

Realistic Tunneling States for the Magnetic Effects in Non-Metallic Real Glasses

Giancarlo Jug^{a,d}[*], Silvia Bonfanti^{a,b} and Walter Kob^c

^aDipartimento di Scienza ed Alta Tecnologia and To.Sca.Lab
Università dell’Insubria, Via Valleggio 11, 22100 Como, Italy

^bLaboratoire Charles Coulomb, Université de Montpellier
Place Eugène Bataillon, F-34095 Montpellier Cedex 5 - France

^cLaboratoire Charles Coulomb, UMR CNRS 5221
Université de Montpellier, 34095 Montpellier, France

^dINFN – Sezione di Pavia, Italy and IPCF – Sezione di Roma, Italy

August 12, 2015

Abstract

The discovery of magnetic and compositional effects in the low temperature properties of multi-component glasses has prompted the need to extend the standard two-level systems (2LSs) tunneling model. A possible extension [1] assumes that a subset of tunneling quasi-particles is moving in a three-welled potential (TWP) associated with the ubiquitous inhomogeneities of the disordered atomic structure of the glass. We show that within an alternative, cellular description of the intermediate-range atomic structure of glasses the tunneling TWP can be fully justified. We then review how the experimentally discovered magnetic effects can be explained within the approach where only localized atomistic tunneling 2LSs and quasi-particles tunneling in TWPs are allowed. We discuss the origin of the magnetic effects in the heat capacity, dielectric constant (real and imaginary parts), polarization echo and SQUID magnetization in several glassy systems. We conclude by commenting on a strategy to reveal the mentioned tunneling states (2LSs and TWPs) by means of atomistic computer simulations and discuss the microscopic nature of the tunneling states in the context of the potential energy landscape of glass-forming systems.

1 Introduction

The physics of glasses, especially at low temperatures, continues to attract considerable interest. At low temperatures glasses are believed to be characterized by low-energy excitations going under the name of tunneling systems, or states (TSs) which are normally described in terms of double-welled potentials (DWPs) and two-level systems (2LSs) with energy asymmetry and tunneling barrier uniformly distributed in the amorphous solid [2, 3]. Little is still known about the nature of the TSs, but the general consensus is still that the intermediate-range atomic structure of glasses is well described by Zachariasen's 1932 continuous random network model [4, 5] (thus, homogeneously disordered like for a liquid) and the 2LSs arise out of two slightly similar, localized atomic configurations. With this characterization the 2LSs have been employed in the 1970s and 80s to explain with some success the anomalies in the properties of glasses at low temperatures. Recently, the field has been witnessing a renaissance since the discovery that there are unexpected magnetic effects in insulating glasses [6, 7, 8, 9] and that the TSs are responsible for the decoherence of phase qubits made of superconducting Josephson-junctions [10, 11, 12, 13, 14]. The 2LSs are thought to be ubiquitous in the junction's tunneling barrier which, though very thin, is considered to be amorphous and described by Zachariasen-Warren's model [4, 5]. On the other hand, the low-temperature glasses have also been studied as a paradigm where to conduct research on the physics of aging so common to many disordered systems out of equilibrium [15, 16]. In this context, the relevant degrees of freedom have also been described in terms of 2LSs, with some success [17].

Yet, deviations from the behaviour predicted by the standard tunneling model (STM) have challenged the validity of the model in the case of multi-component glasses with variable content of the good crystal-forming (GCF) component (e.g. $(\text{SiO}_2)_{1-x}(\text{K}_2\text{O})_{1-x}$ with changing x [18, 19]) and especially in glasses of compositions like $\text{BaO}-\text{Al}_2\text{O}_3-\text{SiO}_2$ in the presence of a weak magnetic field [20]. In such glasses (the mixed alkali-silicates have not yet been investigated in a field, but we predict important magnetic effects there, and x -dependent, too) a puzzling non-monotonous magnetic-field dependence has been revealed in most physical properties [6, 7, 8, 9]. The magnetic effect is normally weak, but orders of magnitude larger than expected from basic thermodynamic considerations. The STM is unable to explain the compositional and magnetic effects, thus a suitable extension of the tunneling model for both situations has been proposed by one of us [1]. This extended tunneling model (ETM) rests upon the existence in the multi-component (or contaminated mono-component) glasses of regions of enhanced regularity (RERs) in the atomic structure of the incompletely-frozen (in fact) amorphous solid. A complete mathematical description and physical justification of the ETM thus calls at the very least for a partial demise of the Zachariasen-Warren's vision of the intermediate structure of glasses.

Research on the mechanism of the glass phase transition is also witnessing intense activity [21], with almost all of the investigations conducted from the high-temperature (liquid or supercooled-liquid) side of the transition. Any attempt at a new look at (and demise of) the Zachariasen-Warren's continuous random network model description of the atomic structure of glasses from the low-temperature side is therefore likely to provide new insight also on the nature of the glass transition itself.

In this paper we provide a new scenario for the atomic structure of glasses, the cellular model, a description within which the phenomenological assumptions for the ETM's mathematical formulation become completely justified. The cellular model provides for a more realistic mathematical formulation in terms of a tetrahedric four-welled tunneling potential, the triangular three-welled version employed being nothing but a poor-man's, but probably very realistic, version affording a much simplified mathematical description. Within the cellular approach to the structure of glasses the most significant local tunneling potentials (also in terms of number density) turn out to be the DWPs, for a single (or very few) atomic particles, and the tetrahedric four-welled potential (TFWP) for a correlated cluster of $N \gg 1$ charged atomic particles. A reasonable and very useful simplification for the TFWP is then the replacement of the N interacting and tunneling atomic particles with a single quasi-particle subject to a triangular tunneling potential (TWP) carrying renormalized parameters (charge, magnetic threaded area, energy asymmetry and tunneling probability) moving about one face of the tetrahedric potential. The renormalization is fully justified by the proximity of four similarly quasi-ordered, close-packed atomic cells (RERs) and the reasonable assumption that most of the charged particles will avoid the interstice's centre. We present therefore the mathematical description of the TWP and its quantum mechanics in the appropriate limits for practical applications. We apply the results for the description of the density of states and the temperature and magnetic-field dependence for the specific heat of the glass, then for the dielectric constant (real and imaginary part) in the linear regime, and for the polarization echo - always in the presence of a magnetic field. Finally we apply the model to the description of the temperature

and magnetic-field dependence for the SQUID-magnetization, showing that the ETM keeps providing a good description for this quantity up to room temperatures. As a check that the tunneling states we use are realistic representations of the remnant degrees of freedom in the disordered solid phase we also outline a strategy for the study of these local tunneling states in the potential energy landscape (PEL) with the help of classical numerical simulation of a large number of particles interacting with a BLJ potential.

The paper is organized as follows. In Section 2 we introduce the cellular model for the structure of glasses, an important refinement of Zachariasen's continuous random-network model, and examine the likely tunneling states that emerge from such cellular picture, concluding that only DWPs and TFWPs should be relevant for the physics of glasses below the glass transition temperature T_g . In Section 3 we review the relevant quantum mechanics of the three-welled, poor man's version of the TFWP, a version that has been used so far to obtain a reasonable single explanation for all the anomalies (and deviations from STM predictions) due to composition changes and to the magnetic field. We also show how to evaluate the magnetic density of states (DOS) $n(E, B)$ and, in Section 4, we examine the magnetic-field dependent heat capacity $C_p(T, B)$ comparing with some published data for the multi-silicates. In Section 5 we do the same for the dielectric constant, real part ϵ' and imaginary part ϵ'' , also showing some comparison with available data at low (kHz) frequency. In Section 6 we examine the application of the ETM to the explanation of some of the data for the polarization echoes in the silicates and in glycerol, also explaining the so-called isotope effect. In Section 7 we examine the question of the paramagnetism of insulating glasses *per se*, that is that due to the tunneling states themselves and which we find to be stronger than the Langevin paramagnetism of the trace paramagnetic impurities contained in the multi-silicates. Section 8 contains a discussion about guiding principles on how one should proceed, within a molecular dynamics simulation of a model glass former (the BLJ system in 3D, for example), in order to characterize the relevant tunneling states from a numerical analysis of the PEL and thus make contact with the original phenomenological modelization at low temperatures. Finally, Section 9 contains a Summary of the results obtained and our Conclusions.

2 The Cellular Model for the Atomic Structure of Glasses and the Three-Welled Tunneling Potential

What is a glass? According to Shelby "A glass can be defined as an amorphous solid completely lacking in long range, periodic atomic structure and exhibiting a region (of temperature) of glass transformation behaviour" [22]. This, however, does not mean that the atomic arrangement of a glass should be the same as that for a liquid, as is implicit in Zachariasen's 1932 proposed continuous network picture [4, 5], which has been widely adopted by scholars (at least in the West, see below). This picture differs from that of a liquid only in that a dynamical arrest has occurred, without specifying its ultimate origin. In a spin-glass the ultimate origin of dynamical arrest is magnetic frustration (with or without disorder), but for ordinary structural glasses it remains mysterious and an important open issue [21, 23, 24, 25]. Prior to Zachariasen's scheme, however, the Soviet scientist A.A. Lebedev had proposed, in 1921, the concept of "crystallites" [26], small undefined crystal-like regions clump against each other in random orientation to contain altogether all atoms in the substance. Later, Randall proposed that these be real micro-crystals and explained the rounded-up X-ray spectra from glasses in this way [27]. However, the density of glasses is some 10% less than that of poly-crystalline aggregates and the thermal properties of glasses also cannot be explained through the Lebedev-Randall picture. Despite these observations, the West-Soviet controversy continues to these days. The Zachariasen-Warren model of glass structure was in fact criticized by Hägg [28] in the West right in the early days of X-ray crystallography and a good review of the status quo of this controversy has been recently provided by Wright [29] who concludes from a re-analysis of X-ray and neutron-scattering data from many covalent-bonded and network glasses that indeed *cybotactic groupings* (better-ordered regions) may well be present and frozen-in in most glasses, especially if multi-component. The formation of *polyclusters*, instead of crystallites, in most glasses is the latest claim by the Soviet school [30, 31], based on observations and thermodynamic reasoning. As nicely set out by Bakai [30], the incipient crystals forming at and below T_m (melting point) are in constant competition with kinetically swifter (for glass-forming liquids) polyclusters (or crystallites) that can win thermodynamically and kinetically over crystals during a rapid enough quench. For e.g. the oxyde glasses (e.g. window glass, of composition $\text{CaO-Na}_2\text{O-SiO}_2$) the dilemma is most simply put in these terms. Pure good glass-former (GGF) SiO_2 melts at around 1900 K and vitrifies at around 1475 K, whilst pure GCFs CaO and Na_2O melt at 2886 K and 1405 K, respectively. Yet, the mixture $\text{CaO-Na}_2\text{O-SiO}_2$ vitrifies at around 750-850 K (depending on % composition) and that is way below the melting point of

very bad glass-formers CaO and Na_2O . Since phase separation is commonplace in such ternary mixtures (the recent X-ray tomography imaging of the related molten system $\text{BaO-Na}_2\text{O-SiO}_2$ is compelling [32]), what is then stopping the pockets and channels formed by CaO and Na_2O within the GGF SiO_2 's network to at least initiate some degree of crystalline ordering? In the mono-composed oxydes it will be up to the impurities to take the place of the GCF phase separation.

On the experimental side, the concept of de-vitrification is gradually taking shape with reports of metallic glasses [33] and also monocomponent high coordination covalent solids like Si forming *paracrystals* in the amorphous solid [34]. Therefore, the stance will be taken in this paper that only the purest mono-component glasses may abide to the Zachariasen-Warren continuously random-network model of a glass, whilst the vast majority of real glasses will be organized otherwise at the intermediate-range atomic structure.

The structure proposed is a cellular-type arrangement of better-ordered regions (regions of enhanced ordering, RERs) that can have complicated, maybe fractal, but compact shapes with a narrow size distribution and interstitial regions between them populated by still fast-moving particles (normally charged, probably dangling bonded ions). We remark that a cellular-type structure was already embodied by the “crystallite” idea of Lebedev, but now no micro-crystals are here claimed to exists (except perhaps in the ceramic-glasses case, to an extent). The RERs are more like Wright’s “cybotactic regions” [29] or Treacy’s “paracrystals” [34] and issue from the dynamical heterogeneities (DHs) picture of the glass-forming supercooled liquid phase above T_g (see e.g. Fig. 1) [21, 35, 36, 37]. The DHs picture recognises the presence of regions of “slower” and “faster” particles, and inspection of the slower-particle regions in the supercooled liquid reveals that these are also better ordered (solid-like) whilst the faster-particle regions are much more liquid-like. DHs are ubiquitous in most supercooled liquids [37] and the claim (yet still somewhat speculative) here is that the slower-particle regions will grow on approaching T_g , but only up to a finite size and will be giving rise to the RERs in the frozen, glassy phase. Simulations in the frozen glassy state of the slower- and faster-particle regions confirm that a DHs picture applies also below T_g [38] and with the slower-regions increasing in size as $T \rightarrow 0$. Earlier simulations (always for model systems) [39] pointed out the difficulty of simulating the DHs picture below T_g and came up with a picture of the slower-regions growing, possibly diverging in size, on approaching T_g . In this paper, however, the stance will be taken that the slower-regions’ average size growths, in real systems, but does not diverge at T_g or at any other characteristic temperature. A full numerical proof of this fact is, however, still lacking. We remark that a cellular structure for the glasses

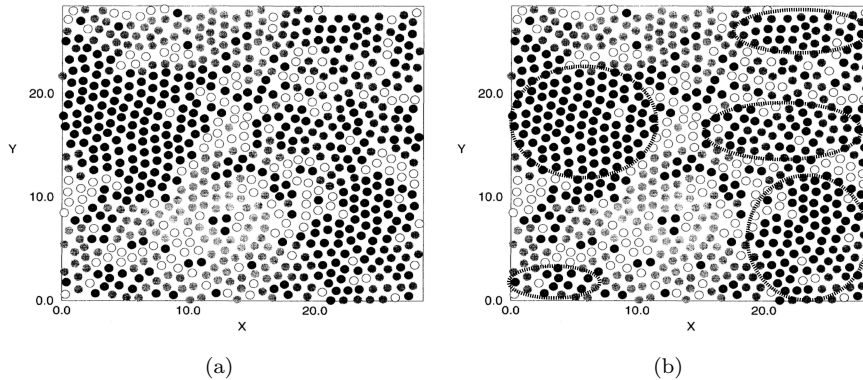


Figure 1: (colour online) (a) Map of the relaxation times of one MD simulation run of a 2D system of 780 soft disks, interacting via a repulsive $1/r^{12}$ potential cut off at some distance (from Ref. [35]). Circles represent particle positions, the slowest 40% coloured black, the fastest 40% shaded gray and the intermediate 20% are unfilled circles. Note the distinct clustering of slow particles (dynamical heterogeneities, DHs). (b) The slower regions have been schematically highlighted to show their incipient cellular structure.

had been proposed in the past by de Gennes [40] and, in the context of the low-temperature anomalies, by Baltes [41] who was able to explain the linear in T anomaly in the heat capacity C_p (but not those in the acoustic properties which require the introduction of 2LSs). A very similar picture is that of the polyclusters of Bakai [30], as already mentioned, but here the thermal history of the cells, or RERs, is ascribed directly to the DHs situation already present above T_g . In this approach the RERs, like grains in the frozen structure below T_g , are the thermal history continuation of the slower particle regions of the DHs above T_g and contain the bulk of the 2LSs. These 2LSs are atomic tunneling states arising from the grains’ own disorder causing a distortion in the natural bond angle between neighbouring cations with the anions becoming susceptible

of taking up two nearly equivalent positions differing by a tiny energy (see Section 8). Some 2LSs may be located at the meeting point between two grains, or cells (two RERs). In the interstitials between grains the faster particles of the DHs at $T > T_g$ give rise for $T < T_g$ to regions where a large number N (on average) of charged atomistic tunneling particles are constrained to move in a coherent fashion due to the high Coulomb repulsion between them. Fig. 2 shows in a schematic way how the atomic/ionic matter can get organised below T_g in a real glass. Since the charged ions (dangling bonds, most likely) should act as a coherently

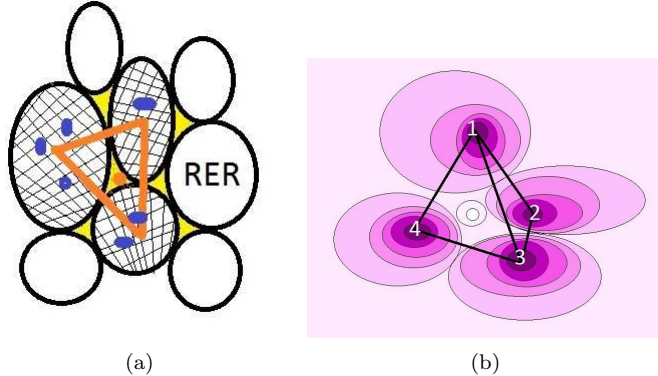


Figure 2: (colour online) (a) 2D cartoon of the cellular structure of an amorphous solid just below T_g . The RERs (black-circled blobs, an oversimplified schematics for fractal-like, but compact objects) have grown to completely fill the space and enclose atomistic tunneling states of the 2LS type (blue blobs). At the same time, in the RER interstitials (yellow regions, connecting to each other) the trapped, charged and faster particles of the DHs existing above T_g and now probably charged dangling bonds, give rise to coherently tunneling large groups of ions to be represented by a single fictitious quasi-particle (orange dot) subjected to an effective tunneling potential having four natural wells in distorted tetrahedral configuration (b) for close-packed RERs. (b) The tetrahedral four-welled potential (TFWP) in a 3D representation with colour-coded potential intensity (dark=deepest, light=highest).

tunneling ensemble, it seems natural to simplify the description of the physics at the lower temperatures using phonons, propagating in the collection of cells now jammed against each other, and remnant localized degrees of freedom acting as TSs. These TSs will be the 2LSs within the cells and at their points of contact (owing to inherent disorder in the cells' atomic arrangement) and effective quasi-particles sitting in the close-packed cells' interstices and representing the collective motion of the coherently- tunneling ions trapped in each interstice (Fig. 2). The quasi-particle will be subjected to an effective potential of distorted- tetrahedral

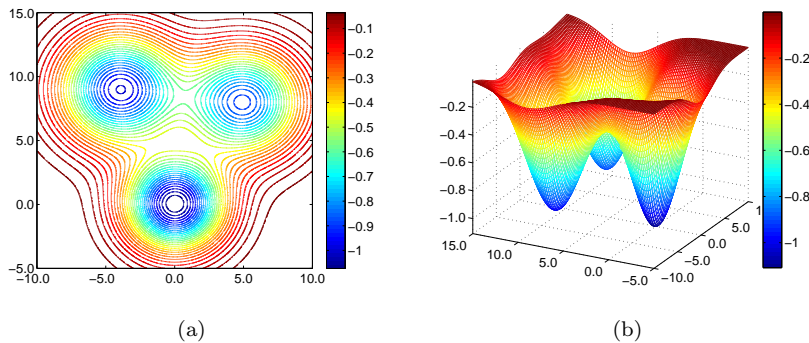


Figure 3: (colour online) (a) Contour plot of a possible realization of the 2D effective three-welled potential (TWP) most likely felt by the quasi-particle of those charged real particles dangling from a group of three RERs on each one face of the tetrahedral configuration of an interstice formed by close-packed RERs well below T_g . (b) 3D visualization of the same example of a TWP potential.

shape characterized by four wells for each interstice, with a high barrier in the interstice's centre. *De facto* this 3D interstitial TFWP potential can be replaced with four local 2D potentials for the four quasi-particles describing the coherent tunneling of the dangling-bond particles sitting near each face of the tetrahedron,

close to a group of three (on average) quasi-ordered cells (Fig. 3). Because of the better ordering implicit in this model of the glassy intermediate-range atomic structure and in each cell, the three wells of each effective local 2D potential for the tunneling quasi-particles (four per interstice, on average) will be near-degenerate in terms of their ground-state energy asymmetries: $E_1 \simeq E_2 \simeq E_3 \simeq 0$. With this qualitative picture in mind, we now turn to the mathematical description of the physics of the remnant, still ergodic degrees of freedom (phonons in the cells' network, 2LSs and ATSSs (anomalous tunneling systems, four in each interstice). For our model of a real glass, by construction the 2LSs will be more numerous than the ATSSs.

3 The Quantum Mechanics of the Three Welled Potential

In this approach [1] the relevant degrees of freedom, beside the phonons, are dilute collections of independent 2LSs, described by the STM, and of fictitious quasi-particles tunneling in TWPs.

The formulation of the STM (the 2LS model) for the low temperature properties of glasses is well known. One assumes a collection of DWPs distributed in the substance and represented each by a 2×2 Hamiltonian of the form, in the potential-well (or real-space) representation:

$$\mathcal{H}_{2LS} = -\frac{1}{2} \begin{pmatrix} \Delta & \Delta_0 \\ \Delta_0 & -\Delta \end{pmatrix}. \quad (1)$$

Here the parameters Δ (the energy asymmetry) and Δ_0 (twice the tunneling parameter) are typically characterized by a probability distribution that views Δ and $\ln(\Delta_0)$ (the latter linked to the DWP energy barrier) broadly (in fact uniformly) distributed throughout the disordered solid [42]:

$$\mathcal{P}_{2LS}(\Delta, \Delta_0) = \frac{\bar{P}}{\Delta_0} \quad (2)$$

where some cutoffs are introduced when needed and where \bar{P} is a material-dependent parameter, like the cutoffs. In fact Eq. (2) embodies the Zachariasen-Warren hypothesis for the intermediate atomic structure of a glass, assuming broadly distributed the energy asymmetry $\Delta = E_2^{(0)} - E_1^{(0)}$, hence the single-well ground state energies $E_1^{(0)}$ and $E_2^{(0)}$ themselves, as well as the potential barrier height V_0 appearing in relations such as:

$$\Delta_0 \simeq \hbar\Omega e^{-\frac{d}{\hbar}\sqrt{2mV_0}} \quad (3)$$

$$\Delta_0 = \frac{\hbar\Omega}{2} \left[3 - \sqrt{\frac{8V_0}{\pi\hbar\Omega}} \right] e^{-2\frac{V_0}{\hbar\Omega}} \quad (4)$$

where the first relation is the generic WKB result for an arbitrarily shaped DWP (where m is the particle's mass, Ω its single-well harmonic frequency (tunneling attempt frequency) and d the tunneling distance) and the second formula refers to a symmetric ($\Delta = 0$) DWP made up by two superimposed parabolic wells. In fact, the distribution (2) in the end refers to the combination of parameters $\Delta_0/\hbar\Omega$. The energies of the two levels $|0\rangle$ and $|1\rangle$ are then $\mathcal{E}_{0,1} = \pm\frac{1}{2}\sqrt{\Delta^2 + \Delta_0^2}$ and so on [2, 42].

The tunneling Hamiltonian of a particle in a TWP is easily written down, in the same low- T spirit as for a 2LS, as a generalization of the above matrix formulation to three levels [1]:

$$\mathcal{H}_{3LS} = \begin{pmatrix} E_1 & D_0 & D_0 \\ D_0 & E_2 & D_0 \\ D_0 & D_0 & E_3 \end{pmatrix} \quad (5)$$

where E_1, E_2, E_3 are the energy asymmetries between the wells and D_0 is the most relevant tunneling amplitude (through saddles of the PEL, in fact). This 3LS Hamiltonian has the advantage of readily allowing for the inclusion of a magnetic field $B > 0$, when coupling orbitally with a tunneling "particle" having charge q (q being some multiple of the electron's charge $-e$) [1]:

$$\mathcal{H}_{3LS}(B) = \begin{pmatrix} E_1 & D_0 e^{i\varphi/3} & D_0 e^{-i\varphi/3} \\ D_0 e^{-i\varphi/3} & E_2 & D_0 e^{i\varphi/3} \\ D_0 e^{i\varphi/3} & D_0 e^{-i\varphi/3} & E_3 \end{pmatrix} \quad (6)$$

where $\varphi/3$ is the Peierls phase for the tunneling particle through a saddle in the field, and φ is the Aharonov-Bohm (A-B) phase for a tunneling loop and is given by the usual formula:

$$\varphi = 2\pi \frac{\Phi}{\Phi_0}, \quad \Phi_0 = \frac{h}{|q|} \quad (7)$$

Φ_0 being the appropriate flux quantum (h is Planck's constant) and $\Phi = \mathbf{B} \cdot \mathbf{S}_\Delta$ the magnetic flux threading the area S_Δ formed by the tunneling paths of the particle in this simple (poor man's, yet as we have seen realistic) model. The energy asymmetries E_1, E_2, E_3 typically enter through their combination $D \equiv \sqrt{E_1^2 + E_2^2 + E_3^2}$. For $n_w=3$ wells an exact solution for the $k=0, 1, 2$ eigenvalues of the multi-welled tunneling Hamiltonian Eq. (6) is still possible:

$$\begin{aligned} \mathcal{E}_k &= 2D_0 \sqrt{1 - \frac{\sum_{i \neq j} E_i E_j}{6D_0^2}} \cos \left(\frac{1}{3}\theta + \theta_k \right) \\ \cos \theta &= \left(\cos \varphi + \frac{E_1 E_2 E_3}{2D_0^3} \right) \left(1 - \frac{\sum_{i \neq j} E_i E_j}{6D_0^2} \right)^{-3/2} \end{aligned} \quad (8)$$

$\theta_k = 0, +\frac{2}{3}\pi, -\frac{2}{3}\pi$ distinguishing the three eigenstates. In the physically relevant limit, which we now discuss, in which $\varphi \rightarrow 0$ (weak fields) and $D = \sqrt{E_1^2 + E_2^2 + E_3^2} \rightarrow 0$ (near-degenerate distribution), and at low temperatures, we can approximate (in a now simplified calculation) the $n_w = 3$ - eigenstate system with an *effective* 2LS having a gap $\Delta\mathcal{E} = \mathcal{E}_1 - \mathcal{E}_0$ widening with increasing φ if $D_0 > 0$ (see below):

$$\lim \Delta\mathcal{E} \simeq \frac{2}{\sqrt{3}} \sqrt{D_0^2 \varphi^2 + \frac{1}{2}(E_1^2 + E_2^2 + E_3^2)} \rightarrow \sqrt{D_0^2 \varphi^2 + D^2} \quad (9)$$

(a trivial rescaling of D_0 and of the E_i was applied). One can easily convince oneself that if such a TWP is used with the standard parameter distribution, Eq. (2) with D, D_0 replacing Δ, Δ_0 , for the description of the TS, one would then obtain essentially the same physics as for the STM's 2LS-description. In other words, there is no need to complicate the minimal 2LS-description in order to study glasses at low temperatures, unless structural inhomogeneities of the RER-type and a magnetic field are present. Without the RERs, hence no distribution of the type (10) below, the interference from separate tunneling paths is only likely to give rise to an exceedingly weak A-B effect. Hence, it will be those TSs nesting between the RERs that will give rise to an enhanced A-B interference and these TSs can be minimally described – most appropriately – through Hamiltonian (6) and with distribution of asymmetries thus modified to favour near-degeneracy (P^* being a dimensionless material parameter) [1]:

$$\mathcal{P}_{3LS}^*(E_1, E_2, E_3; D_0) = \frac{P^*}{D_0(E_1^2 + E_2^2 + E_3^2)}. \quad (10)$$

We remark that the incipient “crystallinity” of the RERs calls for near-degeneracy in E_1, E_2, E_3 simultaneously and not in a single one of them, whence the correlated form of (10). We now have three-level systems (3LSs) with energy levels $\mathcal{E}_0 < \mathcal{E}_1 \ll \mathcal{E}_2$, periodic in φ . The typical spectrum, with $D_0 > 0$ (see below), is shown in Fig. 4 as a function of φ and one can see that the third, highest level \mathcal{E}_2 can be safely neglected for most applications. Other descriptions, with TFWPs or modified three-dimensional DWPs are possible for the TSs nested in the RERs and lead to the same physics as from Eqs. (6) and (10) above [43] (which describe what we call the anomalous tunneling systems, or ATSs, nesting in the interstitials between the RERs). The final and most important consideration for the construction of a suitable mathematical model is that the TSs appear to be rather diluted defects in the glass (indeed their concentration is of the order of magnitude of that for trace paramagnetic impurities, as we shall see), hence the tunneling “particles” are embedded in a medium otherwise characterized only by simple acoustic-phonon degrees of freedom. This embedding, however, means that the rest of the material takes a part in the making of the tunneling potential for the TS's “particle”, which itself is not moving quantum-mechanically in a vacuum. Sussmann [44] has shown that this leads to local trapping potentials that (for the case of triangular and tetrahedral perfect symmetry) must be characterized by a degenerate ground state. This means that, as a consequence of this TS embedding, our poor man's model, Eq. (6), for the ATSs must be chosen with a positive tunneling parameter [1]:

$$D_0 > 0 \quad (11)$$

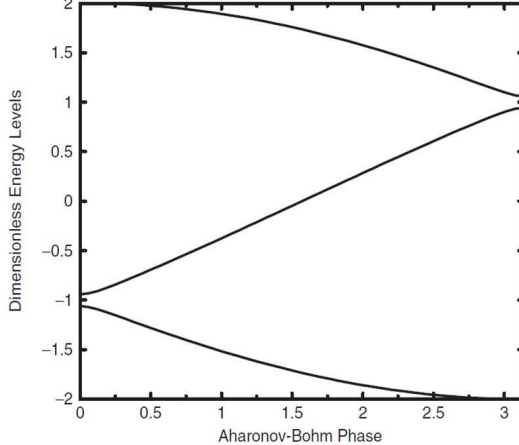


Figure 4: The energy spectrum ($D_0 = 1$ units) of the ATS (3LS, TWP) model, in the appropriate limits of weak field and near-degeneracy due to the embedding within RER's interstitials. On the horizontal axis the A-B phase $\varphi \propto B$.

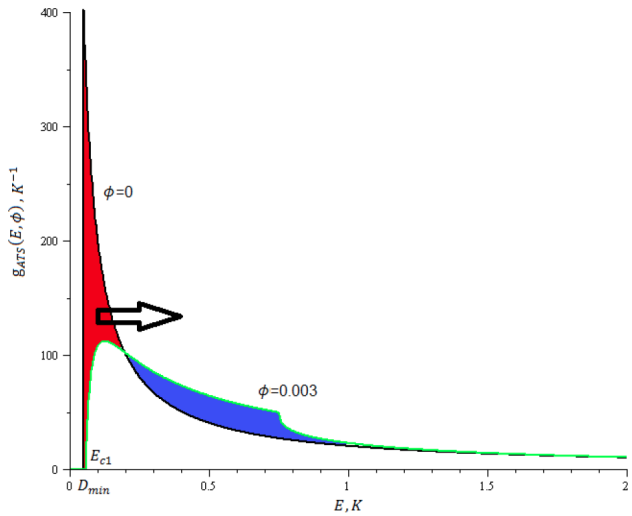


Figure 5: (colour online) The magnetic-sensitive part of the density of states (DOS) as a function of the energy gap E and different A-B phases φ (proportional to the magnetic field B) ($n_{ATS}P^*$ has been set to 1). The rapid shift of quantum states to higher energy when a very weak B is switched on is the physical explanation for the origin of the magnetic effects.

where of course perfect degeneracy is always removed by weak disorder in the asymmetries. The intrinsic near-degeneracy of (10) implies that this model should be used in its $D/D_0 \ll 1$ limit, which in turn reduces the ATSs to effective magnetic-field dependent 2LSs and greatly simplifies the analysis together with the limit $\varphi \rightarrow 0$ which we always take for relatively weak magnetic fields. The ETM, first proposed in [1], consists then in a collection of independent, non-interacting 2LSs described by the STM and also 3LS TWPs, described by Eqs. (6) and (10) above, in the said $D/D_0 \ll 1$ and $\varphi \rightarrow 0$ limits, the 3LSs nested in the interstitials between the close-packed RERs and the magnetic-field insensitive 2LSs distributed in the remaining homogeneously-disordered matrix of RERs and at their touch points or interfaces [46]. In Fig. 5 we illustrate the behaviour of the density of states (DOS) for this model as a function of the gap energy E for different φ values. This figure shows the physical origin of the magnetic effects: the quantum states being conserved in number, they are very rapidly shifted towards high values of the energy when a magnetic field, even very weak, is switched on. Our ETM has been able to explain the magnetic effects in the heat capacity [1], in the real [45] and imaginary [47] parts of the dielectric constant and in the polarization echo amplitude [47] measurements reported to date for various glasses at low temperatures, as well as the composition-dependent anomalies [19, 46]. The new physics is provided by the magnetic-field dependent TS

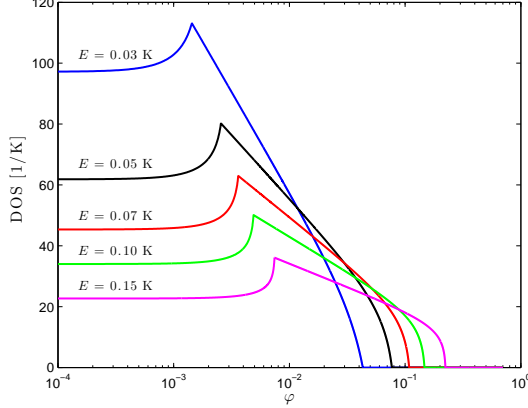


Figure 6: (colour online) The magnetic-sensitive part of the density of states (DOS) as a function of the A-B phase φ (proportional to the magnetic field B) and different energies ($n_{ATS}P^*$ has been set to 1). The shape of this part of the DOS (coming from the TWPs with a parameter distribution (10) favouring near-degeneracy) is the ultimate source of all the magnetic effects. The cusp is an artifact of the effective 2LS approximation [1], but also of the existence of upper and lower bounds for D_0 owing to the nature of the RER glassy atomic structure.

DOS, which acquires a term due to the near-degenerate TWPs [1] that gets added up to the constant DOS from the STM 2LSs (having density n_{2LS}):

$$\begin{aligned} g_{tot}(E, B) &= n_{2LS} \bar{P} + n_{ATS} \frac{P^*}{E} f_{ATS}(E, B) \theta(E - E_{c1}) \\ &= g_{2LS}(E) + g_{ATS}(E, B) \end{aligned} \quad (12)$$

where n_{ATS} is the ATSs' concentration, f_{ATS} is a magnetic-field dependent dimensionless function, already described in previous papers [1], and E_{c1} is a material and B -dependent cutoff:

$$\begin{aligned} g_{ATS}(E, \varphi) &= \int \Pi_i dE_i \delta(\sum_j E_j) \int dD_0 \mathcal{P}_{3LS}^*(\{E_k\}, D_0) \delta(E - \Delta\mathcal{E}) \\ &= \begin{cases} \frac{2\pi P^*}{E} \ln \left(\frac{D_{0max}}{D_{0min}} \sqrt{\frac{E^2 - D_{0min}^2 \varphi^2}{E^2 - D_{0max}^2 \varphi^2}} \right) & \text{if } E > E_{c2} \\ \frac{2\pi P^*}{E} \ln \frac{\sqrt{(E^2 - D_{0min}^2 \varphi^2)(E^2 - D_{0max}^2 \varphi^2)}}{D_{0min} D_{0max} \varphi} & \text{if } E_{c1} \leq E \leq E_{c2} \\ 0 & \text{if } E < E_{c1}. \end{cases} \end{aligned} \quad (13)$$

Here, after a suitable renormalization of parameters: $E_{c1} = \sqrt{D_{min}^2 + D_{0min}^2 \varphi^2}$, $E_{c2} = \sqrt{D_{min}^2 + D_{0max}^2 \varphi^2}$, D_{min} , D_{0min} and D_{0max} being suitable cutoffs (material parameters). The $1/E$ dependence of the ATS DOS is a consequence of the chosen tunneling parameter distribution, Eq. (10), and gives rise to a peak in g_{tot} near E_{c2} that is rapidly eroded away as soon as a weak magnetic field is switched on. The form and evolution of the magnetic part of the DOS is shown in Fig. 6 for some typical parameters, as a function of $\varphi \propto B$ for different values of E . This behaviour of the DOS with B is, essentially, the underlying mechanism for all of the experimentally observed magnetic field effects in the cold glasses within this model: the measured physical properties are convolutions of this DOS (with appropriate B -independent functions) and in turn reproduce its shape as functions of B .

4 The Magnetic Field Dependent Heat Capacity

4.1 Theory

As a first example, the total TS heat capacity is given by

$$C_{pTS}(T, B) = \int_0^\infty dE g_{tot}(E, B) C_{p0}(E, T) \quad (14)$$

where

$$C_{p0}(E, T) = k_B \left(\frac{E}{2k_B T} \right)^2 \cosh^{-2} \left(\frac{E}{2k_B T} \right) \quad (15)$$

is the heat capacity contribution from a single TS having energy gap E and where $g_{tot}(E, B)$ is given by Eq. (12).

In this Section we re-analyze some of the available data [48] for the magnetic effect in the heat capacity of two multi-component glasses, commercial borosilicate Duran and barium-allumo-silicate (AlBaSiO, or BAS in short) glass, in order to show that the ATS model works well for the magnetic-field dependent C_p . A systematic experimental study of $C_p(T, B)$ around and below 1 K in these multi-silicate glasses was carried out by Siebert [48] and those data have been used, upon permission, by one of us [1] as the very first test of the above (Sections 2, 3) ETM [1]. That earlier analysis best-fitted the C_p data by Siebert with the sum of Einstein's $\gamma_{ph}T^3$ phonon term plus the 2LS $\gamma_{2LS}T$ non-magnetic contributions, as well as with Langevin's paramagnetic and the ATS contributions (see below). The analysis came up with concentrations $\bar{n}_J \simeq 48$ ppm and, respectively, $\bar{n}_J \simeq 20$ ppm instead of the quoted [48] 126 ppm (or 180 ppm in a different study [49]) and 102 ppm for Duran and for BAS glass, respectively.

In order to better understand this large discrepancy we re-analysed Siebert's data for $C_p(T, B)$, after subtraction of the data taken at the same temperatures for the same glass, but in the presence of the strongest applied magnetic field (8 T) [50]. In this way only the magnetic-field dependent contributions should remain in the data for $\bar{C}_p(T, B) \equiv C_p(T, B) - C_p(T, \infty)$. The parameters involved when fitting data are the cutoff D_{min} and combinations of cutoffs, charge and area $D_{0min}qS$ and $D_{0max}qS$ [1], as well as: $n_{Fe^{2+}}$ (Fe²⁺ impurity concentration), $n_{Fe^{3+}}$ (Fe³⁺ impurity concentration) and n_{ATS} (ATS concentration (always multiplied by P^*)). The data from [48] (we have restricted the best fit to the three temperatures having the most data points around the peak of $C_p(B)$) have been best-fitted by using the following magnetic-dependent contributions:

a. the known Langevin contribution of the paramagnetic Fe impurities (Fe²⁺ and Fe³⁺) having concentration n_J :

$$C_J(T, B) = n_J \frac{k_B z^2}{4} \left(\left(\frac{1}{\sinh \frac{z}{2}} \right)^2 - \left(\frac{2J+1}{\sinh \frac{(2J+1)z}{2}} \right)^2 \right) \quad (16)$$

where $z = \frac{g\mu_B J B}{k_B T}$ and where g is Landè's factor for the paramagnetic ion in that medium, μ_B is Bohr's magneton and J the ion's total angular momentum (in units $\hbar=1$); k_B is Boltzmann's constant. We have assumed the same values the parameters g and J take for Fe²⁺ and Fe³⁺ in crystalline SiO₂: $J=2$ with $g=2$ and, respectively, $J = 5/2$ with $g=2$ (we have adopted, in other words, complete quenching of the orbital angular momentum [51], consistent with other Authors' analyses [48, 52]).

b. the averaged contribution of the ATSs [1], written in terms of a sum of individual contributions from each ATS of lowest energy gap E (making use of Eqs. (12), (13) and (14)):

$$\begin{aligned} C_{ATS}(T, \varphi) = & \frac{\pi}{4} \frac{P^* n_{ATS}}{k_B T^2} \\ & \times \left\{ \int_{E_{c1}}^{E_{c2}} dE \frac{E}{\cosh^2(\frac{E}{2k_B T})} \ln \left[\frac{(E^2 - D_{0min}^2 \varphi^2)(E^2 - D_{min}^2)}{D_{min}^2 D_{0min}^2 \varphi^2} \right] \right. \\ & \left. + \int_{E_{c2}}^{\infty} dE \frac{E}{\cosh^2(\frac{E}{2k_B T})} \ln \left[\left(\frac{D_{0max}}{D_{0min}} \right)^2 \frac{E^2 - D_{0min}^2 \varphi^2}{E^2 - D_{0max}^2 \varphi^2} \right] \right\} \end{aligned} \quad (17)$$

or, re-written in a dimensionless form as

$$\begin{aligned} C_{ATS}(T, \varphi) = & \tilde{C}_0(T, \varphi) + 2\pi P^* n_{ATS} k_B \left\{ [I(x_{c1}) - I(x_{c2})] \ln(x_{min} x_{0min} \varphi) \right. \\ & \left. + \frac{1}{2} [\mathcal{I}(x_{c1}, x_{min}) - \mathcal{I}(x_{c2}, x_{min}) + \mathcal{I}(x_{c1}, x_{0min} \varphi) - \mathcal{I}(x_{c2}, x_{0max} \varphi)] \right\} \end{aligned} \quad (18)$$

where:

- $E_{c1} = \sqrt{D_{min}^2 + D_{0min}^2 \varphi^2}$ and $E_{c2} = \sqrt{D_{min}^2 + D_{0max}^2 \varphi^2}$;
- $x_{c1,2} = \frac{E_{c1,2}}{2k_B T}$, $x_{min} = \frac{D_{min}}{2k_B T}$, etc.;

BAS glass	Concentration [g ⁻¹]	Concentration [ppm]
$n_{Fe^{2+}}$	1.06×10^{17}	14.23
$n_{Fe^{3+}}$	5.00×10^{16}	6.69
$P^* n_{ATS}$	5.19×10^{16}	-

Table 1: Extracted parameters (from the heat capacity data) for the concentrations of ATSs and Fe-impurities for the BAS glass.

Temperature [K]	D_{min} [K]	$D_{0min} \frac{q}{e} S [\text{\AA}^2]$	$D_{0max} \frac{q}{e} S [\text{\AA}^2]$
0.60	0.49	4.77×10^4	3.09×10^5
0.90	0.53	5.07×10^4	2.90×10^5
1.36	0.55	5.95×10^4	2.61×10^5

Table 2: Extracted tunneling parameters (from the C_p data) for the BAS glass.

- $I(x) \equiv x \tanh x - \ln \cosh x$;
- $\mathcal{I}(x, a) \equiv \int_x^\infty dy \frac{y}{\cosh^2 y} \ln(y^2 - a^2)$.

and the following expression:

$$\tilde{C}_0(T, \varphi) = 2\pi P^* n_{ATS} k_B \ln \left(\frac{D_{0max}}{D_{0min}} \right) \{ \ln(2) - I(x_{c2}) \} \quad (19)$$

The angular average over the ATS orientations is performed by replacing $\varphi \rightarrow \frac{\varphi}{\sqrt{3}}$ (in other words averaging $\cos^2 \theta$, θ being the orientation of \mathbf{S} with respect to \mathbf{B}).

The above formula for C_{ATS} is actually correct only for weak magnetic fields (up to about 1 T). For higher magnetic fields one must make use of an improved form [53] for the ATS lower energy gap. In practice, this consists in making the following replacement for the A-B phase φ

$$\varphi^2 \rightarrow \varphi^2 \left(1 - \frac{1}{27} \varphi^2 \right) \rightarrow \frac{1}{3} \varphi^2 \left\{ 1 - \frac{1}{45} \left(\frac{B}{B^*} \right)^2 \right\} \quad (20)$$

where the second expression holds after orientational averaging and where B^* is the upturn value of the magnetic field for, e.g., the B -dependence of the dielectric constant $\epsilon'(T, B)$ [53].

4.2 Comparison with available data

The concentrations of the ATSs and Fe-impurities extracted from the best fit of the heat capacity as a function of B , for the BAS glass, are reported in Table 1; having fixed the concentrations, it was possible to extract the other parameters for the BAS glass (Table 2). The best fit of the chosen data is reported in Fig. 7(a). The concentrations of the ATSs and Fe-impurities extracted from the best fit of the heat capacity as a function of B , for Duran, are reported in Table 3; having fixed the concentrations, it was possible to extract the other parameters for Duran (Table 4). The fit of the chosen data is reported in Fig. 7(b). The first comment that we make is that these good fits, with a smaller set of fitting parameters, repropose concentrations and tunneling parameters very much in agreement with those previously obtained by one of us [1]. The problem with the concentrations of the Fe-impurities reported in the literature is that they do not allow for a good fit of the $\tilde{C}_p(B) = C_p(B) - C_p(\infty)$ data in the small field region when the Langevin contribution alone is employed (Eq. (16) without Eq. (18)). See for instance Section 5, Fig. 23. The Langevin contribution drops to zero below the peak, whilst Siebert's data definitely point to a non-zero value of $\tilde{C}_p(0) = C_p(0) - C_p(\infty)$ at $B = 0$ for any $T > 0$. This non-zero difference is well accounted for by our ETM and it comes from the ATS contribution to the DOS in Eq. (12). The parameter B^* was left indetermined in these fits, owing to the fact that the measured C_p becomes very small at higher fields.

The results of our C_p analysis definitely indicate that the concentration of paramagnetic impurities in the multi-silicate glasses is much lower than previously thought and extracted from SQUID-magnetometry measurements of the magnetization $M(T, B)$ at moderate to strong field values and as a function of T . Therefore we will turn our attention to a re-analysis of the SQUID-magnetometry data in Section 7.

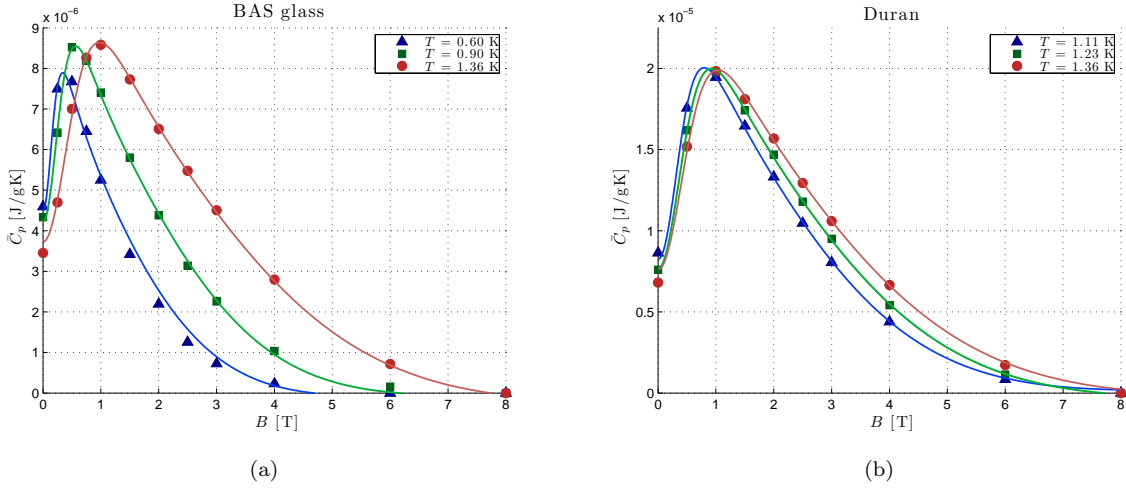


Figure 7: (colour online) The heat capacity best fit for the a) BAS (or AlBaSiO) and b) Duran glasses. The continuous lines are the predictions from the ETM.

Duran	Concentration [g^{-1}]	Concentration [ppm]
$n_{Fe^{2+}}$	3.21×10^{17}	33.01
$n_{Fe^{3+}}$	2.11×10^{17}	21.63
$P^* n_{ATS}$	8.88×10^{16}	-

Table 3: Extracted parameters (from the heat capacity data) for the concentration of ATSs and Fe-impurities for Duran.

Temperature [K]	D_{min} [K]	$D_{0min} \frac{q}{e} S [\text{\AA}^2]$	$D_{0max} \frac{q}{e} S [\text{\AA}^2]$
1.11	0.34	4.99×10^4	2.68×10^5
1.23	0.32	5.30×10^4	2.50×10^5
1.36	0.32	5.54×10^4	2.46×10^5

Table 4: Extracted tunneling parameters (from the C_p data) for Duran.

5 The Magnetic Field Dependent Dielectric Constant

5.1 Dielectric properties of cold glasses: general theory in zero magnetic field

To measure the frequency-dependent dielectric properties of the cold glasses one applies an ac electric field to the sample, typically at radio frequencies (RF). The linear response regime only will be considered in this work. The TSs then couple to this field via the electric charge or dipole moment of the tunneling ‘‘particle’’. The applied electric field both modulates the energy splitting of the tunneling states and excites them from thermodynamic equilibrium. The electric field only affects the asymmetry energy Δ [2]. The influence of the electric field on the tunnel splitting Δ_0 is usually neglected [54]. The coupling of a 2LS to the external field therefore causes resonant processes like resonant absorption and stimulated emission. In the presence of the external electric field \mathbf{F} the Hamiltonian matrix takes the form (coordinate representation):

$$H = H_0 + \mathbf{p}_0 \cdot \mathbf{F} \sigma_z = -\frac{1}{2} \begin{pmatrix} \Delta - 2\mathbf{p}_0 \cdot \mathbf{F} & \Delta_0 \\ \Delta_0 & -\Delta + 2\mathbf{p}_0 \cdot \mathbf{F} \end{pmatrix} \quad (21)$$

Here \mathbf{p}_0 denotes the electric dipole moment of the fictitious particle, $\mathbf{F} = \mathbf{F}_\omega \cos \omega t$ is the time-dependent electric field. Diagonalizing the Hamiltonian (Eq. (21)) one can get (energy representation):

$$H = - \begin{pmatrix} \frac{1}{2}E & 0 \\ 0 & -\frac{1}{2}E \end{pmatrix} + \begin{pmatrix} \frac{\Delta}{E} & \frac{\Delta_0}{E} \\ \frac{\Delta_0}{E} & -\frac{\Delta}{E} \end{pmatrix} \mathbf{p}_0 \cdot \mathbf{F} \cos \omega t \quad (22)$$

The dynamics of the 2LSs is given by the change in the expectation values through the Bloch equations, which were first derived by Bloch in the context of magnetic resonance [55]:

$$\begin{aligned} \frac{dS_x}{dt} &= -\frac{1}{T_2} S_x + \tilde{\gamma} (S_y B_z - S_z B_y) \\ \frac{dS_y}{dt} &= -\frac{1}{T_2} S_y + \tilde{\gamma} (S_z B_x - S_x B_z) \\ \frac{dS_z}{dt} &= -\frac{1}{T_1} (S_z - \langle S_z \rangle) + \tilde{\gamma} (S_x B_y - S_y B_x) \end{aligned} \quad (23)$$

Here we have introduced the pseudo-spin $\frac{1}{2}$ operator $\mathbf{S} = \boldsymbol{\sigma}/2$, where $\boldsymbol{\sigma}$ are Pauli’s matrices (in the 2LS energy representation), T_1 is a characteristic time for the equilibration of the level populations of the 2LS, and T_2 is the transverse dephasing time due to spin-spin (i.e. 2LS-2LS) interactions. Also, $\langle S_z \rangle$ is the thermal equilibrium value of S_z given by $\langle S_z \rangle = \frac{1}{2} \tanh\left(\frac{\tilde{\gamma}hB_z(t)}{2k_B T}\right)$, $\tilde{\gamma}B = \omega_0$, $\tilde{\gamma}$ is the appropriate (fictitious) gyromagnetic ratio and $\mathbf{B} = \mathbf{B}_{dc} + \mathbf{B}_{ac}$ is a fictitious effective field made up of a static (dc) part and of an oscillating (ac) one, both proportional to the electric field with frequency ω . The dimensionless fictitious spin \mathbf{S} processes around this fictitious effective field \mathbf{B} , given by ($\mu = \hbar\tilde{\gamma}$):

$$\mu \mathbf{B} = \left(\frac{2\Delta_0}{E} \mathbf{p}_0 \cdot \mathbf{F}, 0, E + \frac{2\Delta}{E} \mathbf{p}_0 \cdot \mathbf{F} \right) \quad (24)$$

Since the ac field is a small perturbation, one can expand (in linear response theory) $\langle S_z \rangle$ in a Taylor series by keeping terms up to the first order in \mathbf{B}_{ac} . The solution to the Bloch equations takes the form $\mathbf{S}(t) = \mathbf{S}^0(t) + \mathbf{S}^1(t)$, where $\mathbf{S}^0(t)$ is of zeroth order and $\mathbf{S}^1(t)$ is of first order in \mathbf{B}_{ac} . Thus the linearised Bloch equations become, for the zero-order and first-order contributions, respectively, to the \mathbf{S} -components:

$$\begin{aligned} \frac{dS_z^0}{dt} + \frac{1}{T_1} [S_z^0(t) - S_z^0(\infty)] &= 0 \\ \frac{dS_x^1}{dt} - \omega_0 S_y^1 + \frac{1}{T_2} S_x^1 &= 0 \\ \frac{dS_y^1}{dt} + \omega_0 S_x^0 + \frac{1}{T_2} S_y^1 - \delta\alpha S_z^0(t) \cos \omega t &= 0 \\ \frac{dS_z^1}{dt} + \frac{1}{T_1} S_z^1 - \delta\alpha S_z^0(t) \cos \omega t &= 0 \end{aligned} \quad (25)$$

where we introduced the resonance frequency $\omega_0 = \tilde{\gamma}B_{z,dc} = -E/\hbar$, which depends on the level splitting E , $\delta = -\left(\frac{2\Delta}{\hbar E}\right) p_0 F_\omega \cos \theta$ which is a first-order term in the ac field F_ω , θ being the angle between

the ac field and the dipole moment. $S_z^0(0)$ is the initial value of $S_z^0(t)$ shortly after the field is applied, $S_z^0(\infty) = -\tanh(E/2k_B T)/2$ is the equilibrium value of the aligned spin, $\alpha = \Delta_0/\Delta$, and we define $\lambda = \hbar [1 - 4(S_z^0(\infty))^2]/4k_B T$. If one introduces raising and lowering operators $S^\pm = S_x^1 \pm iS_y^1$, then the equations for S^+ and S^- separate. The equations for S^+ becomes:

$$\frac{dS^+(t)}{dt} + i \left(\omega_0 - \frac{i}{T_2} \right) S^+(t) - i\alpha\delta S_z^0(t) \cos \omega t = 0 \quad (26)$$

and the equations for S^- is the complex conjugate of the above. The solutions of these equations are given by the following expressions [56]:

$$\begin{aligned} S_z^0(t) &= S_z^0(\infty) + [S_z^0(0) - S_z^0(\infty)] e^{-t/T_1} \\ S_z^1(t) &= \frac{\delta\lambda}{1 + T_1^2\omega^2} [\cos \omega t + T_1\omega \sin \omega t] \\ S^+(t) &= \frac{\delta\alpha [(\omega_0 - i/T_2) \cos \omega t - i\omega \sin \omega t] S_z^0(\infty)}{(\omega_0 - i/T_2)^2 - \omega^2} \\ &+ \frac{\delta\alpha [(\omega_0 + i/T_1 - i/T_2) \cos \omega t - i\omega \sin \omega t] [S_z^0(0) - S_z^0(\infty)] e^{-t/T_1}}{(\omega_0 + i/T_1 - i/T_2)^2 - \omega^2} \end{aligned} \quad (27)$$

the result for $S^-(t)$ being the complex conjugate of the above equation for $S^+(t)$. The Bloch spins should now be related to the 2LS polarization in the electric field direction. The component p_{\parallel} of the dipole moment along the direction of the electric field, in the diagonal basis as in Eq. (22), is now given by $p_{\parallel} = -\langle \frac{\Delta}{E} \sigma_z + \frac{\Delta_0}{E} \sigma_x \rangle p_0 \cos \theta$ and using the average values of $\langle \sigma_z \rangle$ and $\langle \sigma_x \rangle$ from the solutions of the Bloch equations one can obtain the dipole moment in the energy representation [56]:

$$p_{\parallel} = -p_0 \cos \theta \left(\frac{2\Delta S_z^1(t)}{E} + \frac{\Delta_0(S^+ + S^-)}{E} \right) \quad (28)$$

Then, one must insert the deduced pseudo-spin values $S_z(t)$, $S^+(t)$ and $S^-(t)$, Eqs. (27) to Eq. (28). Eq. (28) depends on the electric field F_{ω} linearly and can be easily differentiated with respect to the electric field, and this gives a formula for the complex dielectric constant $\epsilon = \left. \frac{dp_{\parallel}}{dF_{\omega}} \right|_{F_{\omega}=0}$. For convenience, one may separate the resulting formulae writing $\epsilon = (\epsilon'_{RES} + \epsilon'_{REL}) + i(\epsilon''_{RES} + \epsilon''_{REL})$. These are the real (ϵ') and imaginary (ϵ'') parts of the dielectric constant. The imaginary part is interpreted as a dielectric loss (loss tangent, $\tan \delta = \epsilon''/\epsilon'$) - a parameter of the dielectric material that quantifies its inherent dissipation of electromagnetic energy (much like in a RLC circuit). One gets:

$$\begin{aligned} \epsilon'_{RES} &= \frac{p_0^2 \cos^2 \theta}{\hbar} \left(\frac{\Delta_0}{E} \right)^2 \left[\left(\frac{(\omega_0 + \omega) T_2^2}{1 + (\omega_0 + \omega)^2 T_2^2} + \frac{(\omega_0 - \omega) T_2^2}{1 + (\omega_0 - \omega)^2 T_2^2} \right) \tanh \left(\frac{E}{2k_B T} \right) \right. \\ &\quad \left. - \left(\frac{(\omega_0 + \omega) T_{12}^2}{1 + T_{12}^2 (\omega_0 + \omega)^2} + \frac{(\omega_0 - \omega) T_{12}^2}{1 + T_{12}^2 (\omega_0 - \omega)^2} \right) \left(2S_z^0(0) + \tanh \left(\frac{E}{2k_B T} \right) \right) e^{-t/T_1} \right] \end{aligned} \quad (29)$$

$$\begin{aligned} \epsilon''_{RES} &= \frac{p_0^2 \cos^2 \theta}{\hbar} \left(\frac{\Delta_0}{E} \right)^2 \left[\left(\frac{T_2}{1 + (\omega_0 - \omega)^2 T_2^2} - \frac{T_2}{1 + (\omega_0 + \omega)^2 T_2^2} \right) \tanh \left(\frac{E}{2k_B T} \right) \right. \\ &\quad \left. + \left(\frac{T_{12}}{1 + T_{12}^2 (\omega_0 + \omega)^2} - \frac{T_{12}}{1 + T_{12}^2 (\omega_0 - \omega)^2} \right) \left(2S_z^0(0) + \tanh \left(\frac{E}{2k_B T} \right) \right) e^{-t/T_1} \right] \end{aligned}$$

$$\begin{aligned} \epsilon'_{REL} &= \frac{p_0^2 \cos^2 \theta}{k_B T} \left(\frac{\Delta}{E} \right)^2 \cosh^{-2} \left(\frac{E}{2k_B T} \right) \frac{1}{1 + T_1^2 \omega^2} \\ \epsilon'_{REL} &= \frac{p_0^2 \cos^2 \theta}{k_B T} \left(\frac{\Delta}{E} \right)^2 \cosh^{-2} \left(\frac{E}{2k_B T} \right) \frac{1}{1 + T_1^2 \omega^2} \\ \epsilon''_{REL} &= \frac{p_0^2 \cos^2 \theta}{k_B T} \left(\frac{\Delta}{E} \right)^2 \cosh^{-2} \left(\frac{E}{2k_B T} \right) \frac{T_1 \omega}{1 + T_1^2 \omega^2} \end{aligned} \quad (30)$$

where $T_{12}^{-1} = T_2^{-1} - T_1^{-1}$. In the adiabatic limit the initial value of the pseudo-spin is $S_z^0(0) = -\frac{1}{2} \tanh(E/2k_B T)$, when the 2LS energy eigenvalues are $\pm \frac{1}{2}E$. That makes the time dependent terms of Eq. (29) equal to 0 shortly after applying the field. For an ensemble of 2LS, from the manipulation of the Bloch equations for the motion of the spatial components of a pseudo-spin 1/2 under periodic electric (and/or elastic) perturbations and taking into account the phonon relaxation mechanism, one then finds the explicit form of the expression for the dielectric constant [57]:

$$\epsilon = \epsilon_{RES} + \epsilon_{REL} \frac{1}{1 + i\omega\tau} = \left(\epsilon_{RES} + \epsilon_{REL} \frac{1}{1 + \omega^2\tau^2} \right) - i\epsilon_{REL} \frac{\omega\tau}{1 + \omega^2\tau^2} \quad (31)$$

where we have put $\tau = T_1$. The above equation is the fundamental result of the low-frequency, relaxation-time approach to the complex dielectric constant of glasses. The typical energy splittings of the 2LSs in low temperature experiments correspond to frequencies in the range of $\frac{\omega_0}{2\pi} \approx 10^8$ Hz (GHz range, see Section 6), when the electric field frequency ω is about 10³ Hz. This justifies a low-frequency approximation $\omega \ll \omega_0$. To obtain the resonant part we can also set $T_2^{-1} = 0$, which simplifies expressions (Eq. 29), remembering that $E = \hbar\omega_0$. From the averaging over the dipole orientation angle θ we get a prefactor 1/3: $\overline{p_0^2 \cos^2 \theta} = \frac{1}{3} \overline{p_0^2}$, where $\overline{p_0^2}$ is the configurationally averaged square 2LS electric-dipole moment. The real part of the relative dielectric constant for 2LS shows the temperature-dependent contributions ($\epsilon(T) = \epsilon'(0) + \Delta\epsilon'(T)$, with $|\Delta\epsilon'| \ll \epsilon'$):

$$\frac{\Delta\epsilon'}{\epsilon'} \Big|_{2LS\ RES} = \frac{2}{3} \overline{p_0^2} \frac{\Delta_0^2}{E^3} \tanh\left(\frac{E}{2k_B T}\right) \quad (32)$$

$$\frac{\Delta\epsilon'}{\epsilon'} \Big|_{2LS\ REL} = \frac{1}{3k_B T} \overline{p_0^2} \frac{\Delta^2}{E^2} \cosh^{-2}\left(\frac{E}{2k_B T}\right) \frac{1}{1 + \omega^2\tau^2} \quad (33)$$

Eq. (32) corresponds to the resonant tunneling contribution to the dielectric constant, and Eq. (33) is the relaxational contribution. We neglect for now, for low ω , the frequency dependence in the RES part so long as $\omega \ll \omega_0$. The dielectric loss is described by the following formula (the resonant contribution being vanishingly small):

$$\Delta \tan \delta \Big|_{2LS\ REL} = \frac{\Delta\epsilon''}{\epsilon'} \Big|_{2LS\ REL} = \frac{1}{3k_B T} \overline{p_0^2} \frac{\Delta^2}{E^2} \cosh^{-2}\left(\frac{E}{2k_B T}\right) \frac{1}{1 + \omega^2\tau^2} \quad (34)$$

Integrating Eqs. (32)-(34) over the parameter distribution of the 2LS and over the dipole orientation angle θ , using the expressions for the 2LS (E, τ) -parameter distribution (see e.g. [54]), one can find the temperature-dependent contributions to the dielectric constant and dielectric loss:

$$\begin{aligned} \frac{\Delta\epsilon'}{\epsilon'} \Big|_{2RES} &= \frac{2\overline{P}p_0^2}{3\epsilon_0\epsilon_r} \int_{\Delta_{0,min}}^{E_{max}} \frac{dE}{E} \tanh\left(\frac{E}{2k_B T}\right) \sqrt{1 - \left(\frac{\Delta_{0,min}}{E}\right)^2} \\ \frac{\Delta\epsilon'}{\epsilon'} \Big|_{2REL} &= \frac{\overline{P}p_0^2}{3\epsilon_0\epsilon_r k_B T} \int_{\Delta_{0,min}}^{E_{max}} dE \int_{\tau_{min}(E)}^{\tau_{max}(E)} \frac{d\tau}{\tau} \sqrt{1 - \frac{\tau_{min}(E)}{\tau}} \cosh^{-2}\left(\frac{E}{2k_B T}\right) \frac{1}{1 + \omega^2\tau^2} \\ \Delta \tan \delta \Big|_{2REL} &= \frac{\overline{P}p_0^2}{3\epsilon_0\epsilon_r k_B T} \int_{\Delta_{0,min}}^{E_{max}} dE \int_{\tau_{min}(E)}^{\tau_{max}(E)} \frac{d\tau}{\tau} \sqrt{1 - \frac{\tau_{min}(E)}{\tau}} \cosh^{-2}\left(\frac{E}{2k_B T}\right) \frac{\omega\tau}{1 + \omega^2\tau^2} \end{aligned} \quad (35)$$

If one extends, when appropriate and as a further approximation, the integration limits ($E_{max} \rightarrow \infty$ and $\Delta_{0,min} \rightarrow 0$), then calculating (estimating, in fact) the E -integral one gets a characteristic logarithmic variation of the real part of the dielectric constant as a function of temperature:

$$\frac{\Delta\epsilon'}{\epsilon'} \Big|_{2RES} \approx \begin{cases} -\frac{2\overline{P}p_0^2}{3\epsilon_0\epsilon_r} \ln\left(\frac{T}{T_0}\right), & T < \frac{\Delta_{0,max}}{2k_B} \\ 0, & T > \frac{\Delta_{0,max}}{2k_B} \end{cases} \quad (36)$$

For $\omega\tau_{min} \gg 1$ and at low temperatures, the contribution from relaxation to the real part as compared to the resonant contribution is negligible. Under the condition $\omega\tau_{min} \ll 1$, however, the term $1/\tau$ dominates in the τ -integral and we obtain again a logarithmic variation with temperature:

$$\frac{\Delta\epsilon'}{\epsilon'} \Big|_{2REL} \approx \begin{cases} 0, & \omega\tau_{min} \gg 1 \\ \frac{1}{3\epsilon_0\epsilon_r} \overline{p_0^2} \ln\left(\frac{T}{T_0}\right), & \omega\tau_{min} \ll 1 \end{cases} \quad (37)$$

A crossover between the resonant (low temperature) and relaxation (high T) regimes occurs at a characteristic temperature [57]

$$T_0(\omega) \simeq \frac{1}{k_B} \sqrt[3]{\frac{\omega \pi \rho \hbar^4}{\gamma_l^2/v_l^5 + 2\gamma_t^2/v_t^5}} \quad (38)$$

which for a thermal 2LS with $E = \Delta = k_B T$ satisfies the condition $\omega \tau(T_0) = 1$. The above equation arises from the celebrated expression (see e.g. [54, 57]) for the one-phonon relaxation time:

$$\tau^{-1} = \left(\frac{\gamma_l^2}{v_l^5} + 2 \frac{\gamma_t^2}{v_t^5} \right) \frac{\Delta_0^2 E}{2\pi\rho\hbar^4} \coth\left(\frac{E}{2k_B T}\right), \quad (39)$$

arising from the longitudinal (l) and transverse (t) modes with deformation potentials $\gamma_{l,t}$ and sound speeds $v_{l,t}$, respectively. In terms of (E, τ) the 2LS distribution can be re-written as:

$$\mathcal{P}(E, \tau) = \frac{\bar{P}}{2\tau\sqrt{1 - \tau_{min}(E)/\tau}}, \quad \tau_{min}(E) \leq \tau \leq \tau_{max}(E) \quad (40)$$

where $\tau_{min}(E) = \frac{\gamma}{E^3} \tanh\left(\frac{E}{2k_B T}\right)$ and $\tau_{max}(E) = \frac{\gamma}{\Delta_{0min}^2 E} \left(\frac{E}{2k_B T}\right)$ are the smallest ($\Delta = 0$) and largest ($\Delta_0 = \Delta_{0min}$) relaxation times, respectively. $\gamma = 2\pi\rho\hbar^4 \left(\frac{\gamma_l^2}{v_l^5} + 2\frac{\gamma_t^2}{v_t^5}\right)^{-1}$ is an elastic parameter of the solid and ρ is its density.

Eqs. (36) and (37) show that with increasing temperature the T dependence changes from a decrease in the resonant regime to an increase in the relaxation one. At the temperature $T_0(\omega)$ there is a minimum. Thus, the sum of the two contributions has a characteristic V-shaped form, in a semi-logarithmic plot, with the minimum occurring at a T_0 roughly given by the condition $\omega \tau_{min}(k_B T_0) \cong 1$, or $k_B T_0(\omega) \cong \left(\frac{1}{2}\gamma\omega\right)^{1/3}$. $\epsilon_0\epsilon_r$ is here the bulk of the solid's dielectric constant and we see that a -2:1 characteristic behavior is predicted by the STM with the slope for $T > T_0$ given by Eq. (37). This behavior is indeed observed, but only in very pure (impurity-free) $a\text{-SiO}_2$ [58]. However, in most multi-component glasses (chemically made up of GGFs as well as of GCFs, for example AlBaSiO (or BAS) glass: $a\text{-Al}_2\text{O}_3\text{-BaO-SiO}_2$), or for a contaminated mono-component glass, it is rather a V-shaped curve with a (roughly) -1:1 slope ratio that is often observed. This has been explained by our theory [19].

5.2 Results for the dielectric constant ϵ' in a magnetic field

We now derive the contribution to the dielectric constant $\epsilon(\omega)$ from the TWPs or ATSs sitting in the interstices between the RERs. One can treat the ATS again as an *effective* 2LS having lowest energy gap $\Delta\mathcal{E} = \mathcal{E}_1 - \mathcal{E}_0 = E = \sqrt{D^2 + D_0^2\varphi^2}$ for “weak” fields. Within this picture, the linear-response quasi-static resonant and relaxational contributions to the polarizability tensor $\alpha_{\mu\nu}$ are extracted according to the general 2LS approach described in the previous Section 5.1, to get [45, 59]

$$\alpha_{\mu\nu}^{RES} = \int_0^\infty \frac{dE}{2E} \mathcal{G}_{\mu\nu} \left(\left\{ \frac{E_i}{E} \right\}; \mathbf{p}_i \right) \tanh\left(\frac{E}{2k_B T}\right) \delta(E - \Delta\mathcal{E}) \quad (41)$$

and

$$\alpha_{\mu\nu}^{REL} = \frac{1}{4k_B T} \int_0^\infty dE \left(\sum_{i,j=1}^3 \frac{E_i E_j}{E^2} p_{i\mu} p_{j\nu} \right) \cosh^{-2}\left(\frac{E}{2k_B T}\right) \delta(E - \Delta\mathcal{E}) \quad (42)$$

where

$$\mathcal{G}_{\mu\nu} \left(\left\{ \frac{E_i}{E} \right\}; \mathbf{p}_i \right) = \sum_{i=1}^3 p_{i\mu} p_{i\nu} - \sum_{i,j} \frac{E_i E_j}{E^2} p_{i\mu} p_{j\nu} \quad (43)$$

contains the single-well dipoles $\mathbf{p}_i = q\mathbf{a}_i$. This expression assumes vanishing electric fields and no TS-TS interactions, a situation which does not wholly apply to the experiments. To keep the theory simple one can still use Eq. (41) and the analogous one for the relaxational contribution to the polarizability. Eq. (41) must be averaged over the random energies' distribution (10) ($[\dots]_{av}$, responsible for the high sensitivity to weak

fields) and over the dipoles' orientations and strengths ($\overline{(\dots)}$). For a collection of ATS with $n_w > 2$ wells this averaging presents serious difficulties and one must resort to the decoupling:

$$\overline{\mathcal{G}_{\mu\nu}\delta(E - \Delta\mathcal{E})} \simeq \overline{\mathcal{G}_{\mu\nu}} \cdot \overline{\delta(E - \Delta\mathcal{E})}, \quad (44)$$

where $\overline{[\delta(E - \Delta\mathcal{E})]_{av}} = g_{ATS}(E, B)$ is the fully-averaged density of states. To calculate $\overline{\mathcal{G}_{\mu\nu}}$, one can envisage a fully isotropic distribution of planar n_w -polygons to obtain [59]:

$$\overline{\mathcal{G}_{\mu\nu}} = \frac{1}{3} \left(\frac{n_w}{n_w - 1} \right) \overline{p_i^2} \frac{(n_w - 2)E^2 + D_0^2\varphi^2}{E^2} \delta_{\mu\nu}. \quad (45)$$

The second term in the numerator of Eq. (45) gives rise to a peak in $\delta\epsilon/\epsilon$ at very low B , while the first term (present only if $n_w > 2$) gives rise to a *negative* contribution to $\delta\epsilon/\epsilon$ at larger B which can win over the enhancement term for all values of B if $D_{0max} \gg D_{0min}$ (D_{0min} , D_{0max} corresponding to cutoffs in the distribution of ATS energy barriers). The observations in Duran and BK7 indeed show a significant depression of $\epsilon'(B)$ for weak fields [7], thus giving direct evidence for the existence of ATSs with $n_w > 2$ in the multisilicate glasses. Carrying out the averaging $[\dots]_{av}$ one gets analytical expressions for the polarizability; the uniform average over orientation angles θ must be performed numerically (although a very good approximation is the replacement of φ^2 with $\frac{1}{3}\varphi^2$ in the averaged expression, corresponding to the replacement $\cos^2\theta \rightarrow \frac{1}{3}$).

The expression for the resonant part of the polarizability Eq. (41) should be averaged over the probability distribution of parameters Eq. (10). Averaging over the probability distribution

$\int_{D_{0min}}^{D_{0max}} dD_0 \int dE_1 dE_2 dE_3 \mathcal{P}_{ATS}^*(\{E_i\}; D_0) \delta(\sum_i E_i)$ can be done as in the previous Sections, to get to the expressions

$$\begin{aligned} \alpha_{RES}(T, B) &= \frac{\pi}{2} P^* \overline{p_1^2} \int_0^\infty dE \frac{1}{E^3} \tanh\left(\frac{E}{2k_B T}\right) \int_{D_{0min}}^\infty \frac{dD}{D} \int_{D_{0min}}^{D_{0max}} \frac{dD_0}{D_0} [E^2 - D_0^2\varphi^2] \\ &\quad \times \delta(E - \Delta\mathcal{E}) = \alpha_1(T, B) + \alpha_0(T, B) \\ \alpha_0(T, B) &= \varphi^2 \frac{\pi}{2} P^* \overline{p_1^2} \int_0^\infty \frac{dE}{E^3} \tanh\left(\frac{E}{2k_B T}\right) \int_{D_{0min}}^\infty \frac{dD}{D} \int_{D_{0min}}^{D_{0max}} dD_0 D_0 \delta(E - \Delta\mathcal{E}) \\ \alpha_1(T, B) &= \frac{\pi}{2} P^* \overline{p_1^2} \int_0^\infty \frac{dE}{E} \tanh\left(\frac{E}{2k_B T}\right) \int_{D_{0min}}^\infty \frac{dD}{D} \int_{D_{0min}}^{D_{0max}} \frac{dD_0}{D_0} \delta(E - \Delta\mathcal{E}) \end{aligned} \quad (46)$$

with the energy gap $\Delta\mathcal{E} = \sqrt{D^2 + D_0^2\varphi^2}$.

Similarly to the calculation for the density of states Eq. (13), the integrals in Eq. (46) can be reduced as follows [59]:

$$\begin{aligned} \alpha_0(T, B) &= \varphi^2 \frac{\pi}{2} P^* \overline{p_1^2} \int_{E_{c1}}^{E_{c2}} \frac{dE}{E^2} \tanh\left(\frac{E}{2k_B T}\right) \int_{D_{0min}}^{\frac{1}{\varphi}\sqrt{E^2 - D_{0min}^2}} \frac{D_0 dD_0}{E^2 - D_0^2\varphi^2} \\ &\quad + \frac{\pi}{2} P^* \overline{p_1^2} \int_{E_{c2}}^\infty \frac{dE}{E^2} \tanh\left(\frac{E}{2k_B T}\right) \int_{D_{0min}}^{D_{0max}} \frac{D_0 dD_0}{E^2 - D_0^2\varphi^2} \\ &= \frac{\pi}{2} P^* \overline{p_1^2} \left[\int_{E_{c1}}^{E_{c2}} \frac{dE}{E^2} \tanh\left(\frac{E}{2k_B T}\right) \frac{1}{2} \ln\left(\frac{E^2 - D_{0min}^2\varphi^2}{D_{0min}^2}\right) \right. \\ &\quad \left. + \int_{E_{c2}}^\infty \frac{dE}{E^2} \tanh\left(\frac{E}{2k_B T}\right) \frac{1}{2} \ln\left(\frac{E^2 - D_{0min}^2\varphi^2}{E^2 - D_{0max}^2\varphi^2}\right) \right] \end{aligned} \quad (47)$$

Material and Temperature	$\pi x_{ATS} P^* \bar{p}_1^2 / \epsilon_r \epsilon_0$	$D_{min, K}$	$D_{0min} \left \frac{q}{e} \right S_{\Delta, K^2}$	$D_{0max} \left \frac{q}{e} \right S_{\Delta, K^2}$
BK7 15 mK	$0.089 \cdot 10^{-5}$	0.03	$1.668 \cdot 10^5$	$4.576 \cdot 10^5$
Duran 15 mK	$0.052 \cdot 10^{-5}$	0.021	$2.457 \cdot 10^5$	$4.151 \cdot 10^5$
AlBaSiO 50 mK	$0.89 \cdot 10^{-5}$	0.015	$2.440 \cdot 10^5$	$3.080 \cdot 10^5$
AlBaSiO 94 mK	$3.75 \cdot 10^{-5}$	0.025	$1.225 \cdot 10^5$	$1.589 \cdot 10^5$
AlBaSiO 120 mK	$3.09 \cdot 10^{-5}$	0.0227	$1.767 \cdot 10^5$	$2.248 \cdot 10^5$

Table 5: Fitting parameters for the dielectric constant in a magnetic field for three different types of glasses.

Temperature	$\pi x_{ATS} P^* \bar{p}_1^2 / \epsilon_r \epsilon_0$	$D_{min, K}$	$D_{0min} \left \frac{q}{e} \right S_{\Delta, K^2}$	$D_{0max} \left \frac{q}{e} \right S_{\Delta, K^2}$
50 mK	$4.38 \cdot 10^{-5}$	0.015	$0.076 \cdot 10^3$	$3.047 \cdot 10^4$
70 mK	$12.22 \cdot 10^{-5}$	0.0486	$0.600 \cdot 10^3$	$2.662 \cdot 10^4$
100 mK	$13.63 \cdot 10^{-5}$	0.0486	$3.035 \cdot 10^3$	$7.616 \cdot 10^4$

Table 6: Fitting parameters for the $\text{SiO}_{2+x}\text{C}_y\text{H}_z$ glass for different temperatures.

and likewise for $\alpha_1(T, B)$:

$$\begin{aligned}
\alpha_1(T, B) &= \frac{\pi}{2} P^* \bar{p}_1^2 \int_0^\infty \frac{dE}{E} \tanh \left(\frac{E}{2k_B T} \right) \int_{D_{0min}}^{D_{0max}} \frac{dD_0}{D_0} \frac{E}{\sqrt{E^2 - D_0^2 \varphi^2}} \int_{D_{min}}^\infty \frac{dD}{D} \times \delta(D - D_a) \\
\alpha_1(T, B) &= \frac{\pi}{2} P^* \bar{p}_1^2 \int_{E_{c1}}^{E_{c2}} dE \tanh \left(\frac{E}{2k_B T} \right) \int_{D_{0min}}^{\frac{1}{2} \sqrt{E^2 - D_{min}^2}} \frac{dD_0}{D_0} \frac{1}{E^2 - D_0^2 \varphi^2} + \\
&\quad + \frac{\pi}{2} P^* \bar{p}_1^2 \int_{E_{c2}}^\infty dE \tanh \left(\frac{E}{2k_B T} \right) \int_{D_{0min}}^{D_{0max}} \frac{dD_0}{D_0} \frac{1}{E^2 - D_0^2 \varphi^2} \\
&= \frac{\pi}{2} P^* \bar{p}_1^2 \left[\int_{E_{c1}}^{E_{c2}} \frac{dE}{E^2} \tanh \left(\frac{E}{2k_B T} \right) \frac{1}{2} \ln \left(\frac{(E^2 - D_{0min}^2 \varphi^2)(E^2 - D_{min}^2)}{D_{0min}^2 \varphi^2 D_{min}^2} \right) \right. \\
&\quad \left. + \int_{E_{c2}}^\infty \frac{dE}{E^2} \tanh \left(\frac{E}{2k_B T} \right) \frac{1}{2} \ln \left(\frac{D_{0max}^2 (E^2 - D_{0min}^2 \varphi^2)}{D_{0min}^2 (E^2 - D_{0max}^2 \varphi^2)} \right) \right]
\end{aligned} \tag{48}$$

with E_{c1}, E_{c2} as in Section 4.1. For the whole mass of the glass:

$$\frac{1}{V} \sum_1^{N_{ATS}} (\alpha_1(T, B) + \alpha_0(T, B) - \alpha(T, 0)) = \frac{\mathcal{N}_{ATS}}{V} \Delta \alpha = x_{ATS} \Delta \alpha \tag{49}$$

where x_{ATS} is the volume concentration of ATS and $\alpha(T, 0)$ is:

$$\alpha(T, 0) = \frac{\pi}{2} P^* \bar{p}_1^2 \ln \left(\frac{D_{0max}}{D_{0min}} \right) \int_{E_{c2}}^\infty \frac{dE}{E^2} \tanh \left(\frac{E}{2k_B T} \right) \tag{50}$$

The relative change of the dielectric constant is expressed by Eq. (47), Eq. (48) and Eq. (50):

$$\frac{\Delta \epsilon'(T, B)}{\epsilon'} = x_{ATS} \frac{\Delta \alpha(T, B)}{\epsilon_0 \epsilon_r} = \frac{x_{ATS}}{\epsilon_0 \epsilon_r} (\alpha_1(T, B) + \alpha_0(T, B) - \alpha(T, 0)) \tag{51}$$

Eq. (51) with Eqs. (47)-(48) describes well the experimental data for different glasses, as is shown in Figs. 8-10 and with the fitting parameters presented in Tables 5, 6.

For the sake of clarity, the data and curves in Figs. 9 and 10 have been shifted apart vertically.

5.3 Results for the dielectric loss in a magnetic field

The dielectric loss (or loss angle δ) for a dielectric substance is a measure of the power lost in dissipation and is obtained as the following expression:

$$\tan \delta \equiv \frac{\epsilon''}{\epsilon'} \cong \frac{\epsilon''}{\epsilon_0 \epsilon_r} \tag{52}$$

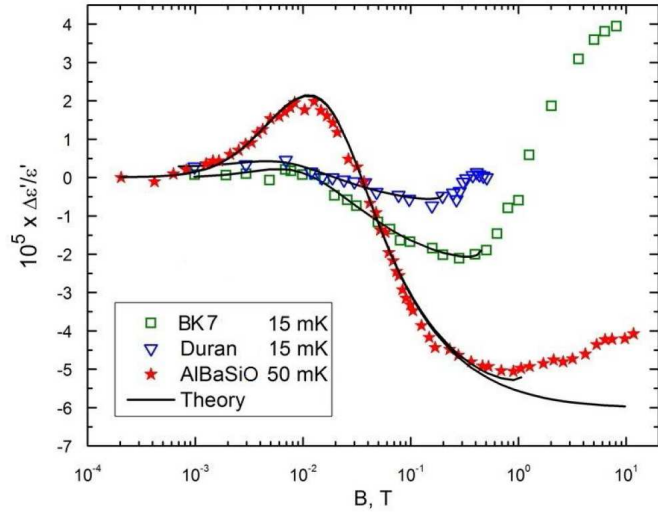


Figure 8: (colour online) The relative dielectric constant variation as a function of the magnetic field for AlBaSiO (BAS) glass [7]b, BK7 [7] and Duran [7]b glasses. With best-fit parameters as in Table 5, the curves are the results of our theory in the “weak field” approximation with (and, for AlBaSiO, without) higher order correction. From [53].

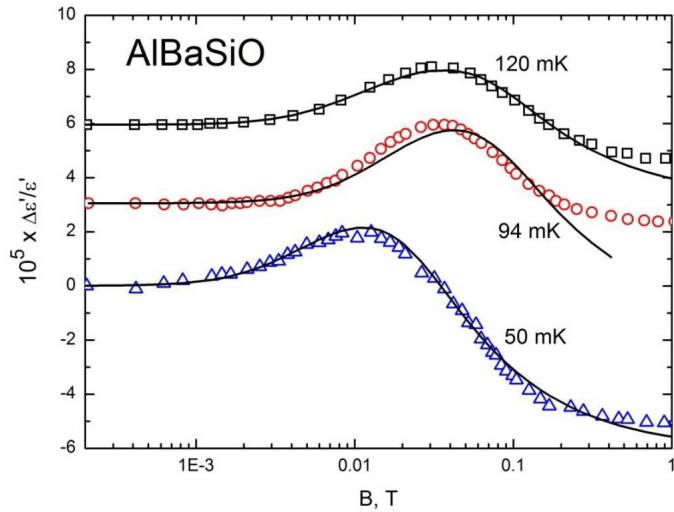


Figure 9: (colour online) Relative dielectric constant variation as a function of the magnetic field and temperature for AlBaSiO (BAS) glass [7]b. With fitting parameters as in Table 5, the curves are the result of our theory in the “weak field” approximation. From [53].

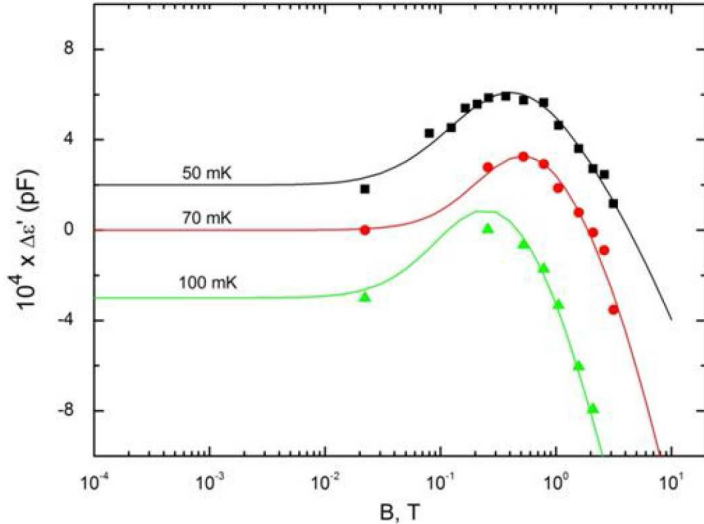


Figure 10: (colour online) Dielectric constant variation as a function of the magnetic field and temperature for the $\text{SiO}_{2+x}\text{C}_y\text{H}_z$ glass [60]. Fitting parameters as in Table 6. From [53].

where $\epsilon'' = \epsilon_{REL} \frac{\omega\tau}{1+\omega^2\tau^2}$ is the imaginary part of the dielectric constant, typically evaluated in the relaxation time approximation (Section 5.1). It should be pointed out that the 2LS STM does not describe well the temperature- and frequency-dependence of ϵ'' in glasses. The reason is that the theory works well only in the low-frequency regime. Since $\epsilon''(\omega)$ should be linked to the real part ϵ' of the dielectric constant through the Kramers-Kroning relation, one can see that the knowledge of the low-frequency behaviour of $\epsilon'(\omega)$ is not enough to reproduce the correct form of $\epsilon''(\omega, T)$. However, inclusion of the ATS contribution does seem to improve the agreement between theory and experiment [53], at least in the case of BK7 (optical glass) which is probably the best approximation to a fully networked glass.

The relaxation part of the dielectric constant depends on the volume concentration $x_{ATS} = n_{ATS}\rho$ of ATS's and is expressed by:

$$\epsilon_{REL} - 1 \cong x_{ATS} \alpha_{REL} \quad (53)$$

where α_{REL} should be averaged over all parameters by means of the distribution function Eq. (10); following similar calculations as in the previous Sections we get:

$$\alpha_{REL} = \frac{\pi P^* p_1^2}{4k_B T} \int_0^\infty \frac{dE}{E^2} \cosh^{-2} \left(\frac{E}{2k_B T} \right) \int_{D_{0min}}^{D_{0max}} \frac{dD_0}{D_0} \int_{D_{min}}^\infty \frac{dD}{D} D^2 \times \frac{\omega\tau_{ATS}}{1 + \omega^2\tau_{ATS}^2} \delta \left(E - \sqrt{D^2 + D_0^2\varphi^2} \right) \quad (54)$$

The relaxation time for ATSs at low temperature and in a magnetic field is now found (after a long calculation that will be reported elsewhere) to be given by the following expression [59]:

$$\tau_{ATS}^{-1} = \tau^{-1}(E, \varphi) = \frac{E^3 (D_0^2\varphi^2 + \frac{5}{6}D^2)}{\Gamma \tanh \left(\frac{E}{2k_B T} \right)} = \frac{E^3 (E^2 - \frac{1}{6}D^2)}{\Gamma \tanh \left(\frac{E}{2k_B T} \right)} = \tau^{-1}(E, D) \quad (55)$$

where as usual the A-B phase φ is directly proportional to the magnetic field B . It appears, therefore, that the total dielectric relaxation time, obtained through its inverse:

$$\frac{1}{\tau_{tot}} = \frac{1}{\tau_{2LS}} + \frac{1}{\tau_{ATS}(\varphi)} \quad (56)$$

must diminish in a non-trivial manner as the magnetic field is switched on. This very interesting prediction of the present theory appears to be confirmed explicitly, albeit only qualitatively, in the laboratory and for some multi-silicate glasses so far only via the work of a Russian group at liquid-He temperatures [61]. A systematic study of the magnetic-field dependence of τ_{tot} in the multi-component glasses is still lacking.

Temperature	$\pi x_{ATS} P^* \bar{p}_1^2 / \epsilon_r \epsilon_0$	D_{min} , K	$D_{0min} \left \frac{q}{e} \right S_\Delta$, K ²	$D_{0max} \left \frac{q}{e} \right S_\Delta$, K ²	$\Gamma = \gamma' k_B^5, (\text{sK}^5)^{-1}$
AlBaSiO					
77 mK	1.5410^{-5}	0.0209	1.9810^4	4.9610^5	5.010^9
88 mK	1.3510^{-5}	0.0206	1.9810^4	4.9610^5	4.010^9
96 mK	1.1010^{-5}	0.0213	1.9810^4	4.9610^5	4.410^9
BK7					
15 mK	2.0210^{-5}	0.0287	0.6910^3	0.6610^4	3.3410^9

Table 7: Fitting parameters for the dielectric loss in a magnetic field in the AlBaSiO (BAS) and BK7 glasses.

The probability distribution function for the ATS dielectric relaxation times turns out to be rather different from that of the standard 2LS case, one finds indeed [59]:

$$P(E, \tau) = \frac{\pi P^* \tau_{min}}{5E(\tau - \tau_{min})(\tau_{max} - \tau)} \quad (57)$$

(with suitable φ -dependent boundaries) where (with Γ a new ATS-related elastic constant). $\tau_{max}(E) = E^5 / [\Gamma \tanh(\frac{E}{2k_B T})]$ is the maximum ATS relaxation time and the minimum allowed is $\tau_{min}(E) = (5/6) \tau_{max}(E)$. The ATS relaxation-time distribution is therefore very narrow-ranged in τ and also very singular (albeit in the $B = 0$ case only). This has important experimental consequences that will be discussed elsewhere. It is however not convenient to switch to τ as an integration variable. Then one writes, integrating over D_0 first via:

$$\delta\left(E - \sqrt{D^2 + D_0^2 \varphi^2}\right) = \frac{E}{\varphi \sqrt{E^2 - D^2}} \delta\left(D_0 - \frac{1}{\varphi} \sqrt{E^2 - D^2}\right) \quad (58)$$

Thus the integral in Eq. (54) becomes:

$$\alpha_{REL} = \frac{\pi P^* \bar{p}_1^2}{4k_B T} \int_0^\infty \frac{dE}{E} \cosh^{-2}\left(\frac{E}{2k_B T}\right) \int_0^\infty dD \frac{D}{E^2 - D^2} \frac{\omega \tau_{ATS}}{1 + \omega^2 \tau_{ATS}^2} \times \theta(D - D_{min}) \theta(D - D_1(E)) \theta(D_2(E) - D) \quad (59)$$

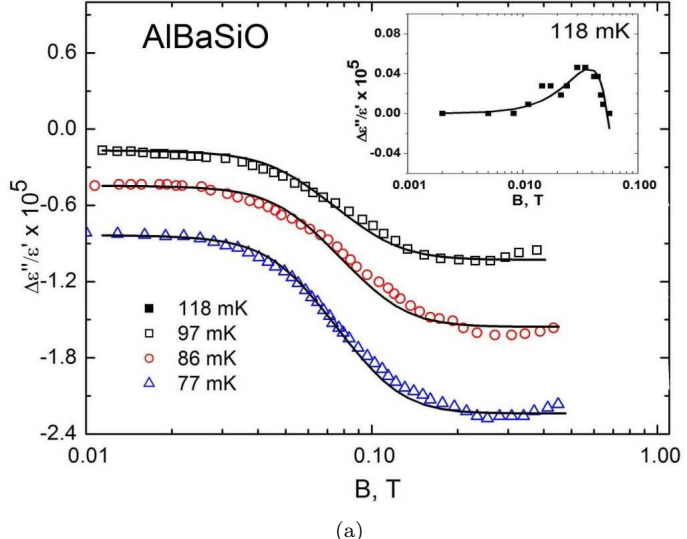
The integral in Eq. (59) has two special points $D_1(E) = \sqrt{E^2 - D_{0max}^2 \varphi^2}$ and $D_2(E) = \sqrt{E^2 - D_{0min}^2 \varphi^2}$, hence $D_1(E) < D_2(E)$. The θ -conditions divide the integral in Eq. (59) into two terms with different intervals in the energy value: $E_{c1} \leq E \leq E_{c2}$ and $E \geq E_{c2}$, and the integral for $E \leq E_{c1}$ vanishes:

$$\alpha_{REL} = \frac{\pi P^* \bar{p}_1^2}{4k_B T} \left[\int_{E_{c1}}^{E_{c2}} \frac{dE}{E} \cosh^{-2}\left(\frac{E}{2k_B T}\right) \int_{D_{min}}^{D_2(E)} dD \frac{D}{E^2 - D^2} \frac{\omega \tau(E, D)}{1 + \omega^2 \tau^2(E, D)} + \int_{E_{c2}}^\infty \frac{dE}{E} \cosh^{-2}\left(\frac{E}{2k_B T}\right) \int_{D_1(E)}^{D_2(E)} dD \frac{D}{E^2 - D^2} \frac{\omega \tau(E, D)}{1 + \omega^2 \tau^2(E, D)} \right] \quad (60)$$

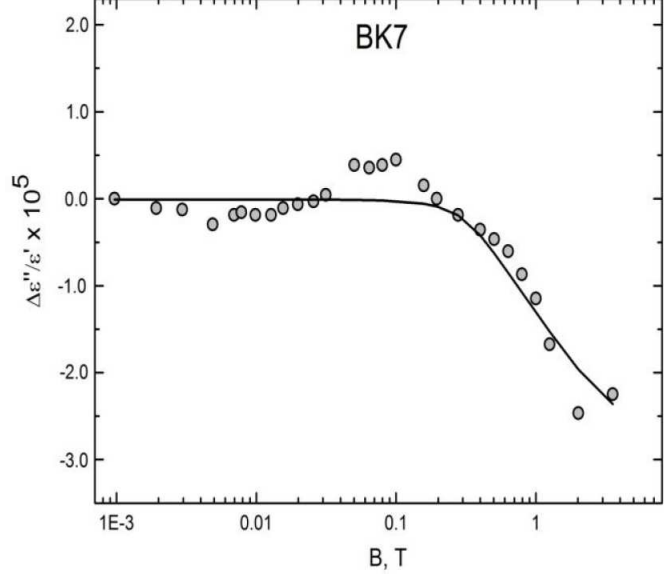
Substituting Eq. (55), Eq. (60) into Eq. (53) and then into Eq. (52) we obtain the final formula for the dielectric loss variation in a magnetic field:

$$\Delta \tan \delta = \frac{x_{ATS} \pi P^* \bar{p}_1^2}{4\epsilon_0 \epsilon_r} \frac{1}{k_B T} \left[\int_{E_{c1}}^{E_{c2}} \frac{dE}{E} \cosh^{-2}\left(\frac{E}{2k_B T}\right) \int_{D_{min}}^{D_2(E)} dD \frac{D}{E^2 - D^2} \frac{\omega \tau(E, D)}{1 + \omega^2 \tau^2(E, D)} + \int_{E_{c2}}^\infty \frac{dE}{E} \cosh^{-2}\left(\frac{E}{2k_B T}\right) \int_{D_1(E)}^{D_2(E)} dD \frac{D}{E^2 - D^2} \frac{\omega \tau(E, D)}{1 + \omega^2 \tau^2(E, D)} \right] \quad (61)$$

with E_{c1} and E_{c2} as in previous Sections. The fitting of relative dielectric loss variation in a magnetic field is shown in Figure 11, using the best-fit parameters from Table 7. One can see that, once again, the experimental data are very well reproduced by the present theory and with fitting parameters very similar to those extracted from the study of the (real part of the) dielectric constant (Section 5.2).



(a)



(b)

Figure 11: (colour online) The relative dielectric loss as a function of the magnetic field and temperature in the AlBaSiO (BAS) (a) and BK7 (b) glasses (data from [7]b). The continuous curves are from the present theory. In the inset of (a) we show that a faint peak seen experimentally at very weak fields can also be explained by the theory. From [53].

6 The Magnetic Field Dependent Polarization Echo Amplitude

6.1 The Polarization Echo Experiment

The experimental detection of electric and phonon echoes in glasses is one strong convincing argument for the 2LSs' existence. Echoes in glasses are similar to other echo phenomena such as spin echo, photon echo and so on. But only at very low temperatures the relaxation of the TSs becomes so slow that coherent phenomena like polarization echoes become observable in the insulating glasses.

The essence of the effect is the following (see Fig. 12). A glass sample placed in a reentrant resonating cavity (“Topfkreisresonator”) is subjected to two short ac electromagnetic pulses at the frequency of about 1 GHz separated by a time interval τ_{12} . The duration τ_1 and τ_2 of these pulses should be much shorter than all relaxation processes in the observed system. The macroscopic polarization produced by the first pulse vanishes rapidly due to the distribution of parameters of the TSs in glasses. This phenomenon is similar to the well-known free-induction decay observed in nuclear magnetic resonance (NMR) experiments. The “phase” (energy-level populations) of each TS develops freely between the two exciting pulses. The second pulse causes an effective time reversal for the development of the phase of the TSs. The initial macroscopic polarization of the glass is recovered roughly at a time τ_{12} after the second pulse. Since the thermal relaxation processes and (see later) spectral diffusion are strongly temperature dependent, polarization echoes in glasses can be observed in practice only at very low temperatures, typically below 100 mK. The echo amplitude is proportional to the number of TSs that are in or near resonance with the exciting microwave pulse and that do not lose their phase coherence during the time $2\tau_{12}$ [42]. It should be pointed out that, due to the wide

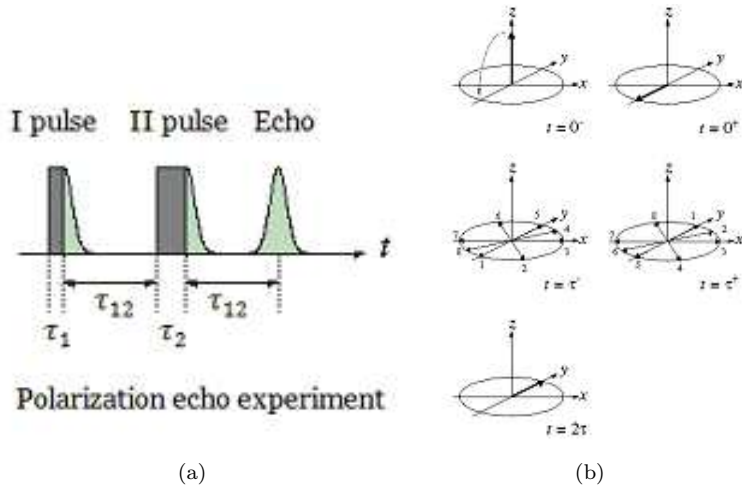


Figure 12: (colour online) The two-pulse polarization echo experiment. Hahn's vector interpretation on the right hand side is for NMR's spin-echo experiment.

distribution for the parameters of the two-level systems in glasses, the description of polarization echoes in glasses is much more complicated than in the case of nuclear spin systems. In analogy to the two-pulse echo in magnetic resonance experiments this phenomenon is referred to as the spontaneous echo.

The polarization echo phenomenon can help to understand more about the microscopic structure of TSs in glasses and gives different kinds of information. The analysis of these experiments follows that for the equivalent magnetic case, except that the TS problem is complicated by three factors. First, the elastic or electric dipoles are not aligned with respect to the driving field and a calculation of the echo signal involves an average over their orientations. Secondly, for a given pumping frequency ω there exists a distribution of induced moments (electric or elastic) and relaxation times, which should be included in the analysis. Finally, in electric echo experiments the local field seen by the TSs is not equal to the applied field, and a local-field correction factor must be used when evaluating absolute values of the dipole moment [42].

In the polarization echo experiments at radio frequencies and at very low temperature of about 10 to 100 mK it has been shown that the TSs in glasses couple directly to the magnetic field [52, 62]. Unexpectedly, the amplitude of two-pulse echoes in the BAS glass was found to be strongly dependent on the applied magnetic field showing a non-monotonic (even oscillatory) field variation. In subsequent papers [8, 63], such behavior

was attributed to the existence of nuclear electric quadrupole moments (NEQM) for some tunneling particles (having nuclear spin $I > \frac{1}{2}$) interacting with the magnetic field and with gradients of the internal microscopic electric field. The NEQM model is based on the consideration that the levels of tunneling particles with non-zero nuclear quadrupole moment exhibit a quadrupole splitting, which is different in the ground state and in the excited state of a tunneling 2LS. The magnetic field causes an additional Zeeman splitting of these levels giving rise to interference effects. In turn, these effects cause the non-monotonic magnetic field variation of the echo amplitude.

The amplitude (or integrated amplitude) of two-pulse polarization echoes of four types of silicate glasses is shown in Fig. 13(a) as a function of magnetic field [62]. In contrast to many other low-temperature properties of glasses the influence of the magnetic field on the amplitude of spontaneous echoes is obviously not universal. BK7 and Duran show similar effects, although the concentration of magnetic impurities differs by at least a factor of 20. Perhaps a most remarkable result of the measurements is the fact that Suprasil I (very pure $a\text{-SiO}_2$) shows no measurable magnetic field effect. While Duran, BAS and BK7 contain nuclei with non-zero nuclear quadrupole moment, Suprasil I is virtually free of such nuclei. This fact is used to provide justification for the nuclear quadrupole model. The variation of the echo amplitude with the applied magnetic field is similar for Duran, BK7 and BAS, but not identical. All three samples exhibit a principal maximum at very weak fields, $B \sim 10$ mT, but only BK7 has a relevant second maximum and a hint to an oscillation in B . At high fields the amplitude of the echo rises well above its value at zero magnetic field and seemingly saturates (yet, see Fig. 7, this is very similar to what happens to the inverted heat capacity, $-C_p$, as a function of B). In Figure 13(b) the amplitude of spontaneous echoes in the BK7 glass is shown as a function of the applied

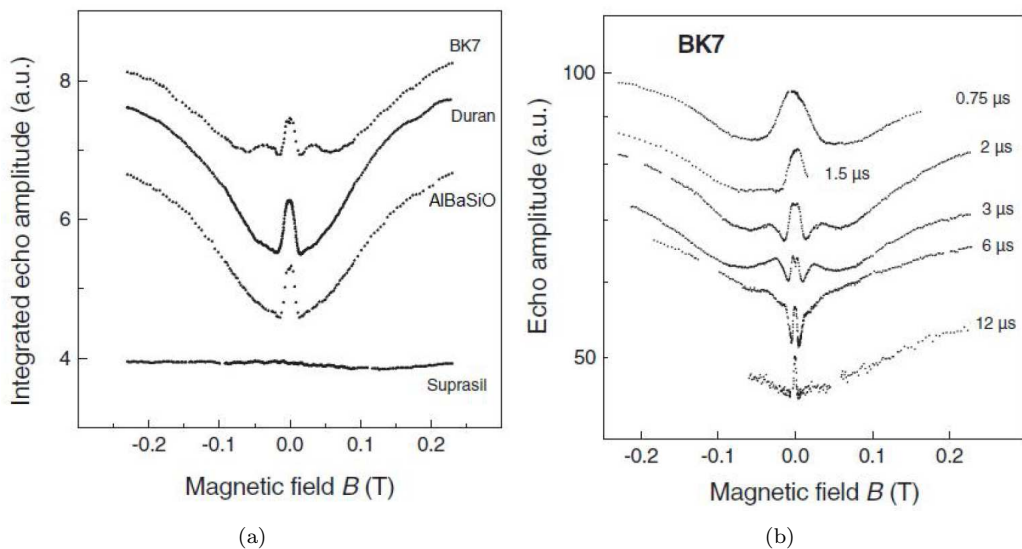


Figure 13: a) The integrated echo amplitude as a function of the magnetic field for different silicate glasses: BK7, Duran, AlBaSiO (BAS) and Suprasil I. All data were taken at $T=12$ mK, $\tau_{12}=2$ ms, and roughly 1 GHz, except for Duran, where the delay time was $\tau_{12}=1.7$ ms [62]. b) The amplitude of two-pulse echoes in BK7 glass as a function of the magnetic field for different values of the waiting time τ_{12} between pulses. All data sets were taken at 4.6 GHz and 12 mK except that for $\tau_{12}=2$ ms which was taken at 0.9 GHz.

magnetic field for different delay times τ_{12} between the exciting pulses. We can see obvious differences for different values of τ_{12} and that a second maximum (the “oscillation”) is not always present. These findings necessitate a good theory for spectral diffusion in real glasses and this theory remains to be accomplished. The most remarkable fact about these experiments on echoes from glasses in a weak magnetic field is that the strong magnetic effect is not confined to the inorganic, silicate glasses. Figure 14 shows the amplitude of spontaneous echoes in partially deuterated and in ordinary amorphous glycerol as a function of the weak magnetic field B . In the case of ordinary glycerol (d_0) there is very small change of the echo amplitude with B . However, for partially deuterated glycerol (d_3) a change is much more noticeable, of a different shape and duration. This experiment seemingly provides proof that the magnetic effect is of nuclear origin, for the two amorphous glycerol samples differ in the content of nuclei carrying a NEQM. Glycerol- d_0 has none, other than the natural abundance of deuterium, some 125 ppm, and of ^{17}O , about 500 ppm, concentrations which

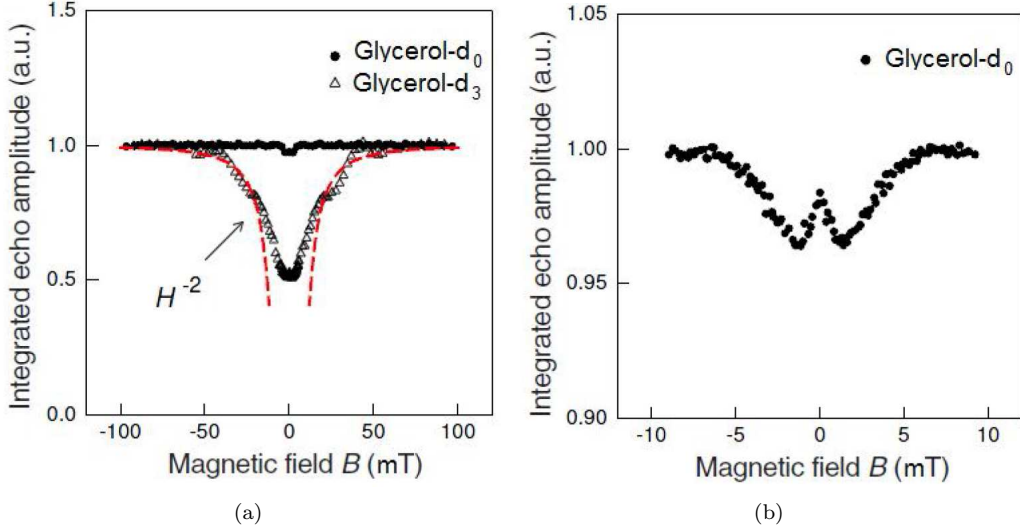


Figure 14: (colour online) The integrated echo amplitude as a function of the magnetic field at $T=13$ mK, generated in partially deuterated glycerol (glycerol-d₃) and in ordinary glycerol (glycerol-d₀). On the left-hand side the figure shows that the echo amplitude for deuterated glycerol-d₃ is much more sensitive to the magnetic field in comparison with non-deuterated glycerol-d₀, shown at the right-hand side (from [9]).

are however a factor 10 too weak to account for the observed magnetic effect. Glycerol-d₃ contains instead 37.5% D ($I=1$) and 62.5% H ($I=1/2$). However, glycerol-d₈ (nominally 100% D) displays a magnetic effect that is only 10% larger than in glycerol-d₃ while glycerol-d₅ (62.5% D) displays a smaller magnetic effect than glycerol-d₃ [8, 69]. All this hints to the fact that the effect does not scale with NEQM concentration. As reproduced in Fig. 15, the integrated echo amplitude as a function of the waiting time τ_{12} in amorphous partially deuterated glycerol-d₅ (that is C₃O₃H₈D₅ instead of ordinary C₃O₃H₈) shows exponential decay with spectacular oscillations at zero applied magnetic field. On the other hand, all oscillations disappear for the relatively weak magnetic field of 150 mT [8, 64, 65]. These findings are extraordinary, especially when combined with the observation that for all multi-silicate glasses the oscillations of the echo amplitude in τ_{12} are absent for all values of the magnetic field (a fact that the NEQM approach cannot explain). All these

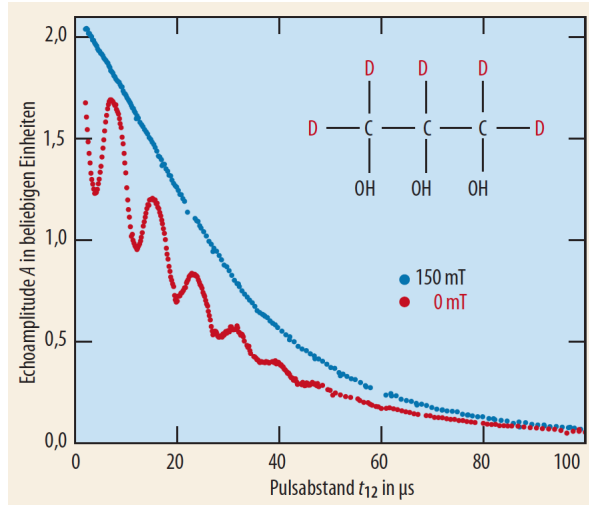


Figure 15: (colour online) The integrated echo amplitude as a function of the waiting time τ_{12} at zero magnetic field (red curve) and in weak magnetic field of 150 mT as generated in deuterated glycerol-d₅ (from [64, 65]).

findings are collectively hard to explain on the basis of the 2LS STM or starting from more microscopic

models and so far only the NEQM has been able to provide the beginning of a rationale for some of these startling experimental results.

6.2 The polarization echo in a magnetic field: Schrödinger equation formalism

Using the density matrix formalism of quantum mechanics, it is possible to obtain, for a collection of 2LSs only, the following expression for the average dipole moment near $t = 2\tau_{12}$: [53]

$$P_{\parallel} = \int dE \int d\Delta_0 \int d\Delta \frac{\bar{P} \Delta_0^3 F_0^3 p_0^4}{\hbar^3 E} \int_0^1 dy y^4 \text{Im} \left[\frac{e^{i\omega t}}{E \Omega_G^3} \tanh \left(\frac{E}{2k_B T} \right) \sin^2 \frac{\Omega_G \tau_2}{2} \right] \quad (62)$$

$$\times \left(\sin \Omega_G \tau_1 - 2i \frac{z}{\Omega_G} \sin^2 \frac{\Omega_G \tau_1}{2} \right) \exp \left(-\frac{\bar{\gamma}}{2} t \right) \exp (iz(t - 2\tau_{12})) \quad (63)$$

$$\times \exp \left(-i \int_0^t \Delta\omega(t') s(t') dt' \right) \delta(E - \sqrt{\Delta^2 + \Delta_0^2}) \quad (64)$$

where: $\mathbf{F} = \mathbf{F}_0(t) \cos(\omega t)$ is the pulsed external electric field (having intensity F_0 and MW frequency ω), \mathbf{p}_0 is the local bare electric 2LS dipole moment, $y = \cos \theta$, θ is the dipole's orientation angle wrt \mathbf{F}_0 , $\Omega_R = \Delta_0 \mathbf{p}_0 \cdot \mathbf{F}_0 / \hbar E$ is the Rabi frequency of the resonant 2LS, $\Omega_G = \sqrt{\Omega_R^2 + (\omega - E/\hbar)^2}$ is the generalized (non-resonant) Rabi frequency, $z = E/\hbar - \omega$ and where $\bar{\gamma} = 2\tau^{-1}$ is the 2LS intrinsic phonon damping (τ being the 2LS phonon-induced relaxation time (Section 5.1)). We have also defined a fluctuating 2LS energy gap $E(t) = E + \hbar\Delta\omega(t)$ with $\hbar\Delta\omega(t)$ the contribution due to interactions with the surrounding thermal 2LSs, and a service function:

$$s(t) = \begin{cases} +1 & \text{if } 0 < t < \tau_{12} \\ -1 & \text{if } t > \tau_{12} \end{cases} \quad (65)$$

This result reproduces (and improves) the derivation by Gurevich et al. [66]. It should be stressed that the (normalized in $\omega_0 = E/h$) spectral function $\sigma(\omega_0) = \frac{1}{2}\Omega_R^2/\Omega_G^3$ is in practice, for $\Omega_R \ll \omega$, very narrowly centered at the pumping frequency ω and can therefore be replaced by a Dirac's $\delta(\omega_0 - \omega)$, thus resulting in the strictly-resonant approximation which is normally employed. Things change considerably, however, when the density of states $g(E)$ is non-uniform, as is the case for the ATS model.

The above result for the echo signal from a collection of 2LS can also be obtained - and from first principles - from a lengthy but straightforward Schrödinger equation treatment in which high-frequency modes are neglected and phonon-damping is treated in a phenomenological way. In the most rigorous way, one obtains for the echo signal:

$$\wp_{\parallel}(t) = \wp_+(t) \cos(\omega\Delta\tau) - \wp_-(t) \sin(\omega\Delta\tau) \quad (66)$$

where $\Delta\tau = \tau_2 - \tau_1$ (whence $\omega\Delta\tau$ typically as large as 10^2) and where:

$$\begin{aligned} \wp_+(t) = & p_{0\parallel} \frac{\Delta_0}{E} \tanh \left(\frac{E}{2k_B T} \right) e^{-\frac{\bar{\gamma}t}{2}} \left(\frac{\Omega_R}{\Omega_G} \right)^3 \\ & \text{Im} \left\{ \sin^2 \left(\frac{\Omega_G \tau_2}{2} \right) \left[\sin(\Omega_G \tau_1) - 2i \frac{\omega_0 - \omega}{\Omega_R} \sin^2 \left(\frac{\Omega_G \tau_1}{2} \right) \right] \right. \\ & \left. \exp \left\{ i\omega_0 (t - 2\bar{\tau}_{12}) - i \int_0^t \Delta\omega(t') s(t') dt' \right\} \right\} \\ \wp_-(t) = & p_{0\parallel} \frac{\Delta_0}{E} \tanh \left(\frac{E}{2k_B T} \right) e^{-\frac{\bar{\gamma}t}{2}} \left(\frac{\Omega_R}{\Omega_G} \right)^3 \\ & \text{Re} \left\{ \sin^2 \left(\frac{\Omega_G \tau_2}{2} \right) \left[\sin(\Omega_G \tau_1) - 2i \frac{\omega_0 - \omega}{\Omega_R} \sin^2 \left(\frac{\Omega_G \tau_1}{2} \right) \right] \right. \\ & \left. \exp \left\{ i\omega_0 (t - 2\bar{\tau}_{12}) - i \int_0^t \Delta\omega(t') s(t') dt' \right\} \right\} \end{aligned} \quad (67)$$

in which $2\bar{\tau}_{12} = \tau_1 + \tau_{12} + \tau_2 + \tau_{12} \approx 2\tau_{12}$ is the total elapsed time at the echo signal's centre. The above Eq. (66) gives the expectation value of the polarization per TS in the direction of the applied electric field. It still needs to be averaged wrt all STM parameter distribution and over a uniform orientational distribution

of 2LS dipoles \mathbf{p}_0 . $\frac{\bar{\gamma}}{2} = \tau^{-1}$ is again the phonon relaxation rate. If $\omega\Delta\tau$ is neglected, then Eq. (64) (after averaging) is recovered for $P_{\parallel} = \bar{\rho}_{\parallel}$.

We are now in the position to extend the polarization echo's calculation to the case of the ATS model describing glasses in a magnetic field; the point of view will be taken that a background of ordinary 2LS's - insensitive to the magnetic field - also exists in the glass. This is in line with our generic cellular model for the real glasses (Section 2).

One starts with a collection of 3LS ($n_w = 3$ is not only computationally convenient, but physically correct as explained in Section 2), but with the single ATS Hamiltonian written in the energy representation:

$$H' = SHS^{-1} = \begin{pmatrix} \mathcal{E}_0 & 0 & 0 \\ 0 & \mathcal{E}_1 & 0 \\ 0 & 0 & \mathcal{E}_2 \end{pmatrix} + S \begin{pmatrix} -\mathbf{p}_1 \cdot \mathbf{F} & 0 & 0 \\ 0 & -\mathbf{p}_2 \cdot \mathbf{F} & 0 \\ 0 & 0 & -\mathbf{p}_3 \cdot \mathbf{F} \end{pmatrix} S^{-1} \quad (68)$$

where the diagonalizing matrix $S = S(\varphi)$ is magnetic-field dependent, the \mathcal{E}_i are the (B -dependent) ATS energy levels and the \mathbf{p}_i are the wells' electric dipoles. As in the treatment of Gurevich *et al.* [66] there is also a phonon bath, but this will be treated - as always - phenomenologically and resulting in a phonon-damping exponential. The second term in Eq. (68) causes irrelevant energy-level shifts and produces an extra matrix term $\Delta H'(t) = (A_{ij})$ of which the only relevant element (see below) is

$$A_{01} = A_{10}^* = \sum_{k=1}^3 -\mathbf{p}_k \cdot \mathbf{F}_0 S_{0k}(\varphi) S_{1k}^*(\varphi) \cos \omega t \quad (69)$$

The A_{ij} cause transitions between the ATS levels 0, 1, 2 when the pulses are applied. In the weak magnetic field limit (most appropriate for the echo experiments) and in the approximation $D \ll D_0$ that we always use (and that is always confirmed by our best fits to the data), one quickly discovers that the second excited level remains unperturbed and one can make use of the "effective 2LS approximation" (where, however, the ground-state wavefunctions of the three wells mix). One can then repeat the Schrödinger equation (or density-matrix, for that matter) calculation carried out for the 2LS case, at the cost of introducing a complex Rabi frequency:

$$\Omega_0 = \frac{A_{01}}{\hbar} \quad (70)$$

The evolution of the generic ATS during and in the absence of pulses can then be followed exactly, in much the same way as before, except that in order to simplify the formalism it is convenient to introduce from the outset an orientationally-averaged Rabi frequency (now a real quantity):

$$\Omega_R = \sqrt{\overline{|\Omega_0|^2}} \quad (71)$$

the bar denoting the average wrt 3LS base-triangle's orientations. Replacing Ω_0 with Ω_R before carrying out the averaging of the sample's polarization is our main approximation, allowing for a considerably simplified treatment and leading to the magnetic-field dependent expression [59]:

$$\Omega_R = \frac{\mathbf{p}_1 \mathbf{F}_0}{\hbar} \sqrt{\frac{D_0^2 \varphi^2 + \frac{5}{6} D^2}{6E^2}} \quad (72)$$

Here, \mathbf{p}_1 is a single-well (averaged) electric dipole and $E = \hbar\omega_0 = \sqrt{D^2 + D_0^2 \varphi^2}$ is the usual magnetic-field dependent lower energy gap in the weak field approximation. The above approximation for Ω_0 treats incorrectly the ATS's that have \mathbf{F}_0 roughly orthogonal to the ATS base triangle; luckily these have $\Omega_0 \approx 0$ and do not contribute to the echo signal.

Proceeding as for the derivation of Eq. (66) one finds that there is a magnetic contribution to the (partly averaged) polarization of the sample from the generic ATS given by [59]:

$$\begin{aligned} \Delta\phi_{\parallel}(t) \cong & -\frac{\hbar}{\mathbf{F}_0} \tanh\left(\frac{E}{2k_B T}\right) e^{-\frac{\bar{\gamma}}{2}t} \frac{\Omega_R^4}{\Omega_G^3} \\ & \text{Im} \left\{ \sin^2\left(\frac{\Omega_G \tau_2}{2}\right) \left[\sin(\Omega_G \tau_1) - 2i \frac{\omega_0 - \omega}{\Omega_R} \sin^2\left(\frac{\Omega_G \tau_1}{2}\right) \right] \right\} e^{i\Phi(t) - i \int_0^t \Delta\omega(t') s(t') dt'} \end{aligned} \quad (73)$$

Now, $\frac{\bar{\gamma}}{2} = \tau^{-1}$ is the magnetic ATS phonon relaxation rate given by Eq. (54), the generalized Rabi frequency is again given by $\Omega_G = \sqrt{\Omega_R^2 + (\omega_0 - \omega)^2}$ and:

$$\Phi(t) = \omega_0(t - 2\bar{\tau}_{12}) + \omega\Delta\tau \quad (74)$$

is the appropriate time argument. From this, it is obvious that the time at which all ATS (regardless of their energy gap $E = \hbar\omega_0$) will be refocused is $t = 2\bar{\tau}_{12}$ and this determines the echo's peak position (if the echo signal has a reasonable shape, which is not always true [52]). The measured echo amplitude's contribution from the magnetic ATS is therefore (allowing for an arbitrary amplification factor A_0):

$$\begin{aligned} \Delta A(\varphi) = & A_0 \frac{d}{\varepsilon_0 \varepsilon_r} x_{ATS} 2\pi P^* \int_0^\infty dE \int \frac{dD}{D} \int \frac{dD_0}{D_0} \Theta(D, D_0) \\ & \times \delta\left(E - \sqrt{D^2 + D_0^2 \varphi^2}\right) \Delta\delta_{||}(2\bar{\tau}_{12}) \end{aligned} \quad (75)$$

where d is the sample's thickness, $\Theta(D, D_0)$ is the usual theta-function restriction for the integration domain (previous Sections) and where a final orientational averaging wrt the angle $\beta = \widehat{\mathbf{B}\mathbf{S}_\Delta}$ (defining the A-B phase φ , see Eq. (7)) is in order. At this point one deals with the delta-function's constraint and the energy parameters integrations in the usual way, to arrive at, after a lengthy calculation [59]:

$$\begin{aligned} \Delta A(\varphi) \cong & -A_0 \frac{d}{\varepsilon_0 \varepsilon_r} x_{ATS} \frac{4\pi\hbar^2 P^*}{F_0} \cos(\omega\Delta\tau) \\ & \times \int_{E_{c_1}}^{E_{c_2}} \frac{dE}{E} \int_{D_{min}}^{D_2(\varphi)} \frac{dD}{D} \tanh\left(\frac{E}{2k_B T}\right) \frac{E^2}{E^2 - D^2} \\ & \cdot e^{-w^2 \bar{\tau}_{12}} \Omega_R^2 \sigma(E) [S(\theta_1, \theta_2) \tan(\omega\Delta\tau) + C(\theta_1, \theta_2)] \\ & + \int_{E_{c_2}}^\infty \frac{dE}{E} \int_{D_1(\varphi)}^{D_2(\varphi)} \frac{dD}{D} (\text{same integrand as above...}) \end{aligned} \quad (76)$$

where we have defined the functions:

$$\begin{aligned} \sigma(E) = & \frac{\Omega_R^2}{2\hbar\Omega_G^3} = \frac{\Omega_R^2}{2\hbar\left(\Omega_R^2 + (\omega_0 - \omega)^2\right)^{3/2}} \\ S(\theta_1, \theta_2) = & \sin(\Omega_G\tau_1) \sin^2(\Omega_G\tau_2/2) \\ C(\theta_1, \theta_2) = & -2\frac{\omega_0 - \omega}{\Omega_R} \sin^2(\Omega_G\tau_1/2) \sin^2(\Omega_G\tau_2/2) \end{aligned} \quad (77)$$

with $\theta_{1,2} = \Omega_G\tau_{1,2}$ the so-called pulse areas. $E_{c_{1,2}}$ are as in the previous Sections, whilst $D_{1,2}(\varphi) = \sqrt{E^2 - D_{max,min}^2 \varphi^2}$ and $E = \hbar\omega_0$.

In going from Eq. (73) to Eq. (76) we have tacitly made some assumption on the (fully averaged) spectral diffusion term $e^{-i\int_0^{2\bar{\tau}_{12}} \Delta\omega(t')s(t')dt'}$. The theory of spectral diffusion (SD) for the magnetic multi-welled ATS is a chapter still open, however we can safely assume that what was found by many Authors for NMR's spin-echoes and for the 2LS polarization echoes in glasses holds for the ATS as well. Namely, that there is a wide range of waiting times where the decay of the echo amplitude is a simple exponential in τ_{12} so that one can replace the SD term with $e^{-2\bar{\tau}_{12}/\tau_\varphi}$, where $\tau_\varphi(T)$ is a SD characteristic time depending only on temperature. There must be a SD time $\tau_{\varphi(3)}$ for the ATSs as well as a SD time $\tau_{\varphi(2)}$ for the standard 2LSs' ensemble. For the latter, theory shows [67, 68] that this parameter is independent of the energy gap E and thus for the ATS we shall assume the same and, moreover, that (like for the phonon damping rate and Rabi frequency) its dependence on the magnetic field is weak or absent. This allows us to lump the SD problem together with phonon damping, yielding an overall exponential relaxation rate:

$$w(E, D) = \tau_\varphi^{-1} + \tau^{-1}(E, D) \quad (78)$$

in which the SD time is typically much shorter than the phonon-damping time τ and depends only on temperature through:

$$\tau_\varphi(3)^{-1} = c_{ATS} T \quad (79)$$

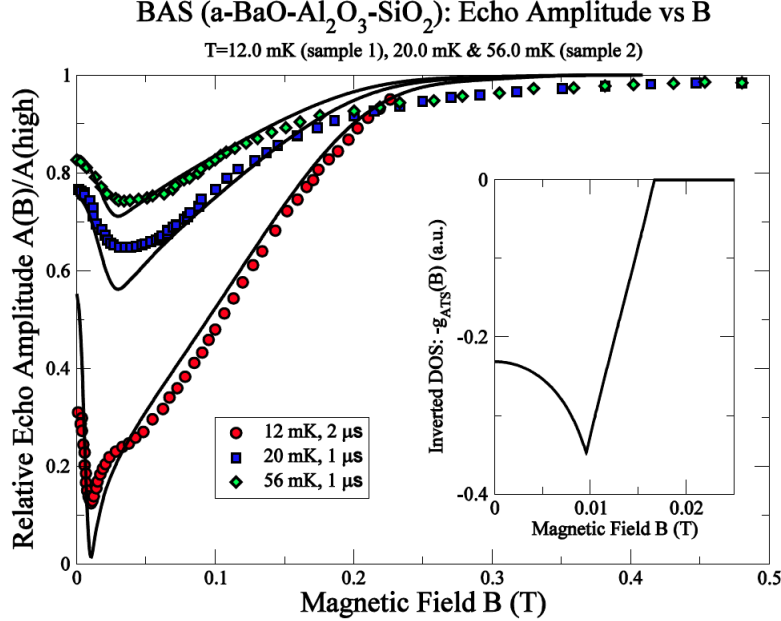


Figure 16: (colour online) Magnetic field dependence of the polarization echo amplitude (relative to its value at “high” fields where saturation occurs) for the AlBaSiO glass [62] (also referred to as BAS) at given experimental conditions. We believe two separate samples have been used. Continuous curves from our theory. Nominal frequency 1 GHz, $\tau_2 = 2\tau_1 = 0.2$ μ s. Inset: behaviour of the ATS DOS for the same parameters (the physical origin of the effect).

with c_{ATS} an appropriate constant. The assumption of an overall simple-exponential decay of the echo amplitude with τ_{12} is well verified experimentally [70].

We now make use of Eq. (76) to fit the experimental data for the multi-silicates, the idea being that the total amplitude is $A(\varphi) = A_{2\text{LS}} + \Delta A(\varphi)$ (which must be averaged wrt the ATS magnetic orientation angle β). Fig. 16 shows the experimental results for the relative echo amplitude in AlBaSiO (BAS glass) as a function of the magnetic field; values of B up to 0.6 T have been explored and for three temperatures. The data are fitted with our theory with parameters as reported in Table 8. The agreement between theory and experiment is highly satisfactory, given the simplifications used in the theory. There is only one minimum in $A(B)$ and the inset in Fig. 16 shows that again it is the ATS density of states (DOS) that is responsible for the magnetic effect (Section 3). Indeed, by enforcing the strict-resonance condition $\sigma(E) \rightarrow \delta(E - \hbar\omega)$ Eq. (76) collapses to a quantity very much like the DOS (convoluted with slow-varying corrections) and with the same behaviour, thus reproducing the main shape of $\Delta A(B)$. It is the non-resonant convolution of this quasi-DOS with other E -dependent functions that produces the rounding of the minimum and the B^{-2} saturation. Interestingly, though $\tau_\phi \ll \tau$, the phonon-damping term plays a main role in the rounding of the high- B tail to a B^{-2} (as observed) saturation. The ATS approach predicts also a linear in B intermediate decay regime of the echo amplitude, and this is often experimentally observed. Next, in Fig. 17 we present the comparison of theory and experiment for data for the echo amplitude in BK7 (good optical glass, hence devoid of true microcrystals, but nevertheless containing RERs) at two different values of the waiting time τ_{12} . It is remarkable how our theory, despite the simplifications and the total absence of multi-level physics (as advocated by the NEQM approach), can reproduce all the features of the experimental data, including every change of curvature in $A(B)$ vs. B . A rough fit, not aiming at high χ^2 agreement, reproduces the two maxima (and minima) that the NEQM approach takes as indication of the multiple (rapid) oscillations ensuing from the quantum beatings due to the Zeeman- and NEQM-splitting of the generic 2LS [63]. There are never more than two observed minima, in practice, and these can be reproduced by our simple ATS model. Finally, in the inset of Fig. 17, we show what the experimentalists missed by not exploring higher magnetic-field values. Using the simple-minded correction for the lower energy gap at higher fields, we plot the expected behaviour of $A(B)$ for intermediate fields. After the two minima, there is only an apparent saturation and new interesting features should characterise $A(B)$ at higher fields ($B > 600$ mT), just like it

BK7: Echo Amplitude vs B (T=12 mK)

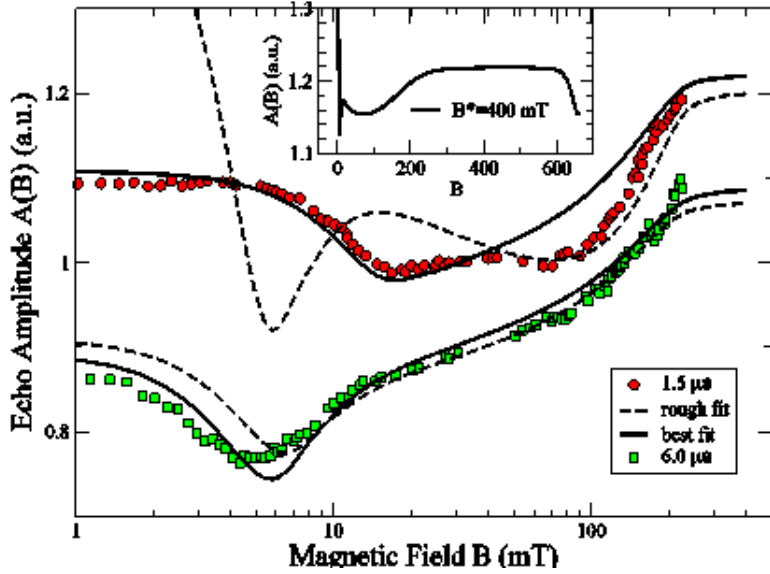


Figure 17: (colour online) Magnetic field dependence of the polarization echo amplitude for the BK7 glass [62] at given experimental conditions. Dashed curves (rough fit) and continuous curves from our theory; there are no more than two observable maxima or minima (no true oscillations). Nominal frequency 0.9 GHz, $\tau_2 = 2\tau_1 = 0.2 \mu\text{s}$. Inset: our prediction for the higher magnetic field regime (B^* as defined in Section 5).

Glass type	D_{min} (mK)	$D_{0min} \frac{q}{e} S_\Delta$ (K \AA^2)	$D_{0max} \frac{q}{e} S_\Delta$ (K \AA^2)	$\Gamma^{-1} (\mu\text{sK}^5)^{-1}$	$c_{ATS} - c_{2LS}$ (μsK) $^{-1}$	$p_1 F_0$ D kV m $^{-1}$	$\tan \omega \Delta \tau$
AlBaSiO (sample 1)	17.74	0.95×10^3	2.13×10^4	9.22×10^6	5.008	0.461	0.247
AlBaSiO (sample 2)	27.20	1.14×10^3	8.96×10^3	2.57×10^5	3.825	0.450	0.245
BK7 (1.5 μs)	16.76	0.92×10^3	1.34×10^4	8.91×10^6	1.03 (*)	0.60	0.207
BK7 (6 μs)	15.94	0.89×10^3	3.31×10^4	3.25×10^6	5.72 (*)	0.98	0.204

Table 8: Fitting parameters for the echo amplitude's magnetic field dependence. (*) For BK7 (best-fit parameters only), c_{ATS} only is involved.

happens for the dielectric constant (Section 5). A full description of the effect, however, requires a calculation involving all three ATS energy levels.

6.3 Amorphous glycerol and the so-called isotope effect

We now come to the astonishing case of amorphous glycerol ($\text{C}_3\text{O}_3\text{H}_8$ vitrifies around $T_g \simeq 47$ K), deuterated and natural. The first question is whether our model applies to this system, which nominally is single-component. We firmly believe it does and therefore that the *a*-glycerol polarization echo experiments can also be explained by the presence of RERs/micropahsing in the samples.

In Brandt's Ph.D. dissertation [69] it is reported that the liquid glycerol, from which the glass samples were made of, were contaminated by water (see Table 9). Moreover, experiments on samples with different deuterium molar content and different before-cooling open-air shelf-storage times gave definitely different results. The available experimental data are reported in Fig. 18. One observes a much greater variation in the experimental data for the $\text{C}_3\text{O}_3\text{D}_3\text{H}_5$ samples left in the air before freezing than in the similarly prepared

Sample	Chemical purity	Water content
glycerol-d ₀	99.9%	ppm H ₂ O
glycerol-d ₃	99%	= 1.5% H ₂ O
glycerol-d ₅	98%	= 0.11% H ₂ O
glycerol-d ₈	98%	no information

Table 9: Purity and water-contents data for the studied glycerol samples.

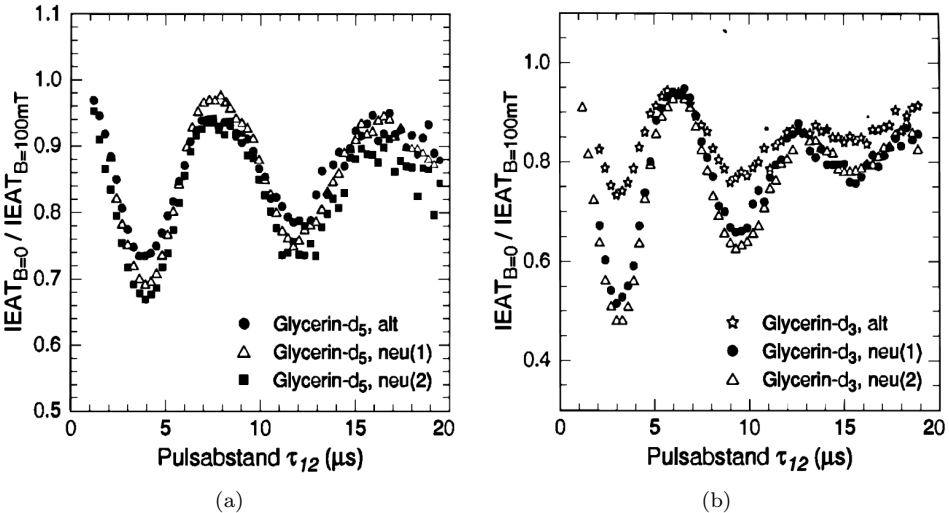


Figure 18: (colour online) Relative integrated echo amplitude vs. τ_{12} for various deuterated amorphous glycerol samples at $B = 0$, nominal frequency 0.85 GHz, $T = 13.5$ mK. The samples termed “old” (alt) were left liquid several days in the air before cooling; two separate fresh preparations (neu(1) and neu(2)) were also employed, obtained from producer-sealed containers just before cooling. From [69].

$\text{C}_3\text{O}_3\text{D}_5\text{H}_3$ samples.

Glycerol is a highly hydroscopic substance, owing to the polarity (similar to H₂O’s) of its molecules which tend to shed one of the three hydrogens (or deuterium) attached to the oxygens, but none of those firmly attached to the carbon atoms. The equilibrium process is of the type, e.g., $\text{C}_3\text{O}_3\text{D}_3\text{H}_5 \longleftrightarrow \text{C}_3\text{O}_3\text{D}_2\text{H}_5^- + \text{D}^+$ causing similar equilibrium concentrations as in the familiar dissociation process $\text{H}_2\text{O} \longleftrightarrow \text{OH}^- + \text{H}^+$. Thus it is not unreasonable to imagine that the water contained in the air causes some hydrogens to substitute for some O-attached deuterium, in time, when absorbed in liquid glycerol-d₃, - but not in the case of glycerol-d₅. The glycerol-d₃ hydroscopic effect on the echo would support the NEQM theory, but the (albeit smaller) effect in glycerol-d₅ does not. Moreover, oddly enough the more hydroscopically contaminated samples (“alt”) yield the smaller effect on the echo’s amplitude oscillations, whilst the fresher samples (“neu” (1) and (2) give wider and different (neu(1) \neq neu(2)) amplitude oscillations.

The lack of reproducibility of the effect leads us to believe that the origin of the observed magnetic phenomena lies again in the formation of RERs/microcrystallites during the freezing process, which in glycerol are nucleated by the presence of dissociated H₂O. The concentration of micro- or nano-crystals is therefore very much sample-dependent.

We remark from further tests [53] that (Section 9) the number of coherently tunneling ions (most probably D⁺ in glycerol-d₃) may be large and/or that the electric-field intensity (unknown for the glycerol experiments) may also be huge (thus renormalizing the value of D_{min} way upwards).

The lack of reliable experimental dielectric data for amorphous glycerol makes the fitting of the polarization-echo data frustrating. All the more so, when considering that – so far – no evidence for a magnetocapacitance effect in a-glycerol has been found (albeit at the nominal frequency of 0.986 GHz) [69]. This last fact, however, could be explained by the suspected large value of D_{min} , for the order of magnitude of the magnetocapacitance is given, in our theory, by the combination $\pi P^* p_1^2 x_{ATS} / (2\epsilon_0 \epsilon_r D_{min})$ (Section 5) and for a-glycerol $\epsilon_r = 42.5$ and D_{min} are much larger than for the multi-silicates. Low-frequency (kHz range) and weak electric-field

intensity measurements of the dielectric constant of a-glycerol would be most useful. These lacking, we must limit our discussion of the magnetic dipole echo phenomena in a-glycerol to the qualitative level of understanding.

The integrated echo amplitude, IEA, is readily obtained from Eq. (73), after the averaging procedure as in Eq. (75) and a subtraction of the pump-frequency mode ω are carried out (rotating reference frame description):

$$\begin{aligned} \Delta IEA(\varphi) \cong & -A_0 \frac{d}{\varepsilon_0 \varepsilon_r} x_{ATS} \frac{4\pi \hbar^2 P^*}{F_0} \\ & \times \left\{ \int_{E_{c_1}}^{E_{c_2}} \frac{dE}{E} \int_{D_{min}}^{D_2(\varphi)} \frac{dD}{D} \tanh\left(\frac{E}{2k_B T}\right) \frac{E^2}{E^2 - D^2} \Omega_R^2 \sigma(E) \frac{2w}{w^2 + (\omega_0 - \omega)^2} \right. \\ & \times [S(\theta_1, \theta_2) \cos(2(\omega_0 - \omega)\tau_{12}) + C(\theta_1, \theta_2) \sin(2(\omega_0 - \omega)\tau_{12})] \\ & \left. + \int_{E_{c_2}}^{\infty} \frac{dE}{E} \int_{D_1(\varphi)}^{D_2(\varphi)} \frac{dD}{D} (\text{same integrand as above...}) \right\} \end{aligned} \quad (80)$$

with $\sigma(E)$, w , S and C as in Eqs. (78,78) above. We are now in the presence of an even narrower spectral delimiter than $\sigma(E)$:

$$\chi(E) = \frac{w}{\pi \hbar (w^2 + (\omega_0 - \omega)^2)} \quad (81)$$

is a (normalized) very sharply-peaked function of $E = \hbar\omega_0$ since $w \ll \Omega_R \ll \omega$. We can then take the limit $p_1 F_0 \rightarrow \infty$ that seems to be appropriate for the glycerol experiments and replace $\sigma(E)$ by a constant, $\sigma(E) \rightarrow (2\hbar\Omega_R)^{-1}$, to get:

$$\begin{aligned} \Delta IEA(\varphi) \approx & -A_0 \frac{d}{\varepsilon_0 \varepsilon_r} x_{ATS} \frac{2\pi^2 \hbar^2 P^*}{F_0} \\ & \times \left\{ \int_{E_{c_1}}^{E_{c_2}} \frac{dE}{E} \int_{D_{min}}^{D_2(\varphi)} \frac{dD}{D} \tanh\left(\frac{E}{2k_B T}\right) \frac{E^2}{E^2 - D^2} \right. \\ & \cdot \Omega_R \chi(E) S(\theta_1, \theta_2) \cos(2(\omega_0 - \omega)\tau_{12}) \\ & \left. + \int_{E_{c_2}}^{\infty} \frac{dE}{E} \int_{D_1(\varphi)}^{D_2(\varphi)} \frac{dD}{D} (\text{same integrand as above...}) \right\} \end{aligned} \quad (82)$$

For fixed and large τ_{12} the above is essentially the energy convolution of a function very much like the DOS $g_{ATS}(E)$ times some slowly-varying functions of E and the sharply-peaked spectral delimiter $\chi(E)$. The result of this convolution is depicted in Fig. 19 and very much depends on whether $D_{min} < \hbar\omega$ or $D_{min} > \hbar\omega$. In the first case, the evolution of the $g_{ATS}(E)$ with φ (or B) gives rise to a sizable magnetic effect on the echo amplitude (or IEA) even in the strict-resonant limit, whilst in the second case, $D_{min} > \hbar\omega$, the magnetic effect is drastically reduced and completely vanishes in the strict resonant limit, $\chi(E) \rightarrow \delta(E - \hbar\omega)$.

This is the explanation for the so-called isotope effect in amorphous glycerol, which actually is a mere mass-substitution effect. Indeed, we claim that for natural glycerol the situation $D_{min} > \hbar\omega$ applies and that for the deuterated samples, as for the multi-silicates, $D_{min} < \hbar\omega$ applies instead. Then, D_{min} is roughly given by (Section 3):

$$D_{min} \approx \frac{1}{2} \hbar \sqrt{\frac{k}{M}} \quad \text{moreover: } D_0 \approx \hbar \sqrt{\frac{k}{M}} e^{-\frac{d}{\hbar} \sqrt{2M} V_0} \quad (83)$$

where k is the bonding constant that depends only on the chemistry and not on the isotope's mass, M . Thus we immediately see that $D_{min}(\text{deuterium}) = D_{min}(\text{hydrogen})/\sqrt{2}$ and this is sufficient to make the transition from case b) to case a) in Fig. 19 when a substantial mass change of the tunneling particles through isotopic substitution is made. The case of partial isotopic substitution requires separate considerations. A further consequence of mass substitution, as seen in Eq. (83), is that a larger mass M will make – the chemistry being unchanged – the parameters $D_{0min, max}$ much smaller and thus will give rise to a much slower variation of the echo's amplitude with B , as is indeed verified in the experiments (Fig. 14). The highly non-uniform shape of the DOS for the ATS model thus qualitatively (and for the multi-silicates also quantitatively) explains all of the experimental findings.

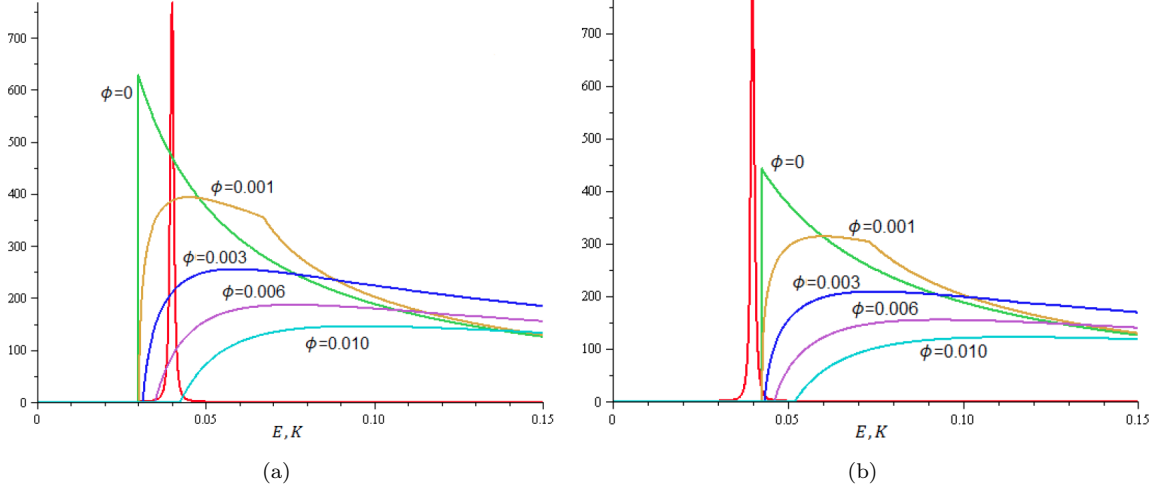


Figure 19: (colour online) Convolution of the DOS $g_{ATS}(E, \varphi)$ and the spectral delimiter $\chi(E)$ in the integral giving the IEA. a) If $D_{min} < \hbar\omega$ there is a significant effect on the echo amplitude as φ increases; b) In the opposite case $D_{min} > \hbar\omega$ the effect is much reduced and vanishes in the strict resonant case. This is our qualitative explanation for the “isotope effect” [59].

The last topic we discuss is our explanation for the dramatic effect for the echo’s IEA dependence on the waiting time τ_{12} near $B = 0$ [59]. To explain this we take the $B \rightarrow 0$ limit of Eq. (82), when only the second term contributes and we get, evaluating the D -integral exactly and lumping all slowly-varying functions into an overall constant \mathcal{A}^* :

$$\lim \Delta IEA(\varphi) \approx -\mathcal{A}^* \int_{D_{min}}^{\infty} \frac{dE}{E} \tanh\left(\frac{E}{2k_B T}\right) \ln\left(\left(\frac{D_{0max}}{D_{0min}}\right)^2 \frac{E^2 - D_{0min}^2 \varphi^2}{E^2 - D_{0max}^2 \varphi^2}\right) \times \chi(E) \cos(2(\omega_0 - \omega)\tau_{12}) \quad (84)$$

Inspection of this last expression shows, that the ATS contribution decreases quadratically as the AB phase (or the magnetic field) increases; hence, the disappearance of the oscillations in τ_{12} is slow (as experimentally reported [62]) for very weak but increasing B . To understand the oscillations themselves (and their absence for the silicates) we set $B = 0$ and redefining the overall constant we arrive at (since τ_ϕ is the shortest decay time involved):

$$\lim \Delta IEA(0) \approx -\mathcal{B}^* \int_{D_{min}}^{\infty} \frac{dE}{E} \frac{\tau_\varphi^{-1}}{\pi \hbar [\tau_\varphi^{-2} + (\omega_0 - \omega)^2]} \cos(2(\omega_0 - \omega)\tau_{12}) \quad (85)$$

(\mathcal{B}^* being another overall constant). The remaining integral can be rewritten as an integral in the interval $[0, \infty]$, which yields an exponentially decaying contribution in τ_{12} , plus the integral in the energy interval $[0, \hbar\omega - D_{min}]$. The latter is responsible for the oscillations in τ_{12} since:

$$\int_0^b dx \frac{\cos x}{x^2 + a^2} = \frac{\pi}{2a} e^{-a} + \text{Im} \left\{ \frac{e^{-a}}{2a} \text{Ei}(-a + ib) - \frac{e^a}{2a} \text{Ei}(a + ib) \right\} \quad (86)$$

where $\text{Ei}(z)$ denotes the exponential-integral function. Rearranging Eq. (85), also adding the 2LS standard exponentially decaying contribution, we come to the following functional form for the total IEA of the sample:

$$\begin{aligned} \lim IEA(0) \approx & C_{2LS} e^{-\frac{2\tau_{12}}{\tau_{\varphi(2)}}} + C_{ATS} \frac{\tau_{\varphi(3)}}{\tau_{12}} e^{-\frac{2\tau_{12}}{\tau_{\varphi(3)}}} \\ & + K_{ATS} \text{Im} \left\{ \frac{e^{-a}}{2a} \text{Ei}(-a + ib) - \frac{e^a}{2a} \text{Ei}(a + ib) \right\} \end{aligned} \quad (87)$$

where C_{2LS} , C_{ATS} and K_{ATS} are appropriate constants and where:

$$a = 2\tau_{12}\tau_{\phi(3)}^{-1} \quad b = 2\tau_{12} \left(\omega - \frac{D_{min}}{\hbar} \right) \quad (88)$$

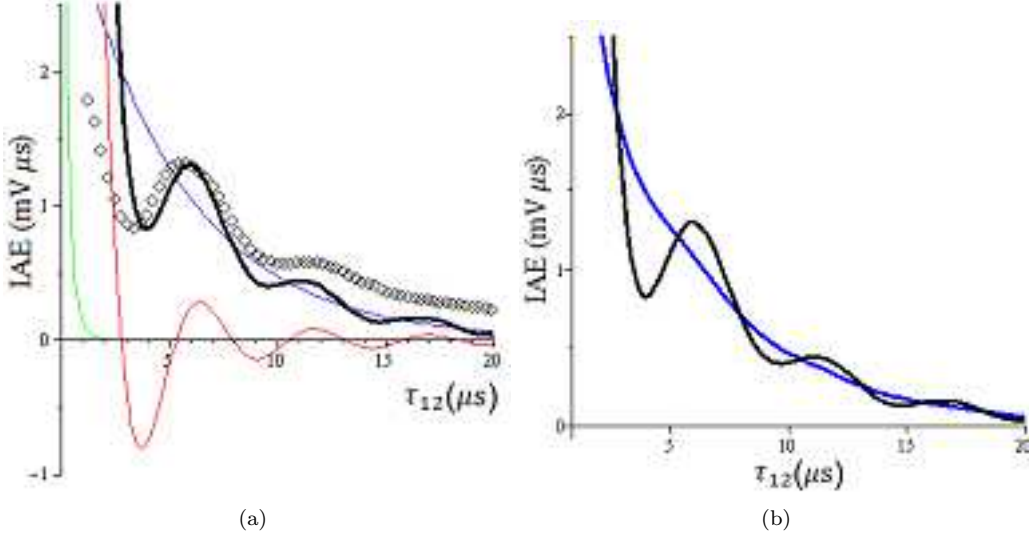


Figure 20: (colour online) The IAE from Eq. (87) plotted as a function of τ_{12} for parameters as in the text. a) The simplified theory almost reproduces (black curve) the experimental data (diamonds) for glycerol-d₃ at $B = 0$, nominal frequency $\omega/2\pi = 0.887$ GHz and $T = 13.5$ mK [9] (blue curve: – 2LS contribution, green and red curves: – ATS contributions, black curve: – sum of 2LS and ATS contributions); b) Disappearance of the IAE oscillations when $\tau_{\phi(3)}$ decreases or $\Delta\omega$ increases (blue curve). From [53].

We plot expression (87) in Fig. 20 as a function of τ_{12} , assuming some reasonable value of $\tau_{\phi(3)} = 1.0$ μs for the ATS spectral-diffusion time, $\tau_{\phi(2)} = 10.0$ μs for the 2LS one, and of $\Delta\omega = \omega - \frac{D_{min}}{\hbar} = 0.6$ MHz for the frequency offset. As is shown in Fig. 20(a) (black curve), this (over)simplified theoretical treatment almost reproduces the data for glycerol-d₃ at $B = 0$. Fig. 20(b) also shows (blue curve) that reducing to $\tau_{\phi(3)} = 0.3$ μs causes the oscillations to disappear; alternatively, this can be achieved by increasing $\Delta\omega$.

This treatment also explains the findings in Fig. 18. Leaving the sample in the air causes a change in D_{min} simply because more RERs or micro-crystals are nucleated (hence a larger $\Delta\omega$) by the absorbed water vapour, but also because of mass substitution through dissociation. The subtle role of the true value of the resonating frequency ω (the sample sits in a reentrant resonating cavity which is loaded with a reacting dielectric and thus develops its own resonance frequency) is as yet not completely understood.

Clearly, if $\Delta\omega < 0$ (case of glycerol-d₀) there can only be exponential decay (from the 2LS contribution, mostly), but if $\Delta\omega > 0$ is also too large the oscillations die out. We believe this is the case for the multi-silicates.

Qualitatively at least, our ATS model explains all experimental observations so far. In terms of the parameters used for the best fits, one cannot fail to notice (see Table 8) that for the echo experiments the values of the cutoffs for the combination of parameters $D_0 \frac{q}{e} S_{\Delta}$ are about one order of magnitude lower than for the other experiments, C_p and ϵ , carried out inside higher temperature ranges, in fact. This can be explained by a mechanism whereby the number N of atomic tunneling systems within each ATS (hence within the interstices between the RERs or micro-crystals) picks up a temperature dependence $N(T)$.

7 The Magnetic Field Dependent SQUID-Magnetization

7.1 Theory

Having obtained qualitatively (and also quantitatively, barring the various approximations applied) good fits to the C_p , ϵ and A_{echo} experimental data with the ATS contributions added to the 2LS's (and when appropriate to the paramagnetic impurities'), we address the question of why the values of $D_0 \frac{q}{e} S_{\Delta}$ are so high. The first conclusion is that the ATSs now appear to carry considerably high magnetic moments μ_{ATS} *per se*. Estimating from the definition ($T = 0$) $\mu_{\text{ATS}} = -\frac{\partial}{\partial B} \left(-\frac{1}{2} E \right)$, where $E = \sqrt{D^2 + D_0^2 \varphi^2}$ is the ATS lower energy gap, we get for not too small fields B (μ_{ATS} vanishes linearly with B when $B \rightarrow 0$, but saturates

at high enough B):

$$\mu_{ATS} \simeq \frac{\pi}{\Phi_0} SD_0 = \frac{\pi}{\phi_0} \left(\left| \frac{q}{e} \right| SD_0 \right). \quad (89)$$

Thus the very same combination $\frac{q}{e} SD_0$ of parameters appears, whilst $\phi_0 \equiv h/e$ is the electronic magnetic flux quantum. Using the values extracted from the C_p best fit (e.g. Table 4) we deduce from Eq. (89) that (for Duran) μ_{ATS} ranges from about $3.8\mu_B$ to $27.1\mu_B$. This fact alone indicates that a large group of correlated charged atomic particles is involved in each single ATS and that an important ATS contribution to the sample's magnetization is to be expected (Fe²⁺ and Fe³⁺ have magnetic moment $\mu_J = 2\sqrt{6}\mu_B$ and $\sqrt{35}\mu_B$, respectively).

The magnetization M of a sample containing dilute paramagnetic impurities as well as dilute magnetic-field sensitive ATSs is, like C_p , also given by the sum of two different contributions:

- a. Langevin's well-known paramagnetic impurities' contribution (Fe²⁺ and Fe³⁺, with n_J concentration of one species having spin J), given by the standard expression [71]

$$M_J = n_J g \mu_B J B_J(z), \quad \left(z = \frac{g \mu_B B J}{k_B T} \right) \quad (90)$$

where the Brillouin function B_J is defined by:

$$B_J(z) = \frac{2J+1}{2J} \coth \left(\frac{(2J+1)}{2J} z \right) - \frac{1}{2J} \coth \left(\frac{1}{2J} z \right) \quad (91)$$

and its low-field susceptibility is the known Curie law:

$$\frac{M}{B} \cong \frac{n_J g^2 \mu_B^2 J (J+1)}{3k_B T} \quad (92)$$

- b. the ATS tunneling currents' contribution, given by the following novel expression as the sum of contributions from ATSs of lowest gap E :

$$M_{ATS} = \pi P^* n_{ATS} \frac{1}{B} \left\{ \int_{E_{c1}}^{E_{c2}} dE \tanh \left(\frac{E}{2k_B T} \right) \ln \left(\frac{E^2 - D_{0min}^2 \varphi^2}{D_{min}^2} \right) \right. \\ \left. + \int_{E_{c2}}^{\infty} dE \tanh \left(\frac{E}{2k_B T} \right) \ln \left(\frac{E^2 - D_{0min}^2 \varphi^2}{E^2 - D_{0max}^2 \varphi^2} \right) \right\} \quad (93)$$

and which can be also re-expressed (like in the case of C_{ATS}) using $y = \frac{E}{2k_B T}$ in the following form:

$$M_{ATS} = 2\pi P^* n_{ATS} k_B T \frac{1}{B} \left\{ \int_{x_{c1}}^{x_{c2}} dy \tanh y \ln \left(\frac{y^2 - x_{0min}^2 \varphi^2}{x_{min}^2} \right) \right. \\ \left. + \int_{x_{c2}}^{\infty} dy \tanh y \ln \left(\frac{y^2 - x_{0min}^2 \varphi^2}{y^2 - x_{0max}^2 \varphi^2} \right) \right\} \quad (94)$$

with, as before:

- $E_{c1} = \sqrt{D_{min}^2 + D_{0min}^2 \varphi^2}$ and $E_{c2} = \sqrt{D_{min}^2 + D_{0max}^2 \varphi^2}$;
- $x_{c1,2} = \frac{E_{c1,2}}{2k_B T}$, $x_{min} = \frac{D_{min}}{2k_B T}$, etc.;

We present this expression here for the first time, also motivated by the fact that we expect a contribution to the measured magnetization M from the ATSs that is comparable to, or even greater than, Langevin's paramagnetism of the diluted Fe impurities. The above expression follows from a straightforward application of standard quantum statistical mechanics, with

$$\mathbf{M}_{ATS} = n_{ATS} \left\langle -\frac{\partial \mathcal{H}_{3LS}}{\partial \mathbf{B}} \right\rangle,$$

n_{ATS} being the ATSs' concentration (a parameter always lumped together with P^*) and with \mathcal{H}_{3LS} given by Eq. (6). The angular brackets $\langle \dots \rangle$ denote quantum, statistical and disorder averaging.

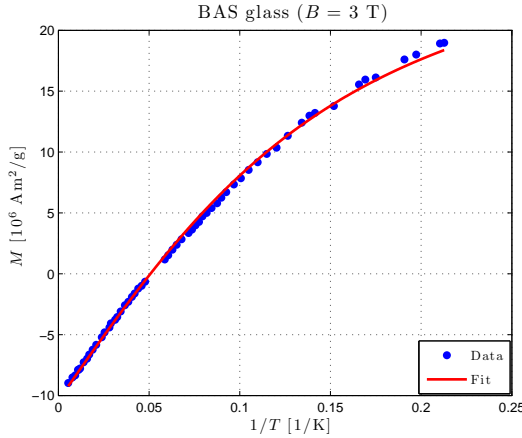


Figure 21: (colour online) The best fit of the magnetization data [48] for the BAS glass, using Eq. (90) (for the Fe^{2+} and Fe^{3+} impurities) and Eq. (94) (for the ATSs).

The above formula for M_{ATS} is in fact correct for weak magnetic fields. For higher fields the correction implied by Eq. (20) has to be implemented and it corresponds to an improved analytic expression for the lowest ATS gap:

$$E = \sqrt{D^2 + D_0^2 \varphi^2 \left(1 - \frac{1}{27} \varphi^2\right)} \quad (95)$$

which needs to be used for high fields [53]. In practice, as seen in Eq. (20), this corresponds – where appropriate – to the replacement of B with $B\sqrt{1 - \frac{1}{45}(B/B^*)^2}$. A full derivation and the study of the B - and T -dependence of M_{ATS} will be presented elsewhere. Here, it suffices to say that temperature-dependent fitting parameters are necessary to achieve good fits for $M(T)$ in such wide temperature range ($4 < T < 300$ K). The underlying physical reason is that as temperature drops the RERs of the cellular structure of the glass (Section 2) begin to fuse together and adsorb atoms/ions from the interstices between them, growing at their expense. As a result the number $N(T)$ of atomic tunnelers in each interstitial ATS decreases with decreasing temperature: $T_g > T \rightarrow 0$ and a reasonable temperature-dependence is of the Arrhenius type:

$$N(T) = N_0 \exp \left\{ -\frac{E_0}{k_B T} \right\}, \quad (96)$$

where E_0 is a suitable activation energy. Then, advocating coherent tunneling of the group of $N(T)$ atomic tunnelers making up each interstitial ATS [46] we must use the temperature dependent parameters:

$$\begin{aligned} D_{min} &= D_{min}^{(0)} \exp \left\{ -\frac{E_0}{k_B T} + \frac{E_0}{k_B T_0} \right\} \\ D_{0min} \frac{q}{e} S_{\Delta} &= \left[D_{0min} \frac{q}{e} S_{\Delta} \right]^{(0)} \exp \left\{ -\frac{3E_0}{k_B T} + \frac{3E_0}{k_B T_0} \right\} \\ D_{0max} \frac{q}{e} S_{\Delta} &= \left[D_{0max} \frac{q}{e} S_{\Delta} \right]^{(0)} \exp \left\{ -\frac{3E_0}{k_B T} + \frac{3E_0}{k_B T_0} \right\} \end{aligned} \quad (97)$$

and a similar one for B^* , containing two parameters proportional to $N(T)$ in Eq. (96). Here, T_0 is a temperature corresponding to the parameters' combinations marked with a (0)-superscript and the values we extract from the best fits below correspond to parameters at that temperature (typically, T_0 is the average temperature of our C_p fits in Section 4).

7.2 Comparison with available data

The magnetization data [48] were best-fitted with Eq. (90) (for the Fe^{2+} and Fe^{3+} contributions) as well as with Eq. (94) (for the ATSs'), using the parameters from the C_p -fits as input. The best fit for the BAS glass is reported in Fig. 21 and the extracted parameters in Table 10.

Parameter	BAS glass
$n_{Fe^{2+}} [g^{-1}]$	1.08×10^{17}
$n_{Fe^{3+}} [g^{-1}]$	5.01×10^{16}
$P^* n_{ATS} [g^{-1}]$	5.74×10^{16}
$D_{min} [K]$	8.01×10^{-2}
$D_{0min} \frac{q}{e} S [\text{K}\text{\AA}^2]$	1.31×10^5
$D_{0max} \frac{q}{e} S [\text{K}\text{\AA}^2]$	2.44×10^5
$B^* [T]$	1.02
$E_0 [K]$	0.42
vert.offset [$\text{Am}^2 \text{g}^{-1}$]	-1.04×10^{-5}

Table 10: Extracted parameters (from the magnetization data of [48]) for the concentration of ATS and Fe-impurities of the BAS glass. The vertical offset represents the residual Larmor diamagnetic contribution.

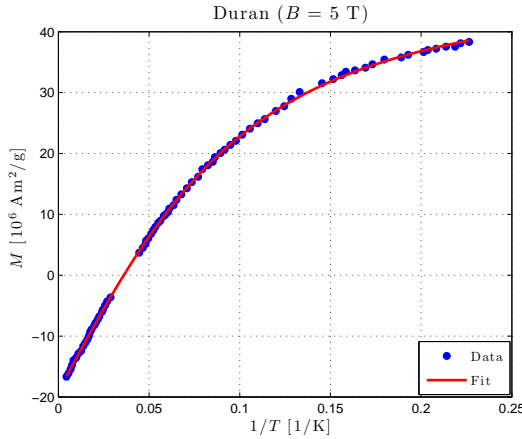


Figure 22: (colour online) The best fit of the magnetization data [48] of Duran, using Eq. (90) (for the Fe^{2+} and Fe^{3+} impurities) and Eq. (94) (for the ATSs).

Parameter	Duran
$n_{Fe^{2+}} [g^{-1}]$	3.07×10^{17}
$n_{Fe^{3+}} [g^{-1}]$	2.13×10^{17}
$P^* n_{ATS} [g^{-1}]$	8.68×10^{16}
$D_{min} [K]$	5.35×10^{-2}
$D_{0min} \frac{q}{e} S [\text{K}\text{\AA}^2]$	2.00×10^5
$D_{0max} \frac{q}{e} S [\text{K}\text{\AA}^2]$	2.81×10^5
$B^* [T]$	1.63
$E_0 [K]$	0.34
vert.offset [$\text{Am}^2 \text{g}^{-1}$]	-1.97×10^{-5}

Table 11: Extracted parameters (from the magnetization data of [48]) for the concentration of ATS and Fe impurities of Duran.

BAS glass	
Heat Capacity fit	
$n_{Fe^{2+}}$	$1.06 \times 10^{17} \text{ g}^{-1} = 14.23 \text{ ppm}$
$n_{Fe^{3+}}$	$5.00 \times 10^{16} \text{ g}^{-1} = 6.69 \text{ ppm}$
$P^* n_{ATS}$	$5.19 \times 10^{16} \text{ g}^{-1}$
Magnetization fit	
$n_{Fe^{2+}}$	$1.08 \times 10^{17} \text{ g}^{-1} = 14.38 \text{ ppm}$
$n_{Fe^{3+}}$	$5.01 \times 10^{16} \text{ g}^{-1} = 6.70 \text{ ppm}$
$P^* n_{ATS}$	$5.74 \times 10^{16} \text{ g}^{-1}$

Table 12: Comparison between the concentrations extracted from the two different best-fitted experimental data sets for the BAS glass.

The best fit for Duran is reported in Fig. 22 and the extracted parameters in Table 11. We recall how we convert the Fe-concentrations thus obtained to atomic ppm concentrations (ppma), using the formula [50]:

$$n_J = \bar{n}_J \frac{N_A}{\sum_i \xi_i A_i} \quad (98)$$

where $n_J = N_J/M$ is the mass density and $\bar{n}_J = N_J/N_{at}$ the atomic concentration of the spin- J Fe species (to be multiplied by 100 to get the ppm) and where: N_J is the number of Fe-ions in the sample with spin J ξ_i the molar fraction of the i -th species, A_i the molar mass of the i -th species, N_{at} the total number of atoms in the sample and N_A Avogadro's number ($6.022 \times 10^{23} \text{ mol}^{-1}$) for the Fe^{2+} ($J=2$) and Fe^{3+} ($J=5/2$) impurities.

The nominal concentration of Fe^{3+} for the BAS glass is (using Eq. (98)):

$$\begin{aligned} \bar{n}_{Fe_{nom}^{3+}} &= 102 \text{ ppm} \\ n_{Fe_{nom}^{3+}} &= \frac{10^{-6} \cdot 102 \cdot 6.022 \times 10^{23} \text{ mol}^{-1}}{80.530 \frac{\text{g}}{\text{mol}}} = 7.63 \cdot 10^{17} \text{ g}^{-1} \end{aligned} \quad (99)$$

which is inadequate (as in Duran's case below) to explain the behaviour of the heat capacity as a function of B , here presented (Fig. 7) and as a function of T (studied in [1]). Table 12 summarizes the concentrations found from our best fits of heat capacity and magnetization data, for the BAS glass. The parameters found in [1] were $P^* n_{ATS} = 6.39 \times 10^{16} \text{ g}^{-1}$ and $\bar{n}_{Fe} = 20.44 \text{ ppm}$ where this latter was for the Fe^{2+} concentration only. The present study confirms that most of the Fe-impurities in these two glasses are of the Fe^{2+} type [1].

The nominal concentration of Fe^{3+} for Duran is (using Eq. (98)):

$$\begin{aligned} \bar{n}_{Fe_{nom}^{3+}} &= 126 \text{ ppm} \\ n_{Fe_{nom}^{3+}} &= \frac{10^{-6} \cdot 126 \cdot 6.022 \times 10^{23} \text{ mol}^{-1}}{61.873 \frac{\text{g}}{\text{mol}}} = 1.23 \cdot 10^{18} \text{ g}^{-1} \end{aligned} \quad (100)$$

which again is inadequate to explain the behaviour of the heat capacity as a function of B (see Fig. 23). Table 13 summarizes the concentrations found from our best fits of heat capacity and magnetization data, for Duran. The parameters found in [1] were $P^* n_{ATS} = 6.92 \times 10^{16} \text{ g}^{-1}$ and $\bar{n}_{Fe} = 47.62 \text{ ppm}$ where this latter was the Fe^{2+} concentration only.

Fig. 23 presents the behaviour of the different contributions to the heat capacity as a function of B for Duran; $C_{Fe^{2+}}$ and $C_{Fe^{3+}}$ are given by Eq. (16), respectively with the Fe^{2+} and Fe^{3+} parameters, C_{param} is the sum of these latter two contributions, C_{ATS} is given by Eq. (18) and the green line represents the result of the best fit. The dashed line corresponds to the $\bar{C}_p(B)$ one would get from the nominal concentration \bar{n}_{Fe} of 126 ppm [48] as extracted from the SQUID magnetization measurements fitted with the Langevin contribution only (no ATS contribution). Likewise Fig. 24 presents the behaviour of the different contributions (Eq.(90) and Eq.(94)) to the magnetization as a function of B , also for Duran. It can be seen that the ATS contribution is in both cases dominant, also (in the case of the magnetization) at the higher temperatures. We finally present our preliminary study of the SQUID magnetization data (also available from [48]) for the borosilicate

Duran	
Heat Capacity fit	
$n_{Fe^{2+}}$	$3.21 \times 10^{17} \text{ g}^{-1} = 33.01 \text{ ppm}$
$n_{Fe^{3+}}$	$2.11 \times 10^{17} \text{ g}^{-1} = 21.63 \text{ ppm}$
$P^* n_{ATS}$	$8.88 \times 10^{16} \text{ g}^{-1}$
Magnetization fit	
$n_{Fe^{2+}}$	$3.07 \times 10^{17} \text{ g}^{-1} = 31.58 \text{ ppm}$
$n_{Fe^{3+}}$	$2.13 \times 10^{17} \text{ g}^{-1} = 21.86 \text{ ppm}$
$P^* n_{ATS}$	$8.68 \times 10^{16} \text{ g}^{-1}$

Table 13: Comparison between the concentrations extracted from the two different best-fitted experimental data sets for Duran.

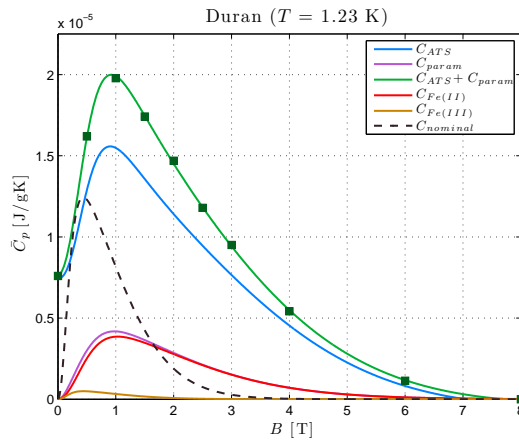


Figure 23: (colour online) The curves represent the different terms that contribute to the heat capacity of Duran in our best fit of the data from [48]. The dashed curve is for Langevin's contribution only, but with the nominal concentration of $\bar{n}_{Fe^{3+}}=126$ ppm (no ATS).

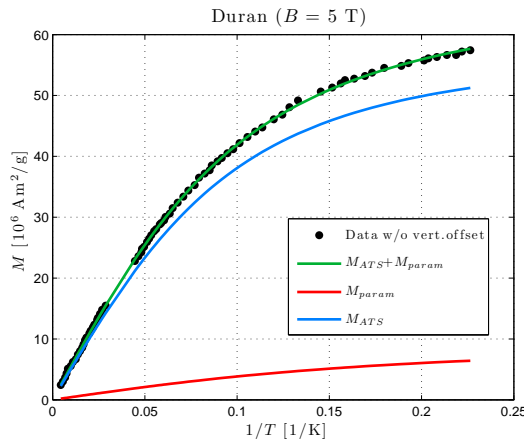


Figure 24: (colour online) The curves represent the different contributions to the magnetization of Duran in our best fit of the data from [48].

Parameter	BK7
$n_{Fe^{2+}} [\text{g}^{-1}]$	$6.69 \times 10^{15} = 0.71 \text{ ppm}$
$n_{Fe^{3+}} [\text{g}^{-1}]$	$3.43 \times 10^{15} = 0.36 \text{ ppm}$
$P^* n_{ATS} [\text{g}^{-1}]$	1.40×10^{16}
$D_{min} [\text{K}]$	5.99×10^{-2}
$D_{0min} \frac{q}{e} S [\text{K}\text{\AA}^2]$	8.87×10^4
$D_{0max} \frac{q}{e} S [\text{K}\text{\AA}^2]$	1.20×10^5
$B^* [\text{T}]$	1.30
$E_0 [\text{K}]$	0.48
vert.offset [Am^2g^{-1}]	-1.08×10^{-5}

Table 14: Extracted parameters (from the magnetization data of [48]) for the concentration of ATSs and Fe impurities of the BK7 ($\sum_i \xi_i A_i = 63.530 \text{ g mol}^{-1}$ [48]). The vertical offset represents the residual Larmor diamagnetic contribution.

glass BK7, for which however no substantial magnetic effect in the heat capacity C_p has been reported [48]. This glass has a nominal Fe-impurity concentration of $\bar{n}_{Fe^{3+}} = 6 \text{ ppm}$ [7, 48, 52], yet our best fit in Fig. 25 with both Langevin (Eq. (90)) and ATS (Eq. (94)) contributions produces the concentrations and parameters given in Table 14. The best fit was carried out with knowledge of ATS parameters from our own theory [47] for the magnetic effect in the polarization-echo experiments at mK temperatures [52]. We conclude that our main contention is once more confirmed, in that the concentration of Fe in BK7 we extract in this way is only about 1.1 ppm and the bulk of the SQUID magnetization is due to the ATSs. Table 14 reports our very first estimate of $n_{ATS} P^*$ for BK7. Assuming P^* to be of order 1 and about the same for all glasses, we conclude that the concentration n_{ATS} of the ATSs nesting in the RERs is very similar for all of the multi-silicate glasses by us studied for their remarkable magnetic effects. From the present SQUID-magnetization best fits we have obtained $5.74 \times 10^{16} \text{ g}^{-1}$ (BAS glass), $8.68 \times 10^{16} \text{ g}^{-1}$ (Duran) and $1.40 \times 10^{16} \text{ g}^{-1}$ (BK7). The almost negligible magnetic effect in C_p for BK7 is due, in our approach, to the low values of the cutoffs D_{0min} and D_{0max} for this system (these parameters appearing in the prefactor and in the integrals' bounds determining the ATS contribution to C_p [46]). We find values of the combinations of parameters $D_{0min} |\frac{q}{e}| S$ and $D_{0max} |\frac{q}{e}| S$ again as high as those extracted from C_p , ϵ and A_{echo} experimental data. We believe [46] this is to be ascribed to the coherent tunneling of an average number $N(T)$ of atomic tunnelers trapped – and strongly interacting – in each interstitial ATSs (Fig. 2).

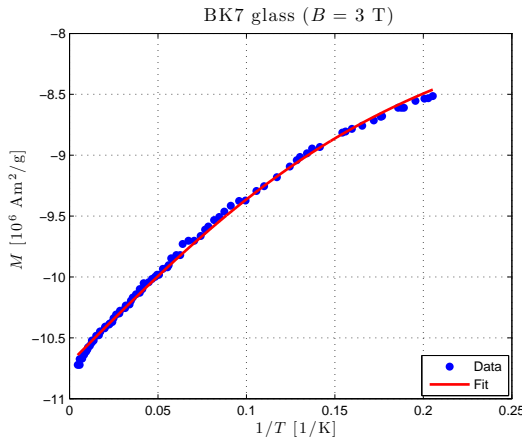


Figure 25: (colour online) The best fit of the magnetization data [48] for BK7, using Eq. (90) (for the Fe^{2+} and Fe^{3+} impurities) and Eq. (94) (for the ATSs). Data from [48].

8 Nature of the Tunneling Systems and the Potential Energy Landscape

So far we have described how the anomalous behaviour of glasses in the low temperature regime is related to localized hoppings between adjacent local configurations, through qm tunneling. The STM postulates that in the configuration space each TS can be represented by a double well potential (DWP) and makes certain assumptions regarding the distribution of its asymmetry and barrier height. Although from a qualitative point of view this picture is certainly reasonable and appealing, in practice one has to see whether in a real glass-forming system such DWPs with the right characteristics are indeed present. Through experiments, it is very difficult to obtain microscopic information about the properties of the TSs since they do not give *direct* access to the relevant information (distribution of barrier heights, asymmetry, nature of the motion of the participating particles, and so on (but see the attempts in [64, 65])).

Thus at present the only promising approach to make progress in this field are atomistic computer simulations. In the past such simulations have already helped to clarify many properties of the potential energy landscape (PEL) of glass-forming systems and allowed to understand their relaxation dynamics [72, 73, 74, 75]. (We recall that the PEL is the surface of the potential energy as a function of the $3N_{at}$ coordinates of the system, where N_{at} is the number of particles. Note that this PEL does not depend on temperature, but the regions that the system explores with a significant probability does.) One can therefore hope that such simulations will also permit to gain insight into the properties of glasses at intermediate, low, and very low temperatures. The question that has to be addressed in such simulations is whether or not one does indeed find in the PEL local DWPs that have the right features. Note that one expects that the number of local minima is exponentially large in N_{at} , i.e. it is a huge number and therefore it will be completely impossible to find all of the DWPs. Furthermore one faces the conceptual problem of how this purely classical concept of the PEL can be used to describe the tunneling processes, i.e. a quantum phenomenon. The simplest approach to address these issues is the introduction of a reaction coordinate that parametrizes the hopping from one local minimum to a neighboring one and from this to calculate the effective barrier height and thus the tunneling parameters. Subsequently this information can be fed into theoretical approaches like those discussed in the previous Sections to calculate quantities like the heat capacity C_p and so on.

First of all we have to discuss the order of magnitude of the main parameters that characterize the TSs, i.e. (for the 2LSs) the tunneling matrix element Δ_0 , the energy of the single well $\hbar\Omega$, and the barrier height V_0 .

The tunneling matrix element Δ_0 is given, for example, by Eq. (4), i.e. $\Delta_0 = \frac{1}{2}\hbar\Omega\left(3 - \sqrt{\frac{8V_0}{\pi\hbar\Omega}}\right)e^{-2\frac{V_0}{\hbar\Omega}}$. From the literature one can infer the typical range of values for the first two quantities for the most studied glasses (the multi-silicates):

- $10^{-6} \text{ K} < \Delta_0 < 10^{-3} \text{ K}$ for the tunneling parameter [53],
- $10^{-5} \text{ K} < \hbar\Omega < 10 \text{ K}$ for the well energy [42, 53]

(it is thought that $\hbar\Omega$ should be the largest energy in the problem, hence of the order of the gap energy's upper cutoff E_{max}). This limits have been verified also in the context of the present ETM theory's various applications and allow us to deduce the range of variation of the barrier height V_0 . Figure 26 shows some iso-lines of Δ_0 as a function of the barrier height V_0 and the well energy $\hbar\Omega$. The range mentioned above for Δ_0 corresponds to the region delimited by the two red bold lines. This plot shows that the typical barrier height range goes up to a maximum of 20 K or so and therefore this value represents a discriminant threshold for the relevant parameters of the TSs (2LSs, specifically). In the past most simulation studies of the properties of the PEL have focused on the so-called "inherent structures" (ISs), i.e. the local minima of the PEL [72, 73, 74, 75]. Following the pioneering work of Goldstein who was the first to point out that the corrugated nature of the PEL is important to understand the slow relaxation dynamics of glass-forming liquids [76], researchers started to study the properties of this landscape for simple glass-forming systems [72, 77, 78, 79]. Weber and Stillinger [77] were the first to analyze the PEL by studying how the system evolves in this complex landscape and explores the various minima. For this they periodically quenched the configurations of molecular dynamics (MD) simulations to zero temperature and identified nearby minima as well as the connecting transition states, i.e. the saddle points (SPs). Subsequently Heuer and coworkers carried out detailed studies in an attempt to determine the properties of the DWPs that are relevant for the low temperature properties of glasses [80, 81]. This was done by searching for the DWPs in the PEL in a wide range of the energy asymmetry Δ , distance between the wells d , and barrier height V_0 .

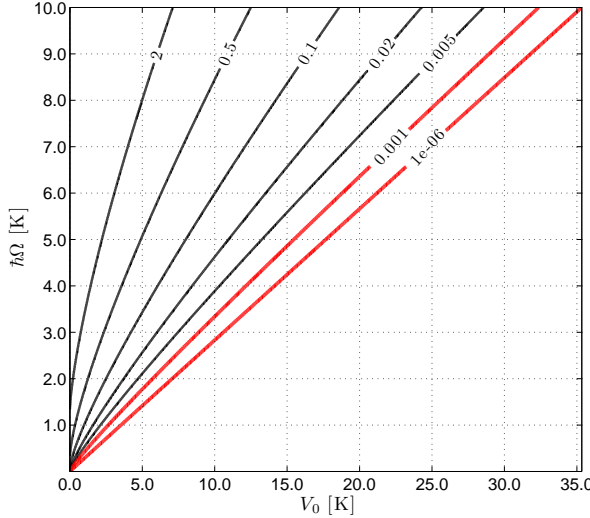


Figure 26: Iso-lines of the tunneling parameter Δ_0 as a function of the barrier height V_0 and the single-well energy $\hbar\Omega$. The physically relevant range for Δ_0 is delimited by the two bold red lines.

After parametrizing these quantities with a polynomial function and subsequently applying an interpolation procedure, they inferred the properties of TSs from the collected sets of DWPs. However, their conclusions regarding the nature of the DWPs in terms of configurations and parameters (asymmetry,...) depend strongly on the manner they have scanned the PEL and as a consequence one does not have, in fact, at present a real good understanding on the nature of the DWPs, or more generally, of the possible atomic configurations that are mutually connected via a tunneling process.

As discussed above, the barrier height of the TSs that are relevant at low T is rather small. However, most previous studies have found that the overwhelming majority of the barriers between two adjacent ISs is not that small, i.e. it is a sizable fraction of the interaction energy between the particles, thus on the order of 100 K [78]. Hence this indicates that in fact the TSs are *not* related to a process in which one particle changes its nearest neighborhood and thus moves a good fraction of the typical nearest neighbor distance, i.e. 0.3-2 Å. So, what other options remain for excitations that give rise to DWPs that have a small barrier height and thus a reasonable tunnelling parameter? One possibility is that these excitation occur in the *interior* of the basin of attraction of an IS. In other words, it could be that the basin of attraction is not just a simple slightly deformed bowl, but is instead corrugated and characterized internally by small channels and valleys. These kind of local deformations in the structure of the PEL can give rise to *effective* DWPs and therefore we believe that both the TSs and the ATSs are associated not with jumps of the system from one IS to a neighboring one, but rather to the motion inside the basin of attraction of a given IS. The TSs could be therefore associated with the motion from one of these valleys to a nearby one and the tunneling can occur among different channels.

To make this idea more specific we show in Fig. 27 what is intended to be an oversimplified representation of the real PEL of a glass, that we computed in order to clarify the concepts; as can be noted, the immediate surrounding of the IS is still harmonic, but as soon as one moves away (always remaining inside the same basin of attraction) different valleys (ending roughly at the N, E, S and W cardinal points in the drawing) develop (as indicated by solid lines), separated by regions in which the potential is higher and where the tunneling processes could occur (a tunneling path is marked by a bold green dashed line). We have two ISs (IS_1 and IS_2) that are connected via a reaction path (thin dashed line) that goes through a SP. Note that this type of transition usually involves only a small number of degrees of freedom, i.e. on the order of 4-10 particles, since the excitation is localized in the three dimensional space. Thus the vast majority of the other particles change their position only marginally in this transition event, since they basically react only in an elastic manner, i.e. without changing their neighborhood. As mentioned above, the typical energy of the SPs is too large to permit a tunneling process with a reasonable probability and thus such processes might be irrelevant for the properties of glasses at low temperatures. We therefore conclude that the TSs should

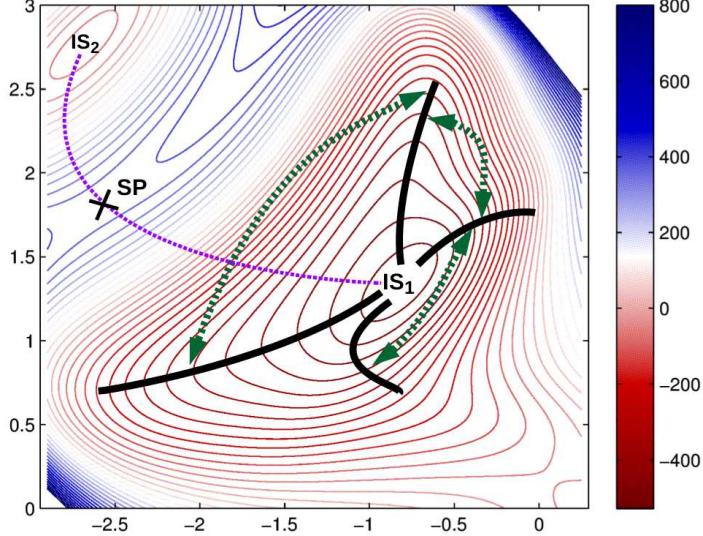


Figure 27: (colour online) Simplified view of the glass potential energy landscape (PEL) of a glass-forming system. We show two local minima, i.e. inherent structures (ISs), that are connected by a first-order saddle point (SP). Also shown are some of the valleys (bold black solid lines) that emanate from the IS and often lead to a SP. The bold green dotted lines represent possible transition pathways from one valley to another. Tunneling takes place across the “reliefs” of the PEL. Note that the paths of these valleys do not necessarily lead to a saddle.

not be thought as a restricted subset of ISs forming DWPs, but rather as small irregular valleys that exist inside a single IS’s basin and characterize the very bottom of the landscape. As is exemplified in Fig. 27, the 2LSSs are tunneling processes of the N-W dashed bold green-path type, whilst the much shallower N-E and S-E tunneling bold green-paths are probably good examples for the more elusive ATSs. We note, however, that to each IS are connected on the order of N_{at} valleys (bold solid lines), many of which lead to one of the $O(N_{at})$ SPs. These valleys are local minima *within* the basin of attraction of a given IS. Since these valleys start all at the IS, their energy difference is small, as long as they are close to the IS. Furthermore one can expect that also the barrier that the system has to cross when moving from one valley to another is not very large. (Such processes are indicated by the bold green dotted lines with arrows.) Thus such an inter-valley transition can approximately be described by a DWP in which the two wells have almost the same energy and the barrier height is not very large, i.e. the DWPs do indeed have the features that we need in order to describe the TSs. Thus at this stage we can speculate that the TSs are related not to the IS-IS transitions, how is usually done, but to valley-valley transitions *inside* the basin of attraction of a single IS. For the moment we can of course only say that the valley-valley transitions will give rise to DWPs that have the right *semi-quantitative* features. It will thus be important to check by means of numerical simulations to what extent these DWPs can indeed be used to describe the low-temperature anomalies of glasses on a *quantitative* basis. In addition it will be important to understand how the specific macroscopic properties of the glass former (composition, local structure etc.) influences the features of the PEL *within* the basin of attraction of an IS, and hence to establish a link between the macroscopic properties of the glass and its behaviour at low temperatures.

From the numerical-analysis point of view, in order to understand the low temperature anomalies found experimentally, there is a need to perform local and systematic analysis of the bottom of the IS basin. Since it has been found [78] that, around the glass transition temperature, the system moves quite close to the IS and the majority of the saddles found is of order 1, the new approach would be the exploration of the IS’s surroundings starting from configurations obtained with standard MD simulations at the lowest temperature that can be equilibrated. The mere location of the SPs is not enough to characterize the PEL, in fact, as we can imagine, a given IS is associated to more than one nearby saddle and furthermore there is no guarantee that following the direction of the softest eigenvalue necessarily leads to the saddle, as depicted in Figure 27: the branches that develop rather tend to vanish in the complexity of the PEL.

We therefore intend to analyze the properties of simple glass-forming systems in order to systematically locate all of the TSs and verify whether they can represent a probe of the very local structure of the PEL and, therefore in this sense, contribute also to the properties of the glass transition. Such numerical simulations should not be too difficult and are currently on the way.

9 Conclusions and Outlook

In conclusion, the ATS tunneling model for the magnetic effects in multi-component glasses (the multi-silicates BAS (or AlBaSiO), Duran and BK7) and contaminated mono-component glass glycerol has been fully justified in terms of a (not entirely) new vision for the intermediate-range structure of real glasses. In this scheme the particles are organized in regions of enhanced regularity (RERs) and more mobile *charged* particles trapped in the interstices between the (on average) close-packed RERs. These are coherent (owing to proximity and strong Coulomb forces) atomic tunnelers that can be modeled in terms of a single quasi-particles with highly renormalized parameters. This model explains a large number of experimental data and facts with remarkable consistency also in terms of cross-checks like the determination of the concentration of trace paramagnetic impurities.

The fact that pure amorphous silica (Spectrosil-I, for example [52]) shows no detectable magnetic effects is a consequence of the extremely small size of the RERs for a-SiO₂, deprived of almost any nucleation centres for both micro-crystal and polycluster (RER) formation. These RERs will therefore trap a very small number N of dangling-bond ionic particles, or none at all given the covalent nature of the Si-O bonds. Hence, no magnetic effects are observable in the purest, single-component glasses.

The present theory shows that the magnetic (and compositional) effects are a mere manifestation of the inhomogeneous, cellular-like intermediate atomic structure of real glasses. A cellular-type structure that has been advocated by scientists, especially (but not only) in the ex-USSR, now for almost a century. It is not impossible that with this vision the TSs could become in the near future the right probes with which to study the structure of glasses in the laboratory.

We have also commented on the possible atomistic computational checks for this theory and it is hoped that in the near future the MD simulations will provide strong evidence for the nature, here proposed, of the tunneling states.

Acknowledgements

One of us (SB) acknowledges support from the Italian Ministry of Education, University and Research (MIUR) through a Ph.D. Grant of the Progetto Giovani (ambito indagine n.7: materiali avanzati (in particolare ceramici) per applicazioni strutturali), as well as from the Bando VINCI-2014 of the Università Italo-Francese. We are very grateful to Maksym Paliienko for his help with data fitting and manuscripts preparation. GJ gratefully acknowledges stimulating discussions with A.S. Bakai.

References

[*] email: giancarlo.jug@uninsubria.it (corresponding author)

- [1] G. Jug: Theory of the Thermal Magnetocapacitance of Multi-component Silicate Glasses at Low Temperature, *Phil. Mag.* **84**(33), 3599–3615 (2004).
- [2] W.A. Phillips (Ed.): *Amorphous Solids: Low Temperature Properties*, (Springer Verlag, Berlin 1981).
- [3] P. Esquinazi (Ed.): *Tunneling Systems in Amorphous and Crystalline Solids* (Springer, Berlin, 1998).
- [4] W.H. Zachariasen: The Atomic Arrangement in Glass, *J. Am. Chem. Soc.* **54**, 3841–3851 (1932); *ibid.*: The Vitreous State, *J. Chem. Phys.* **3**, 162–163 (1935).
- [5] B.E. Warren: The Diffraction of X-Rays in Glass, *Phys. Rev.* **45**, 657–661 (1934).
- [6] P. Strehlow, M. Wohlfahrt, A.G.M. Jansen, R. Haueisen, G. Weiss, C. Enss and S. Hunklinger: Magnetic Field Dependent Tunneling in Glasses, *Phys. Rev. Lett.* **84**, 1938–1941 (2000).
- [7] M. Wohlfahrt, P. Strehlow, C. Enss, and S. Hunklinger: Magnetic-Field Effects in Non-Magnetic Glasses, *Europhys. Lett.* **56**, 690–694 (2001); M. Wohlfahrt: Ph.D. Thesis (Heidelberg 2001, www.ub.uni-heidelberg.de/archiv/1587).
- [8] P. Nagel, A. Fleischmann, S. Hunklinger and C. Enns: Novel Isotope Effects Observed in Polarization Echo Experiments, *Phys. Rev. Lett.* **92**, 245511 (2004).
- [9] M. Brandt, P. Nagel, A. Fleischmann, C. Enss and S. Hunklinger: Evidence for the Crucial Role of Nuclear Spins for the Magnetic Field Effect in Polarization Echoes Experiments, *Phys. Stat. Sol. (Conf. Series)* **1**, 2875–2878 (2004).
- [10] R. W. Simmonds, K. M. Lang, D. A. Hite, S. Nam, D. P. Pappas, and John M. Martinis: Decoherence in Josephson Phase Qubits from Junction Resonators, *Phys. Rev. Lett.* **93**(7), 077003 (2004).
- [11] J.M. Martinis et al.: Decoherence in Josephson Qubits from Dielectric Loss, *Phys. Rev. Lett.* **95**, 210503 (2005).
- [12] A.L. Burin, B.I. Schklovskii, V.I. Kozub, Y.M. Galperin and V. Vinokur: Many electron theory of 1f noise in hopping conductivity, *Phys. Rev. B* **74**, 075205 (2006).
- [13] J. Clarke and F.K. Wilhelm: Superconducting quantum bits, *Nature* **453**, 1031–1042 (2008).
- [14] J.Q. You and F. Nori: Superconducting circuits and quantum information, *Phys. Today* **58**, 42 (2005); *ibid.*: Atomic physics and quantum optics using superconducting circuits, *Nature* **474**, 589–597 (2011).
- [15] A. Amir, Y. Oreg and Y. Imry: On Relaxations and Aging in Various Glasses, *Proc. Nat. Acad. Sci.* **109**(6), 1850–1855 (2012).
- [16] S. Ludwig and D. D. Osheroff: Field-Induced Structural Aging in Glasses at Ultralow Temperatures *Phys. Rev. Lett.* **91**(10), 105501 (2003).
- [17] A.L. Burin et al.: Low-temperature Dipolar Echoes in Amorphous Dielectrics: Significance of Relaxation and Decoherence-free Two-level Systems, *Europhys. Lett.* **104**, 57006–57012 (2013).
- [18] W.M. MacDonald, A.C. Anderson and J. Schröder: Low-temperature Behavior of Potassium and Sodium Silicate Glasses, *Phys. Rev. B* **31**, 1090–1101 (1985).
- [19] G. Jug and M. Palienko: Evidence for a Two-component Tunnelling Mechanism in the Multicomponent Glasses at low Temperatures, *Europhys. Lett.* **90** 36002 (2010).
- [20] C. Enss: Anomalous Behavior of Insulating Glasses at Ultra-Low Temperatures, *Adv. in Solid State Phys.* **42**, 335–346 (2002).
- [21] L. Berthier and G. Biroli: Theoretical perspective on the glass transition and amorphous materials, *Rev. Mod. Phys.* **83**, 587–645 (2011).

[22] J.E. Shelby: *Introduction to Glass Science and Technology*, The Royal Society of Chemistry (Cambridge UK, 2005).

[23] C.A. Angell: Perspective on the Glass Transition, *J. Phys. Chem. Solids* **49**, 863–871 (1988).

[24] V. Lubchenko and P.G. Wolynes: Theory of Structural Glasses and Supercooled Liquids, *Annu. Rev. Phys. Chem.* **58**, 235–266 (2007).

[25] S.L. Simon and G.B. McKenna: Experimental Evidence Against the Existence of an Ideal Glass Transition, *J. Non-Cryst. Solids* **355**, 672–675 (2009).

[26] A.A. Lebedev: O Polimorfizme i Ozhigie Stekla, *Trud'i Gos. Opt. Inst.* **2** 1-20 (1921) (in Russian); *ibid.*, *Izv. Akad. Nauk SSSR, Otd. Mat. Estestv. Nauk, Ser. Fiz.* **3**, 381 (1937).

[27] J.T. Randall, H.P. Rooksby and B.S. Cooper: The Diffraction of X-Rays by Vitreous Solids and its Bearing on their Constitution, *Nature* **125**, 438 (1930); *ibid.*: X-Ray Diffraction and the Structure of Vitreous Solids – I, *Z. Kristallogr.* **75**, 196–214 (1930).

[28] G. Hägg: The Vitreous State, *J. Chem. Phys.* **3**, 42–49 (1935) (Zachariasen's response in Ref. [4]).

[29] A.C. Wright: Crystalline-like Ordering in Melt-quenched Network Glasses? *J. Non-cryst. Solids*, **401** 4–26 (2014); *ibid.*: The Great Crystallite versus Random Network Controversy: A Personal Perspective, *Int. J. Appl. Glass Sci.* **5**, 31–56 (2014).

[30] A.S. Bakai: The Polycluster Concept of Amorphous Solids, Beck/Günterodt (Eds.), *Topics in Applied Physics* **72**, 209–255 (Springer-Verlag, Berlin Heidelberg 1994).

[31] A.S. Bakai: *Poliklastern'ie Amorf'n'ie Tela*, Khar'kov "Synteks" (Khar'kov, Ukraine 2013) (in Russian).

[32] D. Bouttes, E. Gouillart, E. Boller, D. Dalmas and D. Vandembroucq: Fragmentation and Limits to Dynamical Scaling in Viscous Coarsening: An Interrupted *in situ* X-Ray Tomographic Study, *Phys. Rev. Lett.* **112**, 245701 (2014).

[33] J. Hwang, Z.H. Melgarejo, Y.E. Kalay, I. Kalay, M.J. Kramer, D.S. Stone, P.M. Voyles: Nanoscale Structure and Structural Relaxation in $Zr_50Cu_45Al_5$ Bulk Metallic Glass, *Phys. Rev. Lett.* **108**, 195505 (2012).

[34] M.M.J. Treacy and K.B. Borisenko: The Local Structure of Amorphous Silicon, *Science* **335**, 950–953 (2012).

[35] M.M. Hurley and P. Harrowell: Kinetic Structure of a Two-dimensional Liquid, *Phys. Rev. E* **52**, 1694–1698 (1995).

[36] H. Sillescu: Heterogeneity at the Glass Transition: a Review, *J. Non-Cryst. Solids* **243**, 81–108 (1999).

[37] M.D. Ediger: Spatially Heterogeneous Dynamics in Supercooled Liquids, *Annu. Rev. Phys. Chem.* **51**, 99–128 (2000).

[38] K. Vollmayr-Lee and A. Zippelius: Heterogeneities in the Glassy State, *Phys. Rev. B* **72**, 041507 (2005); K. Vollmayr-Lee, W. Kob, K. Binder and A. Zippelius: Dynamical heterogeneities below the glass transition, *J. Chem. Phys.* **116**, 5158–5166 (2002).

[39] C. Donati, S.C. Glotzer, P.H. Poole, W. Kob and S. Plimpton: Spatial Correlations of Mobility and Immobility in a Glass-forming Lennard-Jones Liquid, *Phys. Rev. E* **60**, 3107–3119 (1999).

[40] P.-G. de Gennes: A Simple Picture for Structural Glasses, *Comptes Rendus - Physique* **3**, 1263–1268 (2002).

[41] H.P. Baltes: A Cellular Model for the Specific Heat of Amorphous Solids at Low Temperatures, *Solid State Commun.* **13**, 225–228 (1973).

[42] W.A. Phillips: Two-level States in Glasses, *Rep. Prog. Phys.* **50**, 1657–1708 (1987).

[43] S. Bonfanti and G. Jug: in preparation (2015).

[44] J. A. Sussmann: Electric Dipoles due to Trapped Electrons, *Proc. Phys. Soc. (London)* **79**, 758–774 (1962).

[45] G. Jug: Multiple-well Tunneling Model for the Magnetic-field Effect in Ultracold Glasses *Phys. Rev. B* **79**, 180201 (2009).

[46] G. Jug and M. Paliienko: Multilevel Tunneling Systems and Fractal Clusters in the Low-Temperature Mixed Alkali-Silicate Glasses, *Sci. World J.* **2013**, 1–20 (2013).

[47] G. Jug, M. Paliienko and S. Bonfanti: The Glassy State Magnetically Viewed from the Frozen End, *J. Non-Crys. Solids* **401**, 66–72 (2014).

[48] L. Siebert: Ph.D. Thesis Heidelberg University (2001), www.ub.uni-heidelberg.de/archiv/1601

[49] T. Herrmannsdörfer and R. König: Magnetic Impurities in Glass and Silver Powder at Milli- and Microkelvin Temperatures, *J. Low Temp. Phys.* **118**, 45–57 (2000).

[50] S. Bonfanti and G. Jug: On the Paramagnetic Impurity Concentration of Silicate Glasses from Low-Temperature Physics *J. Low Temp. Phys.* **180**, 214–237 (2015).

[51] A. Abragam and B. Bleaney: *The Physical Principles of Electron Paramagnetic Resonance* (Clarendon, Oxford 1970).

[52] S. Ludwig, P. Nagel, S. Hunklinger and C. Enss: Magnetic Field Dependent Coherent Polarization Echoes in Glasses, *J. Low Temp. Phys.* **131**, 89–111 (2003).

[53] M. Paliienko: Multiple-welled Tunnelling Systems in Glasses at low Temperatures (Ph.D. Thesis, Università degli Studi dell’Insubria, 2011) <http://insubriaspace.cineca.it/handle/10277/420>

[54] J. Jackle: On the Ultrasonic Attenuation in Glasses at Low Temperatures, *Z. Physik* **257**, 212–223 (1972).

[55] F. Bloch: Nuclear Induction, *Phys. Rev.* **70**, 460–474 (1946).

[56] H.M. Carruzzo, E.R. Grannan and C.C. Yu: Non-Equilibrium Dielectric Behavior in Glasses at Low Temperatures: Evidence for Interacting Defects, *Phys. Rev. B* **50**, 6685–6695 (1994).

[57] S. Hunklinger and W. Arnold, in: *Physical Acoustics*, R.N. Thurston and W.P. Mason (Eds.), Vol. **12**, p. 155– (1976).

[58] S.A.J. Wiegers, R. Jochemsen, C.C. Kranenburg and G. Frossati: Comparison of some Glass Thermometers at Low Temperatures in a High Magnetic Field, *Rev. Sci. Instrum.* **58**, 2274–2278 (1987).

[59] G. Jug (unpublished).

[60] F. LeCochec, F. Ladieu and P. Pari: Magnetic field effect on the dielectric constant of glasses: Evidence of disorder within tunneling barriers, *Phys. Rev. B* **66**, 064203 (2002).

[61] B.P. Smolyakov and E.P. Khaimovich, (courtesy A. Borisenko) *Pis’ma Zh. Eksp. Teor. Fiz.* **29**, 464 (1979) (in Russian); *ibid.*: Dynamic processes in dielectric glasses at low temperatures, *Sov. Phys. Uspekhi*, **25**, 102115 (1982).

[62] S. Ludwig, P. Nagel, S. Hunklinger and C. Enss: Direct Coupling of Magnetic Fields to Tunneling Systems in Glasses, *Phys. Rev. Lett.* **88**, 075501 (2002).

[63] A. Würger, A. Fleischmann and C. Enss: Dephasing of Atomic Tunneling by Nuclear Quadrupoles, *Phys. Rev. Lett.* **89**, 237601 (2002).

[64] A. Fleischmann and C. Enns: Geheimniss der Tunnelssysteme im Glas gelüftet, *Physik Journal* **6** (Nr. 10), 41–46 (2007) (in German).

[65] M. Bartkowiak, M. Bazrafshan, C. Fischer, A. Fleischmann and C. Enss, Nuclear Quadrupole Moments as a Microscopic Probe to Study the Motion of Atomic Tunneling Systems in Amorphous Solids, *Phys. Rev. Lett.* **110**, 205502 (2013).

- [66] V.L. Gurevich, M.I. Muradov and D.A. Parshin: Electric Dipole Echo in Glasses, *Sov. Phys. JETP* **70**, 928 (1990).
- [67] Yu.M. Galperin, V.L. Gurevich and D.A. Parshin: Nonlinear Resonant Attenuation in Glasses and Spectral Diffusion, *Phys. Rev. B* **37**, 10339–10349 (1988).
- [68] J.L. Black and B.I. Halperin: Spectral Diffusion, Phonon Echoes and Saturation Recovery in Glasses at Low Temperatures, *Phys. Rev. B* **16**, 2879–2895 (1977).
- [69] M. Brandt: Ph.D. Thesis Heidelberg University (2004), www.ub.uni-heidelberg.de/archiv/4822
- [70] C. Enss, S. Ludwig, R. Weis and S. Hunklinger: Decay of Spontaneous Echoes in Glasses, *Czechoslovak J. Phys.* **46**, 2247–2248 (1996).
- [71] N.W. Ashcroft and N.D. Mermin, *Solid State Physics* (Saunders College, Philadelphia 1976)
- [72] S. Sastry, P.G. Debenedetti and F.H. Stillinger. Signatures of Distinct Dynamical Regimes in the Energy Landscape of a Glass-forming Liquid, *Nature* **393**(6685): 554–557 (1998).
- [73] P.G. Debenedetti and F.H. Stillinger: Supercooled Liquids and the Glass Transition, *Nature* **410**(6825): 259–267 (2001).
- [74] F. Sciortino: Potential Energy Landscape Description of Supercooled Liquids and Glasses, *J. Stat. Mech.* 050515, (2005).
- [75] A. Heuer: Exploring the Potential Energy Landscape of Glass-forming Systems: from Inherent Structures via Metabasins to Macroscopic Transport, : *J. Phys.: Condens. Mat.* **20**, 373101 (2008).
- [76] M. Goldstein: Viscous Liquids and the Glass Transition: a Potential Energy Barrier picture, *J. Chem. Phys.* **51**, 37283739 (1969).
- [77] T.A. Weber and F. Stillinger: Interactions, Local Order, and Atomic-rearrangement Kinetics in Amorphous Nickel-phosphorous Alloys, *Phys. Rev. B* **32**, 5402– (1985).
- [78] L. Angelani, G. Ruocco, M. Sampoli, and F. Sciortino: General Features of the Energy Landscape in Lennard-Jones-like Model Liquids, *J. Chem. Phys.* **119**, 2120–2126 (2003).
- [79] K. Broderix, K. K. Bhattacharya, A. Cavagna, A. Zippelius, and I. Giardina: Energy Landscape of a Lennard-Jones Liquid: Statistics of Stationary Points, *Phys. Rev. Lett.* **85**, 5360–5363 (2000).
- [80] A. Heuer and R.J. Silbey: Microscopic description of tunneling systems in a structural model glass, *Phys. Rev. Lett.* **70**, 3911–3914 (1993).
- [81] J. Reinisch and A. Heuer: Microscopic Description of the Low-temperature Anomalies in Silica and Lithium Silicate via Computer Simulations, *J. Chem. Phys. B* **110**, 19044–19052 (2006).